Universitat
de les Illes Balears

DOCTORAL THESIS
2023

COMPLEX OPTICAL NETWORKS BASED ON VERTICAL-CAVITY SURFACE-EMITTING LASERS (VCSELS)

Moritz Pascal Dominik Pflueger

Universitat
de les Illes Balears

DOCTORAL THESIS
2023

DOCTORAL PROGRAMME IN PHYSICS

COMPLEX OPTICAL NETWORKS BASED ON VERTICAL-CAVITY SURFACE-EMITTING LASERS (VCSELS)

Moritz Pascal Dominik Pflueger

THESIS SUPERVISOR: *Prof. Dr. Ingo Fischer*
THESIS SUPERVISOR: *Dr. Daniel Brunner*
THESIS TUTOR: *Prof. Dr. Pere Colet Rafecas*

DOCTOR BY THE UNIVERSITAT DE LES ILLES BALEARS

Prof. Dr. Ingo Fischer from IFISC and Dr. Daniel Brunner from Femto-ST, declare that this thesis titled "Complex Optical Networks based on Vertical-Cavity Surface-Emitting Lasers (VCSELs)", presented by Moritz Pflüger to obtain the doctoral degree, has been completed under their supervision.

For all intents and purposes, they hereby sign this document.

Prof. Dr. Ingo Fischer Thesis Supervisor	Dr. Daniel Brunner Thesis Supervisor
Prof. Dr. Pere Colet Thesis Tutor	Moritz Pascal Dominik Pflueger PhD Student

Abstract

This thesis is centered around the experimental realization of networks of optically coupled vertical-cavity surface-emitting lasers (VCSELs) that are arranged in square-lattice arrays, using diffraction in an external cavity. After successfully implementing the diffractive coupling scheme, we experimentally study qualitatively and quantitatively the coupling of VCSEL pairs and of an entire VCSEL array, as well as simultaneous optical injection into all the VCSELs. Finally, we evaluate the established network's potential for brain-inspired information processing.

Very few networks containing more than twenty optically coupled semiconductor lasers (SLs) have so far been implemented, although they are interesting for various reasons. From a fundamental research point of view, they allow studying the dynamics of real-world complex networks at high speed. From an application-oriented perspective, they are promising hardware substrates for neuro-inspired computing.

We first characterize the individual VCSELs. After that, we study the behaviour of coupled VCSEL pairs, mainly by analyzing their optical and radio-frequency (RF) spectra. In the RF spectra of the central VCSEL of the array, we find signatures for coupling with every individual non-central VCSEL. Analyzing the optical spectra, we find optical locking of the central VCSEL with two thirds of the individual non-central VCSELs. For entire-array coupling, we also find a clear transition in both optical and RF spectra of the central VCSEL upon incrementing the common wavelength of the ensemble of the non-central VCSELs. We interpret this as a transition from entire-array locking to unlocking. Furthermore, we achieve simultaneous optical injection locking of 22 out of 25 VCSELs to an external drive laser, and analyze the dynamic response of the VCSELs to intensity-modulated injection.

Having characterized coupling and injection, we evaluate the experimental setup's capacity to be utilized as a reservoir computer. We test our experimental system's computing capability on the four basic benchmark tasks memory capacity, exclusive or, header recognition, and digital-to-analog conversion. We observe that the system has good one-step-memory, which then decays rapidly to close to zero for five steps. For the other tasks, we observe that the performance depends crucially on the complexity of the task, with low errors for the 2-bit versions of the tasks, but with substantial decreases in precision for every additional bit. Investigating the output configuration, we find that the change in computing performance upon connecting a reservoir node to the output layer varies greatly from node to node, which means that not all nodes in the output layer are equally important. However, we could not identify reliable indicators of a node's contribution to the computing performance.

In summary, we have experimentally established a diffractively coupled VCSEL network, characterized the coupling and injection, and evaluated the information-processing properties of the network. We have therefore demonstrated one of the first experimental realizations in which tens of SLs are optically coupled within a scalable approach. These results are of interest for the study of complex systems and for photonic reservoir computing.

Resumen de la tesis

Esta tesis se centra en la realización experimental de redes de láseres de cavidad vertical con emisión de superficie (en inglés VCSELs, acrónimo de *vertical-cavity surface-emitting laser*) dispuestos en una retícula cuadrada y acoplados ópticamente utilizando difracción en una cavidad externa. Tras implementar con éxito el esquema de acoplamiento difractivo, estudiamos experimentalmente de forma cualitativa y cuantitativa el acoplamiento entre parejas de VCSELs y de todo un conjunto de VCSELs, así como la inyección óptica simultánea en todos los VCSELs. Por último, evaluamos el potencial de la red que hemos desarrollado como procesador de información inspirado en el cerebro.

Hasta la fecha se habían implementado muy pocas redes en las que se pudieran acoplar ópticamente más de diez láseres semiconductores (SL por su acrónimo en inglés), las cuales son interesantes por diversas razones, como se detalla a continuación. Desde el punto de vista de la investigación fundamental, permiten estudiar las dinámicas de redes complejas físicas a altas velocidades. Desde el punto de vista de las aplicaciones, son una base prometedora para la computación neuroinspirada.

En primer lugar, caracterizamos los VCSELs individuales. Después, estudiamos el comportamiento de VCSELs acoplados a pares, principalmente analizando sus espectros ópticos y de radiofrecuencia (RF). En los espectros de RF del VCSEL central del conjunto, encontramos evidencia de acoplamiento con cada uno de los otros VCSELs. Analizando los espectros ópticos, encontramos acoplamiento óptico entre el VCSEL central y dos tercios de los VCSELs no centrales. Al acoplar todo el conjunto, también observamos una clara transición en los espectros ópticos y de RF del VCSEL central al aumentar la longitud de onda común del conjunto de VCSELs no centrales. Interpretamos este fenómeno como una transición del encadenamiento óptico del conjunto completo a su desencadenamiento. Además, logramos simultáneamente encadenar por inyección óptica 22 de los 25 VCSELs a un láser externo y analizamos la respuesta dinámica de los VCSELs a una modulación en la intensidad de la señal de inyección.

Una vez caracterizados el acoplamiento y la inyección óptica, evaluamos la capacidad del montaje experimental para ser utilizado como reservorio computacional. En este contexto, comprobamos la capacidad de cálculo de nuestro sistema experimental en cuatro tareas básicas de referencia: capacidad de memoria, disyunción exclusiva, reconocimiento de cabeceras y conversión de digital a analógico. Observamos que el sistema tiene una buena memoria a un paso atrás, que luego decae rápidamente hasta acercarse a cero en el quinto paso. Para las demás tareas, observamos que el rendimiento depende sustancialmente de la complejidad de la tarea, con errores bajos para las versiones de 2 bits, pero con descensos importantes de precisión por cada bit adicional. Al investigar la configuración de salida, observamos que el cambio en el rendimiento computacional, al conectar un nodo del reservorio a la capa de salida, varía mucho de un nodo a otro, lo que significa que no todos los nodos de la capa de salida tienen la misma importancia. Sin embargo, no hemos podido identificar indicadores fiables de la contribución de un nodo al rendimiento computacional global.

En resumen, en esta tesis hemos demostrado experimentalmente una red de VCSELs acoplada por difracción, hemos caracterizado el efecto del acoplamiento y de la inyección óptica, y hemos evaluado las propiedades de la red para el procesamiento de información. De esta manera, hemos generado uno de los primeros sistemas experimentales en el que decenas de SLs se acoplan ópticamente con un esquema escalable. Estos resultados son de interés para el estudio de sistemas complejos y para la computación usando reservorios fotónicos.

Resum de la tesi

Aquesta tesi se centra en la realització experimental de xarxes de làsers de cavitat vertical amb emissió de superfície (en anglès VCSELs, acrònim de *vertical-cavity surface-emitting laser*), disposats en una retícula quadrada i acoblats òpticament utilitzant difracció en una cavitat externa. Després d'implementar amb èxit l'esquema d'acoblament difractiu, estudiem experimentalment de manera qualitativa i quantitativa l'acoblament tant entre parelles de VCSELs com de tot un conjunt, així com la injecció òptica simultània a tots els VCSELs. Per acabar, avaluem el potencial de la xarxa que hem desenvolupat com a processador d'informació inspirat en el cervell.

Fins ara s'havien implementat molt poques xarxes on es poguessin acoblar òpticament més de deu làsers semiconductors (SL pel seu acrònim en anglès), les quals són interessants per diverses raons com es detalla a continuació. Des del punt de vista de la investigació fonamental, permeten estudiar les dinàmiques de xarxes complexes físiques a altes velocitats. Des del punt de vista de les aplicacions, són una base prometedora per a la computació inspirada en el cervell.

En primer lloc, caracteritzem els VCSELs individuals. Després, estudiem el comportament de VCSELs acoblats a parells, principalment analitzant els seus espectres òptics i de radiofreqüència (RF). En els espectres de RF del VCSEL central del conjunt, trobem evidència d'acoblament amb cadascun dels altres VCSELs. Analitzant els espectres òptics, trobem acoblament òptic entre el VCSEL central i dos terços dels VCSELs no centrals. En acoblar tot el conjunt, també observem una transició clara en els espectres òptics i de RF del VCSEL central en augmentar la longitud d'ona comuna del conjunt de VCSELs no centrals. Interpretem aquest fenomen com una transició d'encadenament òptic del conjunt complet al seu desencadenament. A més, aconseguim simultàniament encadenar per injecció òptica 22 dels 25 VCSELs a un làser extern i analitzem la resposta dinàmica dels VCSELs a una modulació de la intensitat del senyal d'injecció.

Un cop caracteritzats l'acoblament i la injecció òptica, avaluem la capacitat del muntatge experimental per ser utilitzat com a reservori computacional. En aquest context, comprovem la capacitat de càlcul del nostre sistema experimental en quatre tasques bàsiques de referència: capacitat de memòria, disjunció exclusiva, reconeixement de capçaleres i conversió de digital a analògic. Observem que el sistema té una bona memòria a un pas enrere, que després decau ràpidament fins a acostar-se a zero al cinquè pas. Per a la resta de tasques, observem que el rendiment depèn substancialment de la complexitat de la tasca, amb errors baixos per a les versions de 2 bits, però amb descensos importants de precisió per cada bit addicional. En investigar la configuració de sortida, observem que el canvi en el rendiment computacional en connectar un node del reservori a la capa de sortida, varia molt d'un node a un altre, cosa que significa que no tots els nodes de la capa de sortida tenen la mateixa importància. Tot i això, no hem pogut identificar indicadors fiables de la contribució d'un node al rendiment computacional global.

En resum, en aquesta tesi hem establert experimentalment una xarxa de VCSELs acoblada per difracció, hem caracteritzat l'efecte de l'acoblament i de la injecció òptica, i hem avaluat les propietats de la xarxa per al processament d'informació. D'aquesta manera, hem generat un dels primers sistemes experimentals en què desenes de SL s'acoblen òpticament amb un esquema escalable. Aquests resultats són interessants per a l'estudi de sistemes complexos i per a la computació usant reservoris fotònics.

Acknowledgements

First, I'd like to thank my supervisors Ingo Fischer and Daniel Brunner. Especially at the beginning of my PhD, Ingo took a lot of time for patiently answering all my questions and listening to way too detailed reports about my progress in the lab. Towards the end of my PhD, Daniel gave me the straightforward and results-oriented guidance that I needed. Thanks to both of you for teaching me valuable lessons that have not only made me a better scientist, but have also improved my structured and strategic thinking in general.

Many thanks also to Stephan Reitzenstein's group at TU Berlin for providing the VCSEL arrays for this work and for welcoming me for a one-week stay during which we tested and selected the best devices for our experiments, and to James Lott's group for providing the raw material for said devices. In particular, I'd like to thank Tobias Heuser, who never gave up during the manufacturing, despite all the setbacks that occurred, and that hit him at least as hard as they hit me.

Another special thanks goes out to Daniel Palou and Pep Canyelles, even though I've never met the former in person. The two of them, together with Daniel Brunner, constructed an experimental control system without which the experiments for this thesis would not have been possible.

I'm grateful, as well, to many former and current members of the FESC group, of which I'd like to mention the following ones explicitly: Thanks to Julián Bueno Moragues for introducing me into many aspects of experimental research work in the nonlinear photonics lab; to Apostolos Argyris for always leaving his office door open for people like me asking for help in the lab or having basic questions and for wanting to work with me on the ADOPD project; to Irene Estébanez Santos for many discussions that have improved my understanding of our research topics; and to Pau Massutti Ballester for helping me with several technical problems.

Many thanks also to the optics department at Femto-ST Besançon for welcoming me for a three-week stay. Here, I especially want to mention Louis Andréoli, with whom I worked in the lab during that time and from whom I learned a thing or two about optical free-space setups.

I'm grateful for all the administrative help at IFISC and UIB, too. Here, I'd like to highlight how Marta Ozonas Hernández helped me with all the bureaucracy that I faced when starting to work at IFISC, and how Inma Carbonell Bosca was always there to help and how she made all the bureaucratic procedures as uncomplicated as possible. Furthermore, I acknowledge the economic support by the Volkswagen Foundation and the CSIC during my PhD.

Another group that I don't want to forget are the current and former PhD students and postdocs at IFISC. Thank you for making the 'IFISC underground' a nice place to work at, for funny conversations and interesting discussions during lunch, and for your help with academic and bureaucratic questions.

Of course, I'd also like to thank my mother and my father for all their support, especially during my Bachelor and Master studies. Without this foundation I could not have ended up pursuing a PhD.

Finally, a special thanks goes out to my brother, my flatmates, my climbing buddies, to all my friends here and elsewhere, and in general to all the people who have helped me with anything related to this thesis, or who have made my life more enjoyable during this whole time, but have not been mentioned yet.

¡THANK YOU ALL!

Publications and communications

Publications

- Moritz Pflüger, Daniel Brunner, Tobias Heuser, James Lott, Stephan Reitzenstein, and Ingo Fischer, *Injection locking and coupling the emitters of large VCSEL arrays via diffraction in an external cavity*, Optics Express **31**(5), 8704-8713 (2023).
- Moritz Pflüger, Daniel Brunner, Tobias Heuser, James Lott, Stephan Reitzenstein, and Ingo Fischer, *Experimental reservoir computing implementation with optically coupled VCSELs*, in preparation.
- Tobias Heuser, Moritz Pflüger, Ingo Fischer, James Lott, Daniel Brunner, and Stephan Reitzenstein, *Developing a photonic hardware platform for brain-inspired computing based on* 5×5 *VCSEL arrays*, Journal of Physics: Photonics **2**, 044002 (2020).

Other relevant contributions

- Moritz Pflüger, Daniel Brunner, Tobias Heuser, James Lott, Stephan Reitzenstein, and Ingo Fischer, *Injection locking and coupling large VCSEL arrays via diffraction in an external cavity*, Talk at the Online Workshop "Nonlinear Dynamics in Semiconductor Lasers 2021" (WIAS Berlin, June 2021).

Contents

List of Figures

List of Tables

Chapter 1

Introduction

There are inventions that are designed for a very specific purpose, e.g. a lunchbox in the shape of a banana. The laser is not one of these inventions. Shortly after the first experimental demonstration of a laser, it was described as a "solution looking for a problem", because, despite not being developed for a single specific use, researchers expected it to find applications in broad areas [1]. And they have been proven right since. Lasers have penetrated virtually all fields of science and medicine, and most of our communication today is based on the use of lasers and optical fibers [2]. For most well-known laser applications, like reading optical disks (such as CD, DVD, and Blu-Ray) or refractive eye surgery, the decisive characteristics of the laser light are its high coherence, beam directionality and intensity [3, p. 642]. But especially for semiconductor lasers (SLs), there are additional properties to investigate, like their extreme sensitivity to optical feedback (FB) and optical coupling, which can give rise to interesting phenomena or can be exploited for applications in many creative ways. With this thesis, our aim is to make a little contribution to this rich field of research that has been referred to as complex photonics [4].

1.1 Vertical-Cavity Surface-Emitting Lasers (VCSELs)

The experiments in this thesis were carried out with arrays of vertical-cavity surface-emitting lasers (VCSELs). VCSELs usually are a type of quantum-well SLs, whose cavities are formed by the surfaces of epitaxial layers [5] that create distributed Bragg reflector (DBR) mirrors with high reflectivities of typically $> 99\%$. This is achieved by periodically alternating layers with high refractive index contrast along the light's propagation direction. VCSELs emit light orthogonally to the layers of wafer growth and thus orthogonally to the p-n-junction. Surface-emitting lasers were first implemented by Soda et al. in 1979 [6]. A major advantage of VCSELs that we exploit for this thesis is the possibility of arranging them in two-dimensional arrays, which has already been suggested in early publications [7]. Other potential advantages of VCSELs over other SLs include efficient coupling to optical fibers due to a circular symmetric optical beam profile and low beam divergence, high modulation bandwidths due to their short photon lifetimes, and the possibility of on-wafer testing [8]. In this thesis, we use VCSEL arrays that were custom-manufactured at Technische Universität (TU) Berlin. A scheme of such a VCSEL is shown in Fig. 1.1a, and a more detailed description of the used devices can be found in Sec. 2.1 and Ref. [9].

SL dynamics can be modeled using rate equations. For VCSELs, the spin-flip model (SFM) by San Miguel et al. [10] is well-established and has been extended, e.g. to describe the spatio-temporal dynamics [11]. The SFM takes into account that the polarization stability of the emitted light is typically much lower for VCSELs than for edge-emitting lasers. It considers the transitions between different spin sublevels of the valence and the conduction band, which are associated with different polarizations of the light, as sketched in Fig. 1.1b. The mathematical description consists of differential equations for the left and right circularly polarized components $E_{\pm}$ of the electric field, the difference between the actual carrier number and the carrier number at transparency N (also called

the population inversion), and the difference in the carrier numbers of the two magnetic sublevels m [8]. The most important parameters are the different rates of decays and transitions, like the spin relaxation rate γ_s, the cavity photon lifetime γ_p, the decay rate of the population difference γ_c, and the decay rate of the dipole polarization γ_d, as well as the linewidth enhancement factor α, which is treated in more detail in the next paragraph. For $E_+ = E_-$ and $m = 0$, the SFM rate equations reduce to a widely used rate equation model for the population inversion N and the total electric field E. These reduced equations are sufficient to explain a phenomenon called relaxation oscillations (ROs). The ROs are a relaxation to the steady state that occurs through damped oscillations of the coupled quantities N and E after a perturbation, e.g. when the laser is switched on [3, p. 662]. The ROs can also be undamped by delayed FB.

The linewidth enhancement factor α [12] plays an important role for VCSELs and SLs in general. For SLs, it can be defined as [13]

$$\alpha = -\frac{d\chi_r(n)/dn}{d\chi_i(n)/dn} = 2\frac{\omega}{c}\frac{d\eta_r/dn}{dg/dn}, \tag{1.1}$$

where χ_r is the real part and χ_i is the imaginary part of the susceptibility, n is the carrier density inside the active region, ω is the angular frequency of the light, η_r is the real part of the refractive index, and g is the gain per unit length. Note that the signs one finds in literature might vary depending on conventions used in the derivation of the equation [14] and that α is not constant for a given laser, but depends e.g. on the pump current and the detuning of gain spectrum and cavity resonance. While for most non-SL lasers $\alpha \ll 1$, for VCSELs typical values are $1 < \alpha < 10$. The α-factor describes a nonlinearity that is particular to SLs, the amplitude-phase coupling [12]

$$\frac{d\phi}{dt} = \frac{\alpha}{2I}\frac{dI}{dt}, \tag{1.2}$$

where ϕ is the phase and I is the intensity. This coupling arises from the fact that in SLs photons are generated by interband transitions, and not by transitions between two discrete levels. Thus, the gain spectrum is asymmetric. Since gain and refractive index can be expressed as the real and imaginary part of the same analytic function of the frequency, they are connected via the Kramers-Kronig relationship. This connection of gain and refractive index leads to the above-described amplitude-phase coupling.

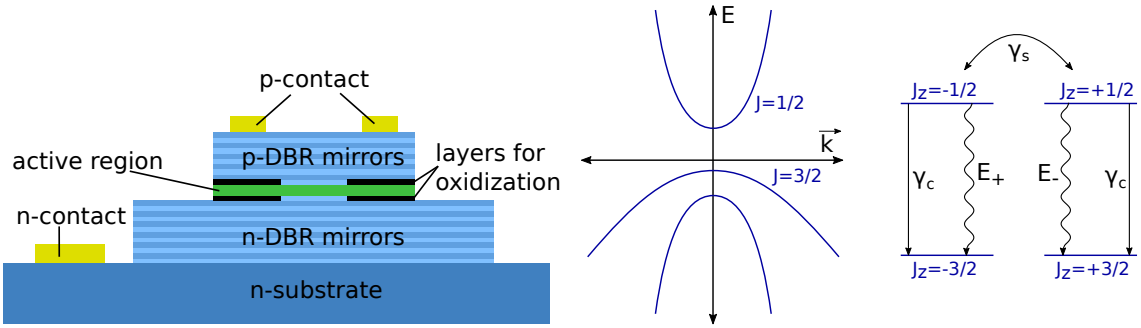

(a) Scheme of a VCSEL with double-mesa structure, similar to the ones used in this thesis. The light is emitted in upwards direction. The substrate and the bottom DBR mirrors are n-doped, while the top DBR mirrors are p-doped. The aperture is defined by oxidization into predefined layers next to the active region.

(b) The spin-flip model (SFM) considers allowed transitions between the conduction band and the heavy holes of the valence band with rate γ_c and spin-flips with rate γ_s. Allowed transitions must fulfil $\Delta J_z = \pm 1$, where J is the spin, and correspond to left and right circularly polarized field components E_- and E_+.

FIGURE 1.1: VCSEL scheme and SFM levels.

1.2 Coupled lasers

Many experiments have been carried out with coupled lasers, and these investigations can be classified by different criteria, of which three are presented in the following subsections.

1.2.1 Principle coupling configurations

Networks are made up of nodes and connections between these nodes. In networks of coupled lasers, the most basic types of optical connections are unidirectional coupling, bidirectional coupling, and self-coupling, i.e. feedback (FB). In Fig. 1.2, an example network and examples for these three principle coupling configurations are shown. In the next paragraphs, these types of coupling are briefly introduced. For a more comprehensive summary of the observed phenomena, see the review by Soriano and coworkers [4]. Note that coupling between lasers is not always optical coupling, as specified in more detail in the next subsection.

For bidirectional optical coupling, the light emitted by one laser is received by another one. Due to symmetry principles in optical propagation, this leads to the light of the second laser also being injected into the first one, unless one introduces optical elements that break this symmetry, such as optical isolators. The particularities of the resulting laser network dynamics depend on different criteria, like if the lasers are identical or different, the frequency detuning between the lasers, the coupling strengths in both directions, and the coupling delay. Different synchronization phenomena can be observed for two bidirectionally coupled SLs [15–18] in general and for VCSELs [19] in particular.

In a typical unidirectional optical coupling configuration, an optical isolator is used. Thus, only the so-called drive laser or injection laser injects light into the response laser, and not the other way around. Wieczorek et al. compare a wide range of theoretically predicted and experimentally observed phenomena for optical injection in SLs in their review article [20]. An important effect in unidirectionally coupled lasers is optical injection locking, i.e. emission of the response laser at the drive laser's frequency. For optical injection locking, the difference between the frequencies of both lasers is limited [21–23,

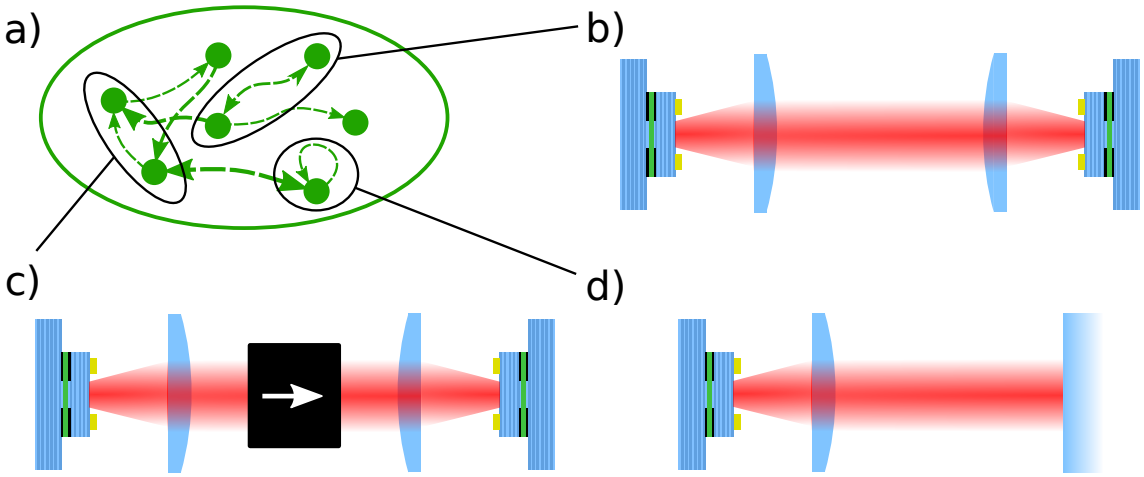

FIGURE 1.2: a) Network of connected nodes with different coupling configurations. b) - d) Principle coupling configurations with example schemes. b) Bidirectional optical coupling of two VCSELs. Two lenses collimate the light emitted by one VCSEL and focus it into the other VCSEL. c) Unidirectional optical coupling of two VCSELs. The optical isolator (marked by the arrow) inhibits the propagation of light from the right to the left. d) VCSEL with optical feedback (FB). The emitted light is reflected at a mirror and coupled back into the VCSEL.

p. 173] and given by

$$-k_c\sqrt{1+\alpha^2}\sqrt{\frac{P_{inj}}{P_r}}\Bigg|_{tf(c,r)} \leq \Delta\omega \leq k_c\sqrt{\frac{P_{inj}}{P_r}}\Bigg|_{tf(c,r)}, \tag{1.3}$$

where $\Delta\omega = 2\pi(f_{inj} - f_r)$ is the difference between the angular frequencies of both lasers, α and P_r are the response laser's linewidth enhancement factor and output power, respectively, $P_{inj}|_r$ is the power of the injection laser's emission at the entry facet of the response laser and k_c is the coupling coefficient of the injection laser into the response laser. Note that $k_c \propto \tau_c^{-1}$ [23], with τ_c being the cavity photon lifetime. Importantly, for VCSELs – other than for edge emitters – the cavity round-trip time cannot be inserted for τ_c due to the high reflectivity of the DBR mirrors.

By reintroducing the emitted light into a laser, the laser is subjected to optical FB. The most employed mathematical model to describe SLs with FB is the rate equation model by Lang and Kobayashi [24]. For VCSELs, this model has been found to be in good agreement with experimental results [25]. One usually defines a long-delay and a short-delay regime, depending on whether the ratio between the round-trip time in the external cavity is larger than the RO frequency (f_{RO}) of the lasers or not. Another crucial FB parameter is the FB power ratio, i.e. the ratio of the fed-back light and the laser emission. Tkach and Chraplyvy defined different regimes of FB, mainly depending on the FB power ratio but also on the cavity length, according to their results with DFB lasers [26]. One important effect observed with FB is the reduction of an SL's lasing threshold [27], which depends on the FB power ratio. The theoretically derived relation has been experimentally confirmed for VCSELs [28]. Additionally, FB gives rise to external cavity modes, as already predicted and found by Lang and Kobayashi [24]. For VCSELs, these were experimentally confirmed to be spaced by the external cavity frequency [29].

In the experimental setup used for this thesis, all three introduced types of optical coupling between lasers are created. The input signal from an injection laser passes through an optical isolator and is thus unidirectionally coupled into the VCSELs, the VCSELs

are bidirectionally coupled to their nearest and second-nearest neighbours, and also to themselves via the external cavity. Thus, we observe an interplay of optical FB and unidirectional and bidirectional coupling in our experiments.

1.2.2 Ways to establish coupling

There are different ways to make lasers interact with each other. In optical fiber networks [19, 30–32], lasers can be readily connected using optical couplers and other fiber-optical components. However, one potentially has to deal with the nonlinearities of the optical fiber. Furthermore, every connection has to be established separately, which complicates scaling this concept to large numbers of lasers.

In photonic integration approaches, SLs do not necessarily have to be optically coupled. Evanescent coupling of implant-defined VCSELs [33, 34] is a possibility, as well as leaky-wave coupling [35, 36], or novel approaches like far-field radiations with definite phase relations [37]. Optical coupling can be implemented monolithically, too, e.g. via direct connections of waveguides [38] or by defining cavities with Talbot geometries [39–41].

Lasers can also be coupled via dedicated mirrors in free-space optical setups [17, 42, 43], however, the complexity of the setup increases rapidly with the size of the laser network. As mentioned for integrated approaches, in free-space configurations the Talbot effect has also been exploited [44, 45]. However, this results in a limitation of the dynamical regimes, since it requires in-phase emission [46].

In this thesis, we utilize diffractive coupling of VCSELs. In our approach, which is described in detail in Sec. 2.2, we use a special element that acts similar to a diffraction grating, and to which we refer as the diffractive optical element (DOE). One challenge that one faces with this approach is that a constant of this DOE, the pitch of the VCSELs, and the VCSELs' emission wavelengths have to fulfil a given relation (Eq. 2.1). As a consequence, either DOE or VCSEL arrays have to be custom-manufactured. Another challenge is that – similar to configurations with dedicated mirrors or free-space Talbot approaches – precise alignment of the optical free-space components is required. The advantages of the used approach are that it is scalable [47, 48], and partially reconfigurable [46].

1.2.3 Phenomena and applications

Coupled lasers and lasers with FB can be investigated for different reasons and with different motivations, and one can observe a broad variety of phenomena and find various creative applications. One frequent research goal is in-phase emission of laser arrays to decrease beam divergence and increase output powers. Successful implementations of this exist with CO_2 lasers [44], with VCSELs [34, 36], and with short-cavity surface-emitting THz quantum-cascade lasers [37]. Optical FB can broaden or reduce SL linewidths [49], and both linewidth reduction by six orders of magnitude [50] and linewidth increase by four orders of magnitude [51] have been observed experimentally. Note that the latter has applications in optical metrology, since for some measurements bright well-directed low-coherence light sources are the best choice [51]. Besides, polarization-rotated optical FB can give rise to chaotic instabilities in SLs. This behaviour has been used for experimental random number generation [52–55].

As hinted in Subsec. 1.2.1, with coupled SLs, different interesting synchronization phenomena can be observed [17, 30, 42] and exploited for applications, like e.g. identical chaos synchronization, which has been used in experiments for a secure key exchange

protocol [56]. Since similarities between dynamics in optical systems and other real-world systems can be found, like e.g. waves in oceans [57], research with coupled SLs can also inspire investigations of other networks of nonlinear nodes and serve as model systems for real-world complex networks. One example here is neuronal dynamics. After zero-lag synchronization had been observed in cats' brains [58], it was found in SLs [42], and then numerically [59, 60] and experimentally [61] in populations of neurons. Motivated by this similarity, brain-inspired data processing schemes have been implemented with (self-)coupled SLs and in optics and photonics in general [48, 62], notably also using VCSELs [63–67]. One of these schemes is reservoir computing (RC), which is a hardware-friendly approach that uses a network (called the reservoir) that contains fixed, recurrent connections between single elements, the network nodes. During a process called training, the output weights are modified according to known input-output combinations to obtain the desired output for every type of input. For more details about RC, see the next section. In this thesis, we use diffractively coupled VCSELs as nodes to implement RC and characterize the system by computing basic benchmark tasks.

1.3 Reservoir computing (RC)

Reservoir computing (RC) [68] is a machine learning approach that uses networks with recurrent connections for information processing. It unifies two concepts that were independently suggested in computational science and machine learning: echo state networks (ESNs) [69, 70] and liquid state machines (LSMs) [71]. A reservoir computer consists of three basic layers, which are sketched in Fig. 1.3: the input, the reservoir, and the output. The reservoir is made up of nodes that are linked via fixed, recurrent connections. Information is fed into the nodes via the input connections that also remain fixed. The connections from the nodes to the output, called output weights, are the only connections that are changed to adapt the system to the desired task. This modification of the output weights is called training.

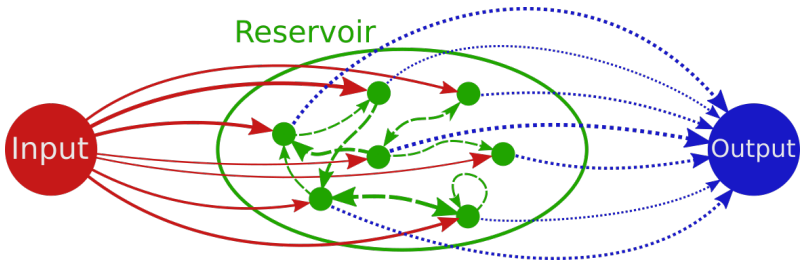

FIGURE 1.3: Reservoir computing (RC) scheme. Via fixed input weights, information is fed into a reservoir with fixed, recurrent connections. During a phase called training, the output weights are adjusted to produce the desired output for a given input.

Data that is fed to the reservoir is mapped onto a state space that is higher-dimensional than the input. The idea behind this is that distinct classes of inputs might not be linearly separable within the generic dimensionality of the input information, but might become linearly separable when mapped onto a higher-dimensional space. Considering this, it becomes clear that for successful information processing, a reservoir computer needs a nonlinearity, since a purely linear mapping cannot increase dimensionality. Furthermore, the reservoir should react similarly to similar inputs to be robust to unavoidable levels of noise in the input, and a reservoir can therefore not be operated in a chaotic state. Still, it should be able to yield sufficiently different outputs for inputs that belong to different

classes. Finally, for processing sequential data, recent inputs should have influence on the current outputs, but this influence should fade.

The fixed internal connections make RC hardware-friendly, since in physical systems it is usually much more difficult to modify internal connections. Consequently, RC has been implemented in several physical systems, like electronic circuits [72], spintronic oscillators [73], and even biological neurons [74]. Some computationally difficult tasks have been solved by reservoir computers that were implemented in physical hardware, e.g. time series prediction [75, 76] or pattern recognition tasks, like speech recognition [62, 73], classification of distorted fiber transmission signals [77], and classification of human actions in videos [78]. In the context of this thesis, especially the numerous successful experimental realizations of RC in optics and photonics systems are interesting.

One powerful approach that has been implemented in photonics uses delay-based reservoirs, a concept that was first demonstrated with an electronic system [72]. Delay-based reservoirs consist of a single physical node with delayed FB. To obtain a sufficient number of nonlinear transients for RC, the input is multiplied with a so-called mask, i.e. a periodic sequence of different values. This defines multiple virtual nodes that correspond to different points of the mask sequence. For delay-based RC, reservoirs with hundreds of nodes have been demonstrated, and they have solved computationally difficult tasks like spoken digit recognition or chaotic time series predicition [62] (see Fig. 1.4a). Recently, this scheme has also been implemented using a VCSEL [66, 79]. However, there is always a tradeoff between the number of nodes and the maximal information processing speed of the reservoir, and the training has been implemented offline on a conventional computer so far.

Another way to define multiple reservoir nodes is by using a spatial light modulator (SLM). In these schemes, connections between the nodes are established via diffraction [48] or scattering [80] (see Fig. 1.4b), the reservoir states are detected using a camera, and reservoirs with thousands of nodes have been demonstrated. These reservoirs have solved advanced tasks, like prediction of the Mackey-Glass time series or prediction of a Kuramoto-Sivashinsky dataset. However, the update rate of the SLM according to the reservoir state detected with the camera currently limits these systems to processing rates of about 100 Hz.

The nodes of a reservoir can also be defined within a large-area VCSEL [67] (see Fig. 1.4c), which guarantees device-inherent coupling between them. The input encoding and the readout are established using digital micromirror devices, which is what currently limits the speed of the system. Notably, the training has been carried out online in this case.

In this thesis, we explore the use of diffractively coupled VCSELs as nodes to implement RC. Here, we measure the output of every VCSEL sequentially and train the system offline. However, implementing output weights with an SLM for parallel readout would be possible. In principle, the system's speed is only limited by the modulation bandwidth of the VCSELs, which is in the GHz range.

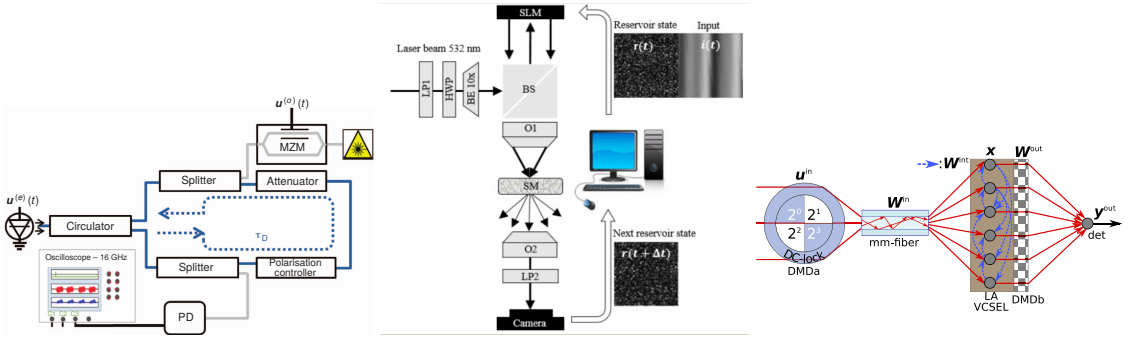

(a) (b) (c)

FIGURE 1.4: Examples for photonic RC implementations. a) RC implementation based on a SL with delayed FB. Figure from [62]. b) Implementation of optical RC using a spatial light modulator (SLM) and a scattering medium. Figure from [80]. c) Photonic RC using a multimode VCSEL. Figure from [67].

1.4 Motivation and overview of this thesis

The objective of this thesis is to diffractively couple and injection lock 25 VCSELs in arrays via an external cavity. There are very few realizations of SL networks of comparable size, although they are interesting from fundamental and applied points of view. Once such a network is established, its fundamental behavior – an example for the dynamics of real-world complex networks at high speed – can be studied. Moreover, it is a promising hardware substrate for RC. This thesis summarizes the results that we have obtained in our experiments with the VCSEL arrays.

In Chapter 2, the VCSEL arrays are introduced, and the diffractive coupling concept is presented in detail, including requirements for coupling, theoretical coupling strengths between VCSELs, and possible deviations. Furthermore, the experimental setup is described in detail and some experimental methods are introduced.

Chapter 3 contains the experimental characterization of the individual VCSELs without coupling. This includes their electrical behavior, their threshold currents, and their slope efficiencies. Also, their modal behavior is analyzed in detail. Finally, the influence of coupling on the individual VCSELs is investigated.

In Chapter 4, the behavior of the VCSELs under diffractive coupling and external optical injection is characterized in detail. After a short explanation of the experimental alignment procedure, we present results for pairwise coupling and coupling of the entire array. For investigating the pairwise coupling, the central VCSEL and one additional VCSEL were switched on. The coupling is analyzed via the optical and radio-frequency spectra of the VCSELs. Last, results on optical injection locking to an external laser and the dynamic response to intensity-modulated injection are shown.

In Chapter 5, the information processing capabilities of the system are explored. The chapter starts with an explanation of how RC can be implemented with diffractively coupled VCSELs. Then, the system's performance on the basic benchmark tasks memory capacity, exclusive or, header recognition, and digital-to-analog conversion is evaluated. The chapter ends with an analysis of the role of the individual nodes.

Chapter 6 contains a summary of the obtained results. Additionally, it gives an outlook to possible future work.

Chapter 2

Methods, devices, and experimental setup

It is essential to know how exactly experimental results were obtained. Therefore, in this chapter, we will introduce the material and methods that were used in our experiments.

2.1 VCSEL arrays

The experiments for this thesis were carried out with custom-manufactured VCSEL arrays. The VCSELs are arranged in a 5×5 square lattice with a pitch $p \approx 80\,\mu\text{m}$, which is the distance between directly, not diagonally, neighbouring VCSELs. Fig. 2.1 contains two microscope images of such an array. As visible in Fig. 2.1a, the p-contacts have the shape of a ¾-ring, whose opening can point in different directions. Via the p-contacts, gold wires, bonding pads, and bonding wires, the VCSELs can be individually electrically contacted, and thus their pump current can be controlled independently. For a detailed description of the VCSEL manufacturing, see Ref. [9]. In the following, only a short overview is given. The VCSELs rely on an AlGaAs/GaAs DBR mirror structure and GaInAs quantum wells with GaAsP barrier layers in the active zone. The aperture is defined by oxidization of an AlGaAs layer into previously defined VCSEL mesas. Crucially, these mesas are slightly elliptical with the difference between the major and minor axis equalling 0.15 µm. With the target aperture size of about 4.5 µm, this leads to an aperture ellipticity of about 3 %.

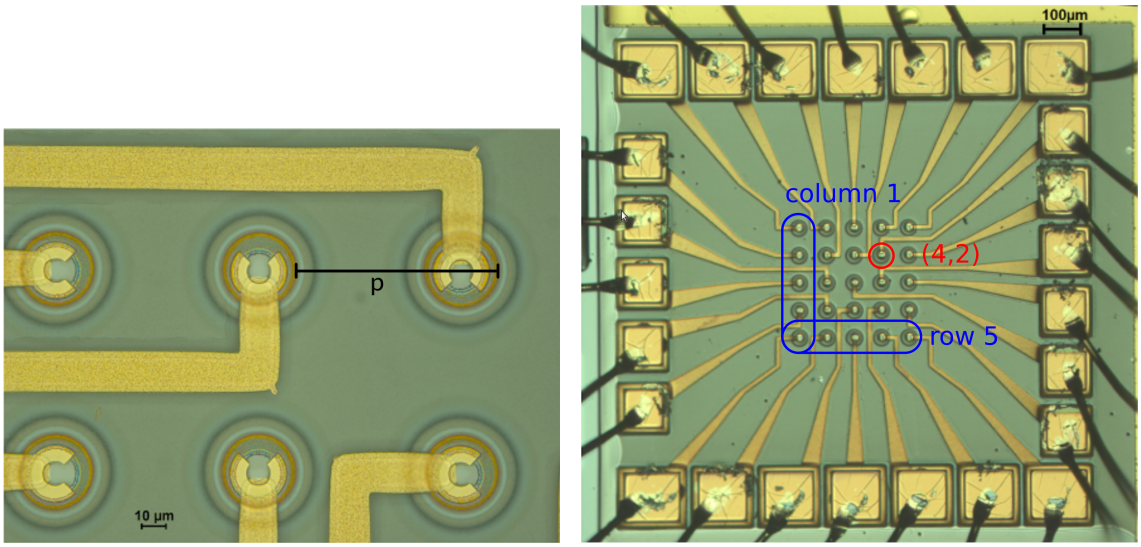

(a) Mesas with ¾-ring shaped p-contacts. The pitch p is the distance between two directly neighbouring VCSELs.

(b) Wirebonded array. VCSEL nomenclature according to column and row in array.

FIGURE 2.1: Microscope images of VCSEL array, from Ref. [9].

Many VCSEL arrays with slightly different pitches p and emission wavelengths were fabricated, since these quantities have to fulfil Eq. 2.5 – introduced in the next section

– to allow for coupling emitters via our intended scheme. We selected three arrays for wirebonding. Most of the experimental results that are presented in this thesis were obtained with one array to which we will refer as array 5 of chip 2. Some results in Sec. 3.3 were obtained with an array from the same semiconductor chip to which we will refer as array 1 of chip 2. For individual VCSELs, we define a nomenclature as shown in Fig. 2.1b. The VCSEL in column c and row r of the array is referred to as VCSEL (c, r), where the columns are numbered from left to right and the rows from top to bottom when looking at the VCSEL array as mounted in the experimental setup with the optical table at the bottom. VCSEL (3,3) is sometimes referred to as the central VCSEL, while the remaining VCSELs can be named non-central.

Unfortunately, during the wirebonding, some pairs of VCSELs were short-circuited at the bonding pads. For array 1, VCSELs (1,1) and (2,2) are short-circuited. For array 5, there are three short-circuited pairs of VCSELs: (2,1) & (3,2), (3,1) & (3,3), and (4,1) & (5,1). This leaves us with 19 individually addressable VCSELs and 3 pairs of VCSELs that can only be biased together. We will assume an equal distribution of the pump current between two VCSELs of the same pair.

2.2 Coupling emitters via diffraction in an external cavity

We aim to achieve coupling of next and second-to-next neighbouring VCSELs via diffraction in an external cavity. For this, we use a diffractive optical element (DOE, Holoor MS-261-970-Y-X) that acts similar to a diffraction grating. When a collimated beam of coherent light passes through this DOE, it is split into a 3×3 square pattern of beams, as shown in Fig. 2.2a. The central beam of this pattern passes the DOE without change of direction. The angles $\theta_n^{\pm}$ between the (not diagonally) neighbouring beams and the optical axis can be calculated via

$$a \cdot \sin(\varphi_n) \pm \lambda = a \cdot \sin(\theta_n^{\pm}), \tag{2.1}$$

where λ is the wavelength of the light, a is the DOE constant, which is similar to a grating constant, and φ_n is the angle between the incoming beam and the optical axis (s. Fig. 2.2b).

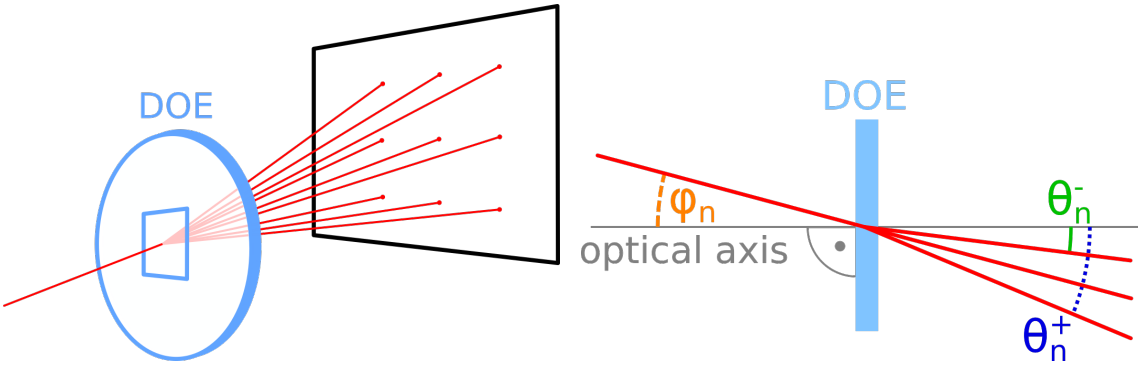

(a) Beam multiplexing into 3×3 pattern. (b) 2D projection of DOE diffraction angles.

FIGURE 2.2: Spatial multiplexing of a collimated beam of coherent light at the diffractive optical element (DOE).

From Eq. 2.1, we can derive the condition for coupling between neighbouring VCSELs by approximating the light propagation through everything but the DOE with ray optics. In our experiment, the central VCSEL of the array is aligned to the optical axis. The emission of all VCSELs is collimated with a microscope objective (MO, $f_{\mathrm{MO}} = 9.0\,\mathrm{mm}$,

NA = 0.45, Olympus LCPLN20XIR), split by the DOE, and focussed by an achromatic lens (L1, $f = 80\,\mathrm{mm}$, Thorlabs AC254-080-B) onto a dielectric mirror (Thorlabs BB1-E03), where it is reflected back at the array through the optical elements. How the principal rays of different VCSELs pass through this external cavity is sketched in Fig. 2.3. To derive the coupling criterion, we define φ_n as the angle of the incoming beam of one VCSEL and thus its 0th diffraction order at the DOE. With l_n being the distance of that VCSEL from the optical axis and f_{MO} being the focal distance of the microscope objective, we obtain

$$\varphi_n = \arctan\left(\frac{l_n}{f_{\mathrm{MO}}}\right). \tag{2.2}$$

As hinted in Fig. 2.3, the DOE's 0th diffraction order is coupled back into the VCSEL from which it was emitted. Thus, the coupling criterion is

$$\varphi_{n\pm1} = \theta_n^{\pm}, \tag{2.3}$$

where $\varphi_{n\pm1}$ is the angle between the incoming beam of a neighbouring VCSEL and the optical axis. Inserting the pitch p and Eqs. 2.2 and 2.1 into Eq. 2.3, we obtain

$$\arctan\left(\frac{l_n \pm p}{f_{\mathrm{MO}}}\right) = \arcsin\left(\sin(\varphi_n) \pm \frac{\lambda}{a}\right) = \arcsin\left(\frac{l_n}{\sqrt{l_n^2 + f_{\mathrm{MO}}^2}} \pm \frac{\lambda}{a}\right). \tag{2.4}$$

Using the paraxial approximation, which also implies $l_n \ll f_{\mathrm{MO}}$, we simplify this to

$$\frac{p}{f_{\mathrm{MO}}} = \frac{\lambda}{a}. \tag{2.5}$$

We based the drawing in Fig. 2.3 on ray optics considerations and sketched the principal rays of the emission of different VCSELs in different colors. The reflected rays are sketched on the right to avoid confusion. DOE diffraction orders are distinguished by line styles. Diffraction at the second DOE pass is only shown for the 1st diffraction order of the central VCSEL. The figure shows how the diffractive orders of different VCSELs overlap at the VCSEL surfaces after reflection. Note that this scheme is the same as the one employed in Refs. [48, 81].

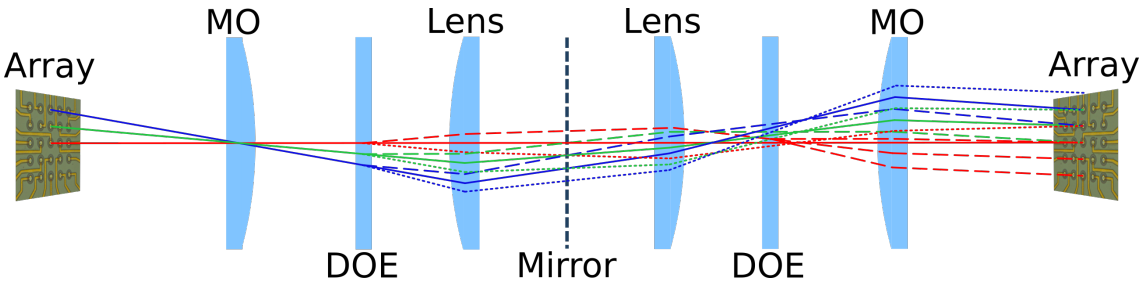

FIGURE 2.3: Schematic of principal rays in the experiment. The image is mirrored for better overview. Rays originating from different VCSELs are differentiated by color, diffraction orders of the first DOE pass by line style. Diffraction at the second DOE pass was sketched in only one case to avoid additional overlap. Not to scale.

In Fig. 2.4, the theoretical distribution of the light intensity of one emitter after the second DOE pass is given. The 3×3 square lattice pattern of equal intensity that forms after the first DOE pass is indicated by circles with light blue background and black arrows. The 5×5 square lattice pattern with non-homogeneous intensities originates from overlap after the second diffraction. The relative intensities $C_{\mathrm{DOE}}(c, r)$ at column c and

row r of the pattern are proportional to the number of diffraction orders that overlap there, divided by 81. In Fig. 2.4, $C_{\mathrm{DOE}}(c,r)$ is given in percent inside the circles, and the number of overlapping diffraction orders is given by the number of arrows that point to that point, plus one for the inner points.

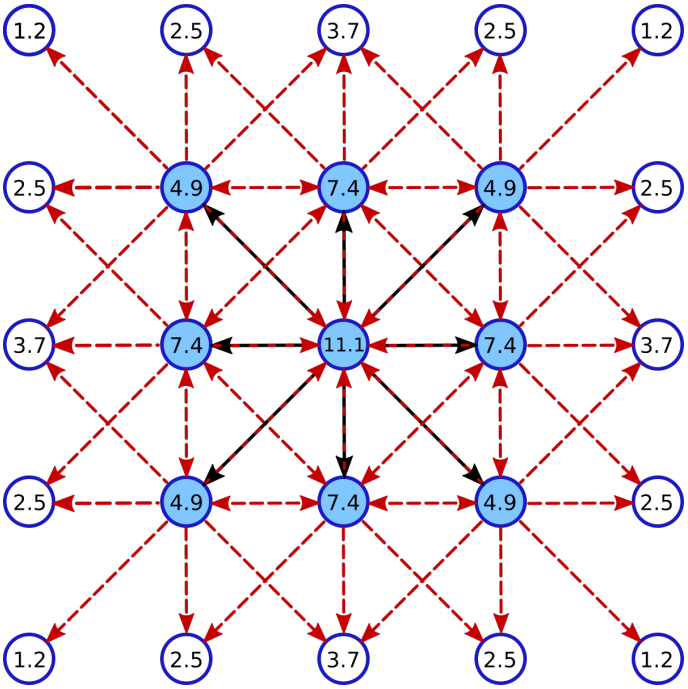

FIGURE 2.4: Diffraction pattern after light emitted at the center passes the DOE twice. Numbers indicate $C_{\mathrm{DOE}}(c,r)$, the relative intensity to the incoming beam in percent at column c and row r. Circles with light blue background and black arrows represent the diffraction pattern after a single pass through the DOE; dashed red arrows and circles with white background represent the pattern after a double pass. Image reproduced from Ref. [81, p. 15].

To calculate the coupling mismatches, we will limit ourselves to the one-dimensional case, i.e. to VCSELs in the same row (or column) as the central VCSEL (3,3). We define the mismatch d for the coupling between two VCSELs as the distance from the center of one VCSEL to the position on the array surface for which we expect the maximum of the diffractive coupling beam of another VCSEL . In this case, the mismatch d as a function of a with fixed p, λ, and f_{MO} is given by

$$d = \left| \tan\left(\arcsin\left(\frac{k_1 p}{\sqrt{(k_1 p)^2 + f_{\mathrm{MO}}^2}} + (k_2 - k_1)\frac{\lambda}{a} \right) \right) f_{\mathrm{MO}} - k_2 p \right|, \tag{2.6}$$

where $k_1 = r_1 - 3$ and $k_2 = r_2 - 3$ are the distances of both involved VCSELs from the center, in units of p, with r_1 and r_2 being the rows of these VCSELs. This is plotted in Fig. 2.5 together with the mismatch calculated directly from the paraxial approximation for direct and for second neighbours. We observe that, for our array size and perfect alignment, deviations from the paraxial approximation do not cause significant mismatches. For the relevant range, we can approximate the mismatch for direct neighbours by $d \approx 0.75\,|a - a_0|$, and for second neighbours by $d \approx 1.5\,|a - a_0|$, where $a_0 = \lambda f_{\mathrm{MO}}/p$.

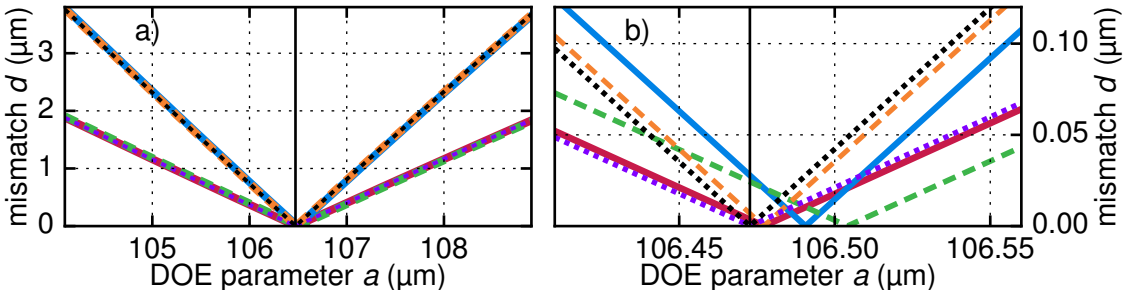

FIGURE 2.5: a) Coupling mismatch vs. DOE parameter a for $p = 82.5\,\mu\text{m}$, $f_{\text{MO}} = 9.0\,\text{mm}$, and $\lambda = 976\,\text{nm}$. b) Zoom into a). Solid red line: coupling of central VCSEL ($k_1 = 0$) and direct neighbour ($k_2 = 1$). Solid blue line: $k_1 = 0$ and $k_2 = 2$. Dashed green line: $k_1 = 1$ and $k_2 = 2$. Dashed orange line: $k_1 = -1$ and $k_2 = 1$. Dotted violet line and dotted black line: Mismatch calculated from the paraxial approximation. Horizontal solid black line: $a_0 = \lambda f_{\text{MO}}/p$.

2.3 Experimental setup

To conduct the experiments, the VCSEL chips with the arrays that are described in Sec. 2.1 were installed into an experimental setup, which is described in this section. All part numbers and the most important related technical details are summarized on p. 81.

2.3.1 VCSEL mounting

Fig. 2.6 gives an overview over how the VCSELs were mounted. The chips, which typically contain 16 arrays of 5×5 VCSELs, were fixed on a ceramic quad flat package (CQFP, Kyocera PB23866) with silver conductive paste. The desired arrays were contacted by wire-bonding the bonding pads to the CQFP contact stripes. Then, the CQFP was placed into a small custom-designed printed circuit board (PCB), which serves as a submount for the VCSELs. Its position and angle can be varied with micrometer screws and its orientation was aligned such that the array's rows are parallel to the optical table. At the back of the small PCB, we installed a thermistor, a copper block, and a Peltier element for stabilizing the chip temperature (thermistor and chip visible in Fig. 2.6). Their thermal contact with the CQFP was established using thermal paste. Using coaxial cables, the VCSELs' contacts on the edge of the small PCB were electrically connected to a larger PCB, which was also custom-designed. The design of this larger PCB, together with an Arduino microcontroller and a Labview program, allows for individual control of the pump currents $I(c,r)$ of all the VCSELs (c,r), with a pump current dependent 8-bit resolution of about 0.01 mA close to $I(c,r) \approx 0.2\,\text{mA}$ and roughly 0.1 mA close to $I(c,r) \approx 2.0\,\text{mA}$.

2.3.2 Optical free-space setup

As shown in the rightmost image in Fig. 2.6, the large PCB is mounted on an optical table, where an optical free-space setup is constructed out of several optical elements. In Fig. 2.7, this experimental setup is sketched schematically (and not to scale). For better overview, we separated the setup in three parts: the external cavity containing the VCSELs, the injection arm, and the measurement arm. We define the z-axis as the direction of propagation of the VCSELs' emission, the x-axis as being parallel to the optical table and orthogonal to the z-axis, and the y-axis as orthogonal to the optical table.

How the light passes the external cavity, i.e. the MO, the 50/50 beam splitter (BS1, Thorlabs BS014), the DOE, and the achromatic lens before being reflected at a mirror, is

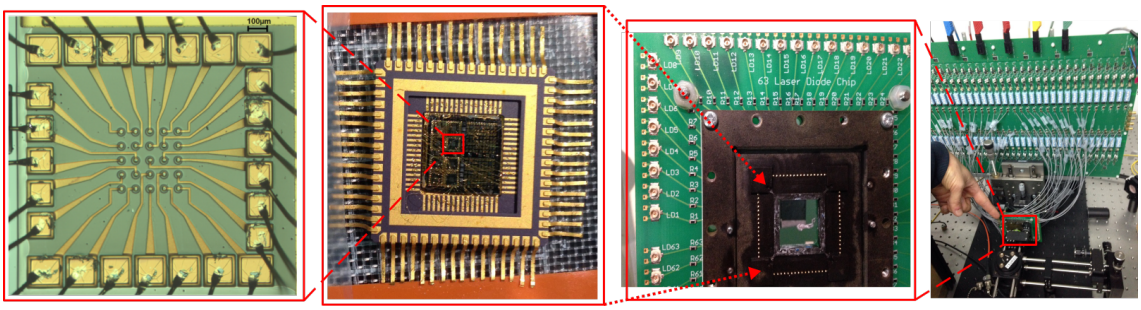

FIGURE 2.6: VCSEL mounting. One VCSEL chip contains various arrays (left, copied from Ref. [9]). The VCSEL chip is fixed with silver conductive paste onto a ceramic quad flat package (CQFP) that serves as a VCSEL submount (center left). Up to two arrays are contacted via wire-bonding. The CQFP is placed into a custom-designed small printed circuit board (PCB) for precise positioning and temperature control (center right). The small PCB is connected to a large PCB (right, hand for scale). This large PCB, together with a microcontroller and a computer program, allows for individual control of the VCSELs' pump currents.

described in the previous section. The MO was mounted on a µm-precision z-axis translation mount. To avoid or attenuate the FB, the light can be blocked or neutral density filters can be introduced between BS1 and DOE.

In the injection arm, the light from an external injection laser (inj, Thorlabs DBR976PN) passes a Mach-Zehnder modulator (MZM, Eospace AZ-0K5-10-PFA-PFA-970), where its intensity is modulated. The light that is emitted from the polarization-maintaining fiber tip is collimated using an aspheric lens (L2, Thorlabs AL1225-B, $f = 25\,\mathrm{mm}$, NA = 0.23) and it is polarization-aligned to the VCSEL emission using a $\lambda/2$ waveplate (Thorlabs WPH10M-980). It enters the external cavity via reflection at BS1 and passes the DOE twice before being injected into the VCSELs. This results in its intensity being split up according to Fig. 2.4. An arbitrary waveform generator (AWG, Tektronix AWG7122B, 12 GS/s), whose signal first passes a tunable electrical attenuator (att) and then a broadband electrical amplifier (amp, SHF 826H) is connected to the radio-frequency (RF) port of the MZM. The amp is necessary since the direct output of the AWG does not cover the full range of the MZM's modulation, while the att is needed to prevent damage to the amp. The MZM is biased to the point of maximal slope of its $\sin^2$ nonlinearity by applying U_{bias} with an electrical sourcemeter (ES, Keithley 2611B) to the DC port. To find this point, the AWG's output is set to a periodic triangular function and U_{bias} is adjusted aiming for a symmetric sine signal. When defining an injection time series for the AWG, one has to take into account that the injection laser's intensity will be modulated according to the $\sin^2$ nonlinearity of the MZM and not directly to the AWG's output.

The VCSELs' emission enters the measurement arm after being reflected at BS1. The portion that passes the 30T/70R beam splitter (BS2, Thorlabs BS023) is coupled into a single-mode (SM) fiber using an aspheric lens (L3, Thorlabs AL2018, $f = 18\,\mathrm{mm}$). This SM fiber's position serves as a reference for the optical alignment when maximizing the fiber-coupled intensity that is measured with an optical powermeter (PowM). In some experiments, this signal is split, and part of it is fed into the optical spectrum analyzer (OSA, Anritsu MS9710C, FWHM resolution = 50 pm). The portion that is reflected at BS2 is fiber-coupled using a plano-convex lens (L4, Thorlabs LA1027-B, $f = 34.9\mathrm{mm}$). For measurements with the OSA, it is coupled into an SM fiber. For measurements with the oscilloscope (Osci, Lecroy Wavemaster 816Zi, 16 GHz bandwidth, 40 GS/s) or the electrical spectrum analyzer (ESA, Anritsu MS2667C, 9 kHz to 30 GHz), the reflected part is

coupled into a multimode (MM) fiber, which is connected to a photodiode (PD, New Focus 1554-A-50PD, 10 kHz to 12 GHz 3-dB-bandwidth), which in turn converts the optical signal to an electrical one. The injection laser signal also enters the measurement arm, where it overlaps with the emission of the central VCSEL, making isolated detection of the central VCSEL's signal with injection impossible.

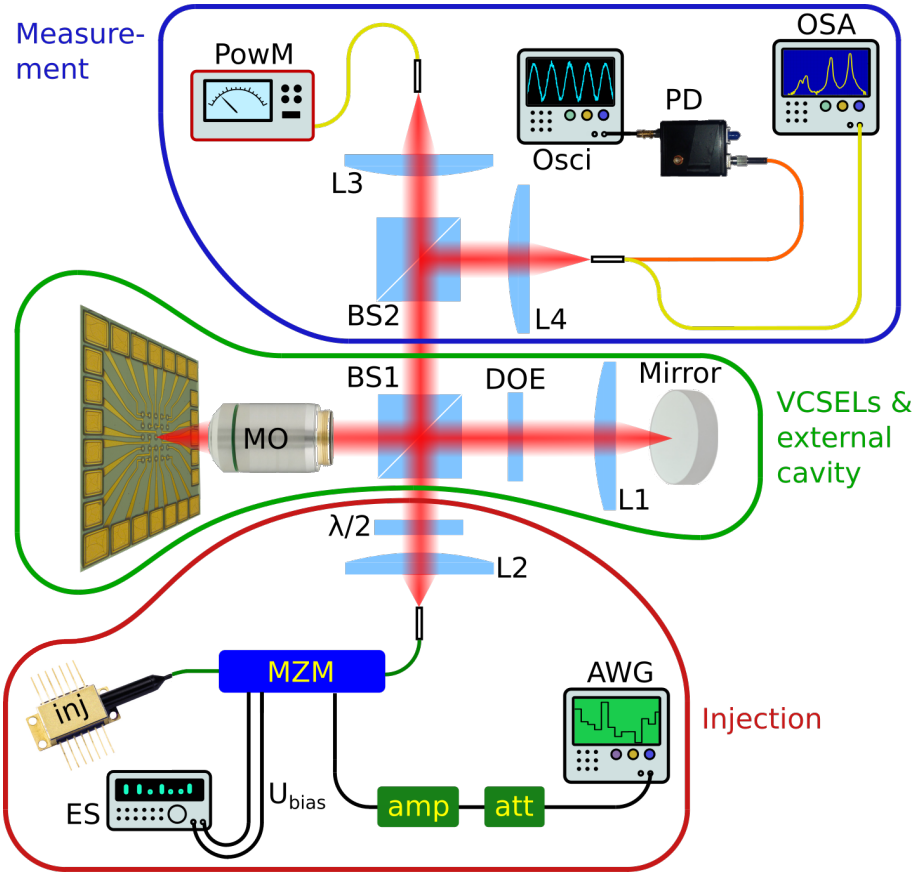

FIGURE 2.7: Schematic experimental setup. An external cavity is formed by a microscope objective (MO), a lens (L1) and a mirror. A diffractive optical element (DOE) creates beam copies, establishing coupling between VCSELs and enabling simultaneous injection into all the VCSELs of the array. The injection branch consists of a DBR injection laser (inj), whose intensity is modulated using a Mach-Zehnder modulator (MZM), which in turn is biased using an electrical sourcemeter (ES). The output of an arbitrary waveform generator (AWG) passes an electrical attenuator (att) and an electrical amplifier (amp) before entering the MZM's radio-frequency (RF) port. The intensity-modulated light passes an aspheric lens (L2) and a half-wave plate ($\lambda/2$). Via reflection at a 50/50 beam splitter (BS1), the injected signal enters the external cavity and the VCSEL signal enters the analysis branch, which contains a 30T/70R beam splitter (BS2), an aspheric (L3) and a plano-convex lens (L4), an optical spectrum analyzer (OSA), a powermeter (PowM), a photodiode (PD), an electrical spectrum analyzer (ESA), and an oscilloscope (Osci). Green lines represent PM fiber, orange lines MM fiber, yellow lines SM fiber, and black lines coaxial cables. Not to scale. For part numbers and the most important technical details, see p. 81.

2.3.3 Alignment

To allow for precise alignment of the setup, we use a cage rod system, in which critical optical elements are mounted on mechanical stages with micrometer precision. All the lenses, including the MO, are mounted on z-axis translation mounts with 50 µm travel

per revolution. All the fiber tips and the small PCB with the VCSELs are fixed on x-y-translation mounts with 25 µm and 50 µm travel per revolution, respectively. To adjust its tilt, the small PCB is additionally mounted on two goniometers with a precision of 10 arcmin, which is the same precision as the one of the DOE's rotation mount. The mirror is mounted on a mechanical x-y-tilt stage that tilts less than 10 mrad per revolution.

As a first alignment step, x-y and z-position of reference fiber, L3 (top of Fig. 2.7), and small PCB (and thus VCSEL array) are approximately adjusted using pinholes and detector cards. For this, the central VCSEL is switched on, an external laser is connected to the outer end of the reference fiber (i.e., the end that in Fig. 2.7 is connected to the PowM), and we aim for the emitted beams of both to be collimated and parallel to the cage system. As a next step, the beam splitters are inserted and their rotation and tilt are adjusted, and so is the tilt of the mirror, using pinholes for both. The VCSEL array's x-y-z position is optimized by biasing it close to threshold and maximizing its optical output power. The idea is to aim for the largest threshold reduction by maximizing the self-FB and thus optimize the VCSEL position. Then, the coupling into the reference fiber is optimized by adjusting the reference fiber's x-y-z position. Since the position of the VCSEL array relative to the cage system is not fixed with direct connections and we have observed that it drifts over time, it is necessary to realign it before taking measurements. Having established the SM fiber as an alignment reference, we can easily realign the position of the VCSEL array via optimization of the coupling into the reference fiber by adjusting the VCSEL array's x-y-z position. After that, we insert L1 into a µm-precision z-axis translation mount at one focal distance f_{L1} from the mirror. We fine-tune this distance using two different methods. First, as before, we maximize the threshold reduction of the central VCSEL. Second, we introduce a lens and a complementary metal-oxide-semiconductor (CMOS) camera into the injection arm. Connecting an external laser to the outer end of the reference fiber, we adjust the relative position of camera and lens such that the light of the external laser is focussed on the camera. Having established this reference, we verify that the beam of the central VCSEL is focussed onto the CMOS camera. With this, most of the optical elements in the external cavity are aligned. The alignment of the DOE angle ν is described in Sec. 4.1. Some other alignment steps of optical elements in the injection and measurement arm that are very similar to the ones described above are not explicitly described.

2.4 Data acquisition

This section contains additional explanations about how the data were acquired. Note that most abbreviations have been introduced in the previous section.

2.4.1 Polarization control and measurement

To control and measure the polarization of the laser light, we used a linear polarizer (Thorlabs LPNIR050-MP) and a $\lambda/2$ waveplate. To calibrate the linear polarizer on its cage system rotation mount, we used a white light source and a polarizing beam splitter cube (PBS, Thorlabs CM1PBS253). Using a free-space powermeter, we measured the angle-dependent transmission through the linear polarizer after the white light had been transmitted through or reflected at the PBS. This is shown in Fig. 2.8, where we obtain angular offsets of 10° and 100°, respectively, from sinusoidal fits to the data points.

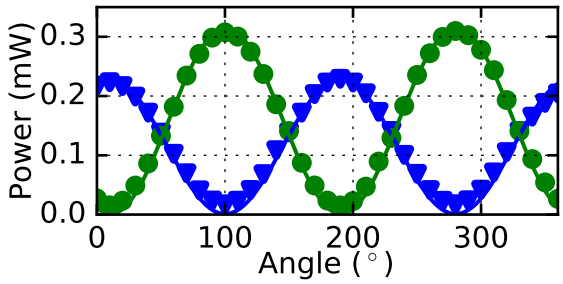

FIGURE 2.8: Power of polarized light transmitted through the linear polarizer. Blue triangles: transmission of parallel-polarized light through the polarizing beam splitter cube (PBS). Green circles: reflection of orthogonal-polarized light through the PBS. Lines: sinusoidal fits.

2.4.2 Recording optical spectra

To record optical spectra, we couple the laser light into an SM fiber that is connected to the OSA, which has an FWHM resolution of 50 pm, an optical reception sensitivity of -90 dBm, and a dynamic range of 70 dB. Note that, due to the experimental geometry (see Subsec. 2.3.2 – especially Fig. 2.7), the outputs of the central VCSEL $(3,3)$ and of the injection laser cannot be collected separately. The output of the injection laser is significantly stronger than that of the central VCSEL, and consequently saturates optical measurements before they can reveal signatures of VCSEL $(3,3)$. We therefore did not obtain meaningful optical spectra, RF spectra, or time series of the central VCSEL in experimental measurements with injection. An example spectrum is shown in Fig. 2.9. We record data points with a minimal spacing of 2 pm. To determine the peak wavelengths, we first smooth the spectra with a second order binomial filter and determine either the global maximum of the power spectral density (PSD) or local peaks with the Python module 'detect_ peaks'. Then, we determine the two data points on both sides of the peak, between which the PSD crosses the line of 3 dB below the peak value. Here, we linearly interpolate the exact coordinate of the -3 dB crossing from these two points and obtain the peak as the midpoint between both of these crossings. Throughout this whole thesis, we always used this method to determine the peak wavelengths precisely. Importantly, on different measurement days, the wavelengths recorded at the same pump current and target temperature of the Peltier element varied. We suspect an inconstant OSA offset as the reason for this, although the variation of the lab temperature could also contribute to this.

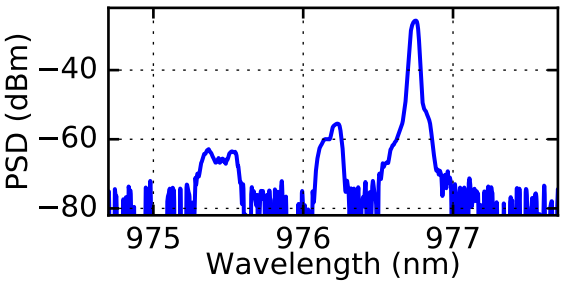

FIGURE 2.9: Optical spectrum of VCSEL (2,3) at $I = 3.0\, I_{\mathrm{th}}$.

2.4.3 Recording intensity dynamics

To record the intensity dynamics of the lasers, we couple their light into an MM fiber that is connected to the PD, which has a 3-dB-bandwidth of 10 kHz to 12 GHz. The PD generates an electrical signal that we feed into the ESA or into the oscilloscope. The ESA can detect signals from 9 kHz to 30 GHz, and the oscilloscope has a sampling rate of 40 GS/s and an analog bandwidth of 16 GHz. To eliminate background peaks in the ESA spectra, we record background spectra, and subtract them from the rest of the spectra, taking into account that the scale is logarithmic and the values are given in dBm. This is shown in Fig. 2.10. For information about how we obtain the reservoir output from the oscilloscope time series, see Subsec. 4.4.2.

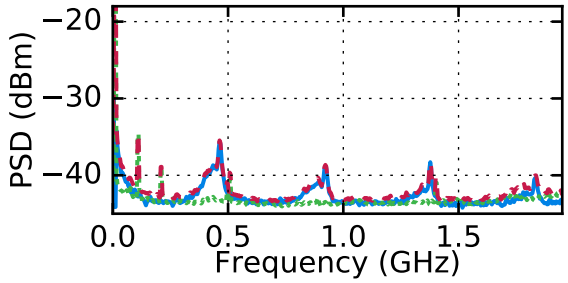

FIGURE 2.10: Solid blue line: RF spectrum of VCSEL (3,3) with self-feedback, background subtracted. Dashed red line: Same spectrum without subtracting the background. Dotted green line: Background spectrum.

Chapter 3

Characterization of individual VCSELs

In this chapter, basic VCSEL characteristics and their behaviour under self-FB are analyzed. Unless specified differently, all the shown results were obtained with chip 2 array 5, the same VCSEL array that was used for the experiments in Chaps. 4 and 5.

3.1 Basic characteristics

In Fig. 3.1, the current-voltage (I-U) characteristics of VCSELs (2,3), (3,2), and (5,3) are shown. They were measured by connecting an electrical sourcemeter to the VCSEL mount, such that only one VCSEL at a time was contacted. For most of the VCSELs, we measure I-U characteristics that are very similar to the one of VCSEL (2,3), making the array mostly homogeneous in this regard. Still, there are a few outliers, such as VCSEL (3,2), see Fig. 3.1. The reason is that it is short-circuited with VCSEL (2,1). When correcting for that by halving the current, the I-U characteristics of the individual VCSELs of the short-circuited pairs (3,2) & (2,1) and (3,3) & (3,1) resemble the one of (2,3) and thus of most of the VCSELs. This leaves us with three actual outliers: The short-circuited pair (4,1) & (5,1) and the individual VCSEL (5,3). These three VCSELs behave differently not only regarding their I-U characteristics, but also regarding their thresholds, as will be discussed in the next paragraph.

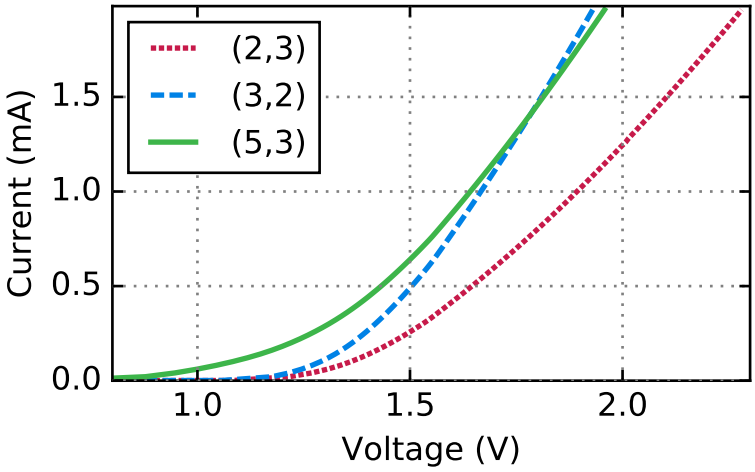

FIGURE 3.1: Current-voltage (I-U) characteristics of three VCSELs. Most I-U characteristics of VCSELs in array 5 were very similar to the one of VCSEL (2,3).

In Fig. 3.2, the optical power-current (P-I) characteristics of four different VCSELs are shown. They were measured by placing a free-space optical powermeter in front of the mounted array while controlling the pump currents via the control unit. For VCSEL (3,2), both current and optical power were halved, since due to the short-circuit with VCSEL (2,1) both P-I curves were measured simultaneously. Still, by blocking the collimated light of one VCSEL with a pinhole, we obtained separate data for the VCSELs that form short-circuited pairs and verified that their thresholds do not differ significantly. The slope

efficiency cannot be measured reliably separately for the VCSELs of a short-circuited pair. To determine the threshold current I_{th} and the slope efficiency η, we fit the P-I curves linearly for $30\,\mu\mathrm{W} \leq P \leq 100\,\mu\mathrm{W}$. From there, we extract I_{th} as the zero crossing of the linear fit and η as its slope. These results are summarized in Tabs. 3.1 and 3.2. We observe that most of the VCSELs behave homogeneously regarding their P-I characteristics. The notable exceptions are VCSEL (5,3), the short-circuited pair (4,1) & (5,1), and VCSEL (2,4). In the first two cases, where I_{th} is higher than for the other VCSELs and η is lower, the I-U characteristics also differ significantly from the rest, while for VCSEL (2,4) only η is smaller than for most of the VCSELs. From Tab. 3.1, we calculate an average threshold current $\overline{I_{\mathrm{th}}} = (0.364 \pm 0.120)\,\mathrm{mA}$, which decreases to $(0.323 \pm 0.025)\,\mathrm{mA}$ when excluding the outliers, i.e. VCSELs (5,3), (4,1), and (5,1). Similarly, from Tab. 3.2, we calculate an average slope efficiency $\overline{\eta} = (0.244 \pm 0.036)\,\frac{\mu\mathrm{W}}{\mu\mathrm{A}}$, which increases to $(0.258 \pm 0.016)\,\frac{\mu\mathrm{W}}{\mu\mathrm{A}}$ when excluding VCSELs (2,4), (5,3), (4,1), and (5,1).

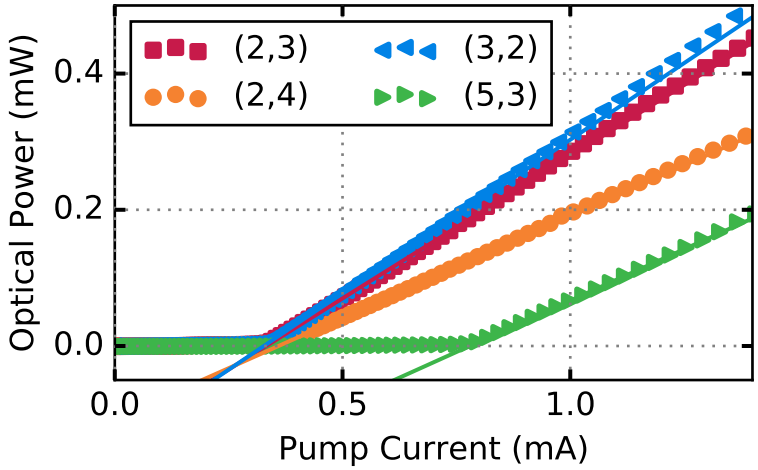

FIGURE 3.2: Optical power vs. pump current (P-I) characteristics of four VCSELs (c, r) (scatter) with linear fits (lines) to obtain the threshold currents $I_{\mathrm{th}}(c, r)$ and the slope efficiencies $\eta(c, r)$. For the P-I curve of VCSEL (3,2), both current and power have been halved to correct for the short-circuit with VCSEL (2,1). Most VCSELs' P-I characteristics were very similar to the one of VCSEL (2,3).

TABLE 3.1: I_{th} of the VCSELs of array 5.

I_{th}(mA)	(1,*)	(2,*)	(3,*)	(4,*)	(5,*)
(*,1)	0.31	0.35	0.31	0.60	0.62
(*,2)	0.30	0.32	0.33	0.29	0.33
(*,3)	0.32	0.33	0.30	0.31	0.78
(*,4)	0.32	0.36	0.33	0.32	0.31
(*,5)	0.31	0.36	0.33	0.27	0.39

TABLE 3.2: Slope efficiency η of the VCSELs of array 5.

$\eta\left(\frac{\mu W}{\mu A}\right)$	(1,*)	(2,*)	(3,*)	(4,*)	(5,*)
(*,1)	0.26	SC with (3,2)	SC with (3,3)	0.17	SC with (4,1)
(*,2)	0.27	0.26	0.25	0.27	0.25
(*,3)	0.26	0.23	0.25	0.27	0.17
(*,4)	0.27	0.17	0.24	0.22	0.28
(*,5)	0.27	0.27	0.28	0.27	0.24

3.2 Transverse modes

In Fig. 3.3, optical spectra of four different VCSELs at different pump currents are shown. For recording the data, the emission of the respective VCSEL was coupled into a single-mode fiber and fed into an optical spectrum analyzer (OSA), as described in Subsec. 2.4.2. The VCSEL chip temperature was stabilized at 19 °C. On the y-axis, the pump current is given in units of the threshold current I_{th} of the respective VCSEL. The colors represent the power spectral density (PSD) at the wavelength given on the x-axis. All VCSELs (also the ones for which no data is shown) emit at similar wavelengths between 975 nm and 977.5 nm for $I \leq 6 \cdot I_{\mathrm{th}}$. For all VCSELs, the longest-wavelength peak is the most intense one up to at least $I = 3 \cdot I_{\mathrm{th}}$, with a side-mode suppression ratio of at least 15 dB for $I < 2 \cdot I_{\mathrm{th}}$. As we will show later (Fig. 3.5), it corresponds to the 0th order mode. We define the wavelength of this peak for VCSEL (c, r) as $\lambda(c, r)$, and determine it as described in Subsec. 2.4.2. It ranges from 976.59 nm to 976.77 nm at $I = 2 \cdot I_{\mathrm{th}}$ for the different VCSELs. At higher pump currents, more peaks appear at lower wavelengths. First, for all VCSELs, 1st order modes appear at a wavelength 0.5 nm below the ground mode. Increasing I further, for most VCSELs, 2nd order modes appear 1.0 nm below the ground mode. For some VCSELs, like (1,4), the 1st order mode results in a double-peak, while for others, the peak rather exhibits a shoulder, and for VCSEL (3,4) it is a single peak. Note that all the lines are broadened, since the FWHM resolution of the OSA is 50 pm ($\widehat{=}$16 GHz). In measurements with a grating and a CCD camera (data not shown), the upper boundary for the linewidth above threshold was shown to be 16 pm ($\widehat{=}$5 GHz). The VCSELs' actual linewidth is thus in the order of 10 pm. Additionally, for other arrays from the same manufacturing process, the FWHM linewidth of the on-chip VCSEL resonance below threshold was measured as 11 pm ($\widehat{=}$3.5 GHz) [82].

The increase of $\lambda(c, r)$ (redshift) with the pump current is not completely linear. It increases faster at higher pump currents. Still, it is approximately 0.24 nm/mA within the range $1.3 \cdot I_{\mathrm{th}} < I < 5 \cdot I_{\mathrm{th}}$ for most VCSELs. For VCSEL (5,3) and the pair (4,1) & (5,1), the emission wavelength increases more slowly with the pump current, at about 0.15 nm/mA. There is also a linear redshift with the chip temperature by about 69 pm/°C for all the VCSELs. Both redshifts affect all the spectral peaks equally. Since pumping a VCSEL locally heats up the chip, it also influences the emission wavelength of the other VCSELs. Thus, for finding conditions under which the wavelengths of all the VCSELs can be maximally matched, we completed two measurement series for every VCSEL. For the first one, which is shown for four VCSELs in Fig. 3.3, only the respective VCSEL was pumped, while all the other VCSELs were switched off. From this, for every VCSEL (c, r), we determined the pump current $I_0(c, r)$ such that $\lambda(c, r) = \lambda_0 = 976.75\,\mathrm{nm}$. We then set the pump current of all VCSELs but one to their respective $I_0(c, r)$. For this one VCSEL, we recorded optical spectra at different pump currents and repeated this procedure for all VCSELs. Under these new conditions, we observed a redshift between 40 pm and 60 pm compared to the emission of the solitarily pumped VCSEL.

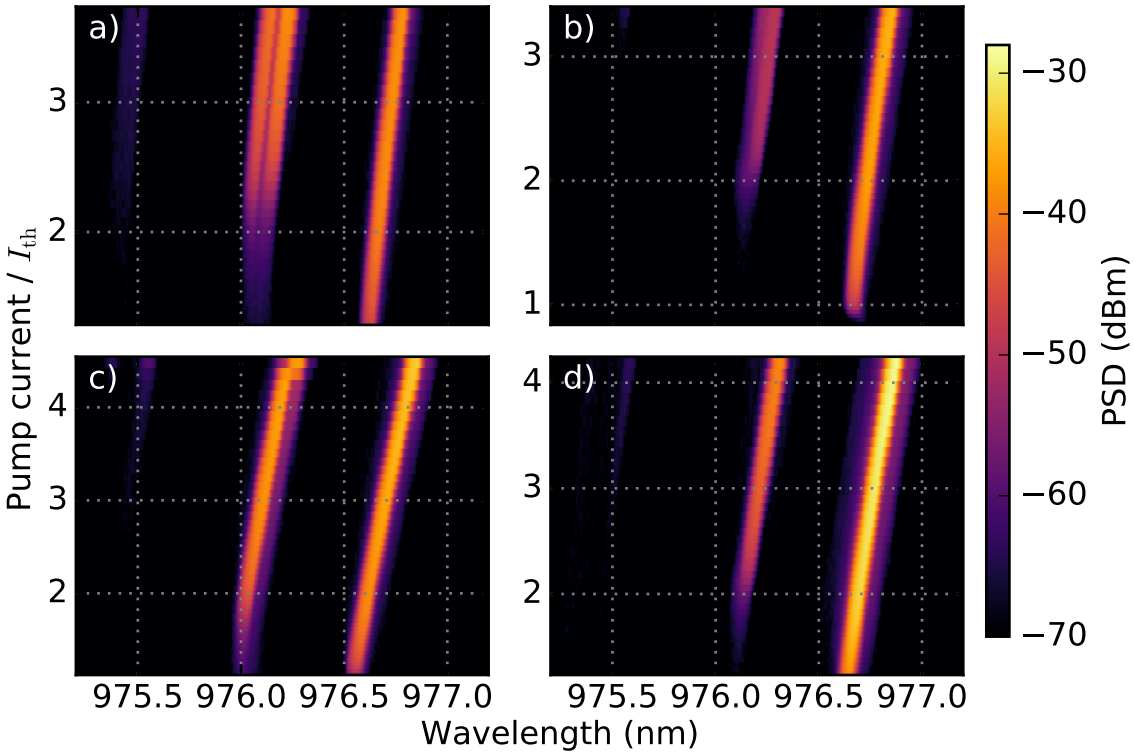

FIGURE 3.3: Optical spectra of four VCSELs at different pump currents. Pump current given in units of the respective threshold current I_{th} (s. Tab. 3.1). Absolute power spectral densities might vary between VCSELs due to different fiber-coupling efficiencies. a) VCSEL (1,4), b) VCSEL (2,5), c) VCSEL (2,4), d) VCSEL (3,4).

To spectrally align the VCSELs, we determined $I_{match}(c,r)$ for every VCSEL (c,r) such that $\lambda(c,r) = \lambda_{match} = 976.81\,nm$ while all the other VCSELs were pumped at $I_0(c,r)$. In Tab. 3.3, $I_{match}(c,r)$ is listed in units of I_{th} of the respective VCSEL. Since some VCSELs cannot be tuned independently due to a short-circuit, it is impossible to spectrally align all of them. Still, for a given I, λ differed less than 0.02 nm between VCSELs of the pairs (2,1) & (3,2) and (4,1) & (5,1), while it differed more than 0.1 nm between VCSELs (3,1) & (3,3). The pump current configuration given in Tab. 3.3 (or a slightly modified one) was used for many of the measurements described in the following chapters. As described in Subsec. 2.4.2, λ_{match} could vary due to lab temperature or an inconstant OSA offset, which is why we usually use the pump currents as a reference rather than the emission wavelengths.

TABLE 3.3: Pump current for spectrally aligning the VCSELs of array 5, given in units of their threshold current I_{th}. Some VCSELs could not be pumped independently due to a short-circuit (SC).

I_{match}/I_{th}	(1,*)	(2,*)	(3,*)	(4,*)	(5,*)
(*,1)	3.3	SC	SC	2.0	SC
(*,2)	3.4	2.5	2.5	2.1	2.6
(*,3)	3.3	2.7	1.7	1.9	1.8
(*,4)	2.9	3.2	2.4	2.3	2.7
(*,5)	4.0	2.0	2.6	2.3	2.2

As a next step, we investigated the polarization of the 0th order mode. For this, we

measured P_t – the optical power that was transmitted through a linear polarizer – at different polarizer angles ϕ. We did this at low pump currents (for most VCSELs $I \approx 1.7 \cdot I_{th}$) to avoid the influence of higher-order modes. In Fig. 3.4, these measurements are shown for four different VCSELs with normalized transmitted optical power. For more details about the measurements, including the calibration, see Subsec. 2.4.1. We fit the results with the function

$$\frac{P_t(\phi)}{P_{max}} = \frac{P_{off}}{P_{max}} + \left(1 - \frac{P_{off}}{P_{max}}\right) \cos^2(\phi - \phi_{off}), \tag{3.1}$$

where P_t is divided by the maximal transmitted optical power P_{max} for normalization, P_{off} is an offset on the vertical plot axis, and ϕ_{off} is the angular offset. For all VCSELs, ϕ_{off} is listed in Tab. 3.4. For 23 VCSELs, we obtain $|\phi_{off}| < 7°$. Since we rotated the polarizer by hand, there is an uncertainty of at least 2°. VCSELs (1,5) and (4,5) exhibit a significantly larger angular offset than the rest. Summarizing the results from Tab. 3.4, we obtain an average

$$\overline{\phi}_{off} = 1.8° \pm 4.4°. \tag{3.2}$$

We obtain similar results for P_{off}. For 22 VCSELs, $P_{off} < 0.04$, for VCSEL (2,4), $P_{off} = 0.06$, and for VCSELs (1,5) and (4,5), $P_{off} = 0.09$. This shows that the emission of VCSELs (1,5) and (4,5) is not completely linearly polarized. Summarizing, our results hint linearly polarized 0th order mode emission with a main polarization direction parallel to the rows of the array (x-axis, s. Figs. 2.1 and 2.7) for most of the VCSELs. As described in Sec. 2.1, the VCSEL apertures are about 3 % elliptical with the major axis being the x-axis, which is thus parallel to the main polarization direction of the emission of most of the VCSELs. We deduce that this small ellipticity contributes to the homogeneity in polarization, especially because arrays that had been manufactured following a similar process but in which the VCSELs had a circular aperture were not as homogeneous regarding their emission's polarization (data not shown). Note that birefringence and gain differences between different polarizations have been predicted numerically in VCSELs with small elliptical apertures [83].

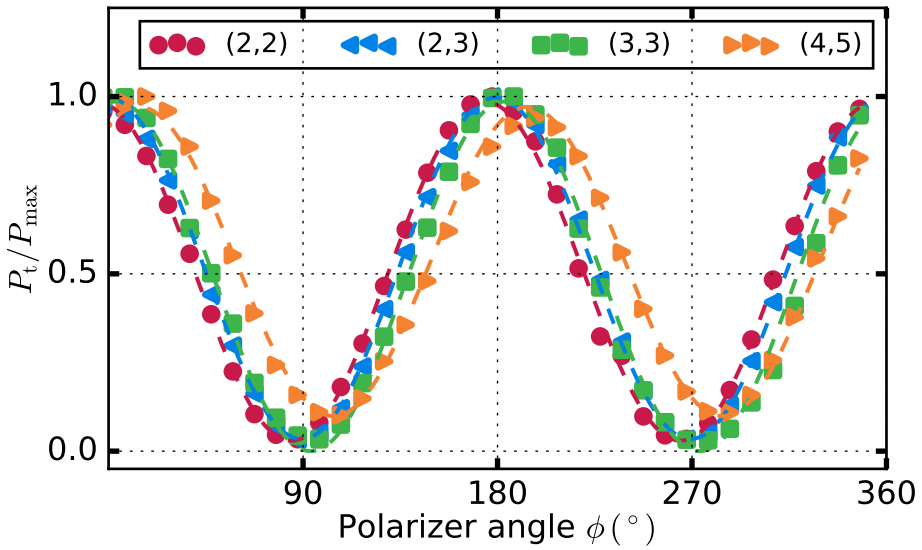

FIGURE 3.4: Normalized optical power transmitted through a linear polarizer vs. polarizer angle for four different VCSELs at $I \approx 1.7 I_{th}$. Dashed lines: Sinusoidal fits.

To conclude the analysis of the transverse VCSEL modes, we imaged the VCSEL near

TABLE 3.4: Main polarization direction of VCSEL emission at low pump currents, extracted from fits to the optical power transmitted through a linear polarizer at different angles (s. Fig. 3.4).

ϕ_{off} (°)	(1,*)	(2,*)	(3,*)	(4,*)	(5,*)
(*,1)	-0.7	-1.3	-0.6	3.4	1.0
(*,2)	-1.6	-5.4	0.7	3.0	-1.0
(*,3)	3.5	-0.7	3.5	2.3	6.6
(*,4)	0.7	0.2	-2.6	-3.7	2.4
(*,5)	14.2	2.4	2.8	14.0	1.4

fields on a CCD camera, as shown in Fig. 3.5. For this, we used the microscope objective (MO) for imaging, a beam displacement prism for resolving by polarization, and a diffraction grating for separating different modes. The beam displacement prism causes the VCSEL emission with a polarization along the x-axis to appear at the bottom of the images, and the emission polarized along the y-axis at the top. The lower the wavelength of a certain VCSEL mode is, the further it appears to the right of the image. We observe that, for all VCSELs, the first mode that appears at low pump currents is the 0th order LP_{01} mode (as defined in Ref. [8, pp. 92 ff.]), which is circularly symmetric and single-lobed. The images confirm what Fig. 3.4 suggests: in 23 VCSELs, the LP_{01} mode is linearly polarized in x-direction. As in the optical spectra (Fig. 3.3), higher modes appear at higher pump currents. The first modes to appear are in most cases the two-lobed LP_{11} modes [8, pp. 92 ff.]. For many VCSELs, (e.g. VCSEL (2,5)), we observe one LP_{11} mode for each polarization with a mode profile orthogonal to each other. From the optical spectra (Fig. 3.3), we know that these modes are usually not degenerate. Often the lobes are parallel to the x- and y-axes. Still, we also observe mode profiles that are not aligned to the array axes and/or not orthogonal for modes of different polarizations, as e.g. for VCSEL (1,4) (Fig. 3.5a). Interestingly, when increasing the pump current of VCSEL (2,4), the x-polarized LP_{11} mode disappears in favor of the y-polarized one (Fig. 3.5b). This corresponds to the shift in wavelength of the second peak in Fig. 3.3 c). For some VCSELs, we observe 1st order modes that cannot readily be classified as LP modes or a superposition thereof. One example for this is VCSEL (3,2) (Fig. 3.5d), for which we observe an annular emission profile with small inhomogeneities in the intensity. For a few VCSELs, the 2nd order modes are visible, too. In Fig. 3.5c, we find profiles that resemble two LP_{21} modes that are rotated by 45° with respect to each other. In total, we observe a variety of modal behaviours. Still, all VCSELs have in common that the first mode to appear is the 0th order LP_{01} mode, which for nearly all VCSELs is linearly polarized along the x-axis.

One important parameter for coupling experiments that we can extract from the beam profiles is the diameter of the LP_{01} mode. For this, we first identify the maximally saturated pixel of the image recorded at $I \approx 2 \cdot I_{th}$, and verify that it is close to the center of the 0th order mode. Then, we fit a Gaussian function to the values in the same row as that pixel, which results in a cut through the 0th order mode along the x-axis. The fit function is

$$I(x) = a \cdot \exp\left(\frac{-2(x - x_0)^2}{w_x^2}\right), \tag{3.3}$$

where I is the intensity recorded by the camera, a is a multiplier, x_0 is the x-coordinate of the peak (not necessarily an integer), and w_x is the beam size in pixels in x-direction. We repeated the same procedure along the y-axis. This equation equals the squared absolute value of the field equation of a Gaussian beam given in Ref. [3, p. 654]. The full width at

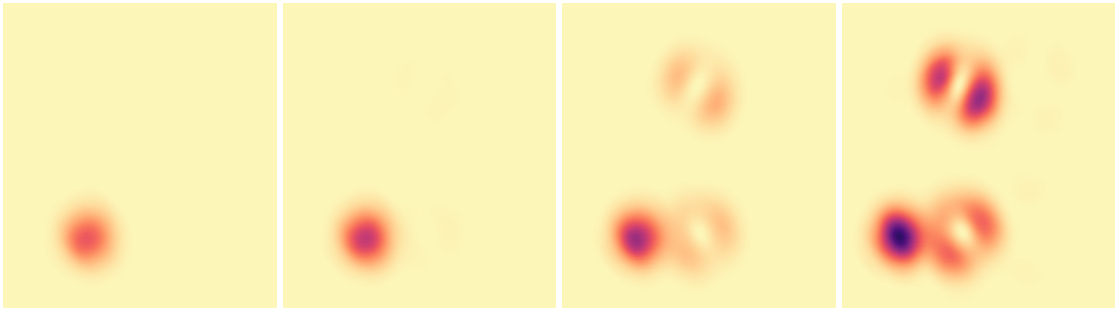

(a) Image of the near-field emission of VCSEL (1,4) at (from left to right) $I \approx 1.9 \cdot I_{\text{th}}$, $I \approx 2.2 \cdot I_{\text{th}}$, $I \approx 3.1 \cdot I_{\text{th}}$, and $I \approx 5.6 \cdot I_{\text{th}}$.

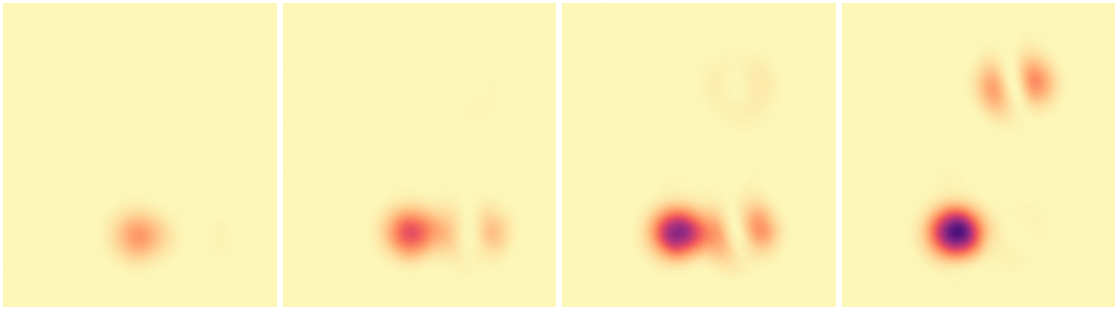

(b) Image of the near-field emission of VCSEL (2,4) at (from left to right) $I \approx 1.7 \cdot I_{\text{th}}$, $I \approx 2.8 \cdot I_{\text{th}}$, $I \approx 4.2 \cdot I_{\text{th}}$, and $I \approx 4.4 \cdot I_{\text{th}}$.

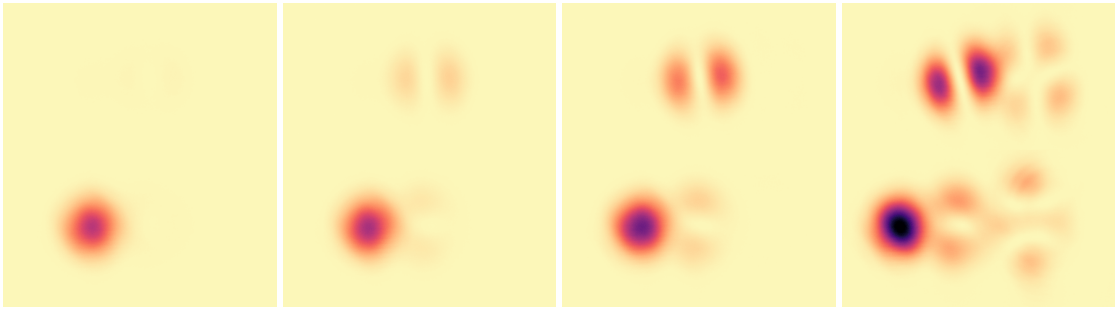

(c) Image of the near-field emission of VCSEL (2,5) at (from left to right) $I \approx 1.7 \cdot I_{\text{th}}$, $I \approx 1.9 \cdot I_{\text{th}}$, $I \approx 2.8 \cdot I_{\text{th}}$, and $I \approx 5.0 \cdot I_{\text{th}}$.

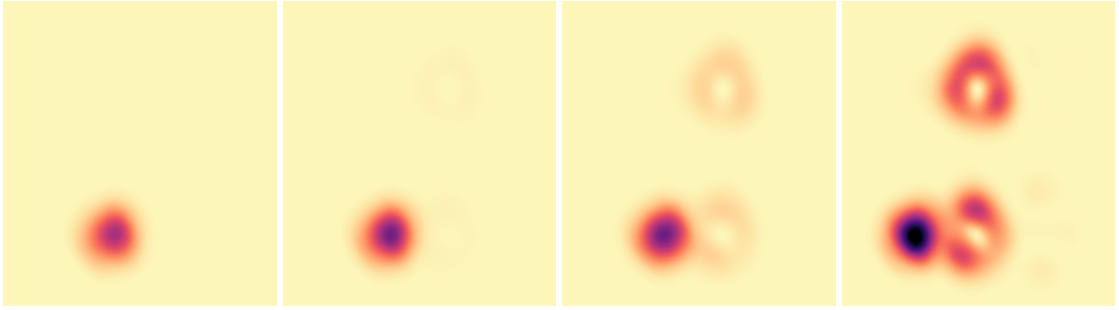

(d) Image of the near-field emission of VCSEL (3,2) at (from left to right) $I \approx 2.1 \cdot I_{\text{th}}$, $I \approx 2.4 \cdot I_{\text{th}}$, $I \approx 3.0 \cdot I_{\text{th}}$, and $I \approx 6.0 \cdot I_{\text{th}}$.

FIGURE 3.5: Image of the near-field emission of four different VCSELs at different pump currents, using a beam displacement prism for resolving by polarization and a diffraction grating for separating different modes.

half maximum along the x-axis can then be calculated as

$$\mathrm{FWHM}_x = \frac{\sqrt{2\ln(2)}\, w_x s}{M}, \tag{3.4}$$

where $s = 6.45 \frac{\mu\mathrm{m}}{\mathrm{pixel}}$ is the pixel size and $M = 1150\,\mathrm{mm}/9\,\mathrm{mm} = 128$ is the magnification. We obtain an average $\overline{\mathrm{FWHM}_x} = 4.7\,\mu\mathrm{m}$. Analogically, along the y-axis we obtain $\overline{\mathrm{FWHM}_y} = 4.5\,\mu\mathrm{m}$. Both values are roughly equal to the target oxide aperture of 4.5 µm. $\overline{\mathrm{FWHM}_x} > \overline{\mathrm{FWHM}_y}$ is plausible, since the VCSEL apertures are elliptical with the major axis along the x-axis. In Tab. 3.5, $\beta := \mathrm{FWHM}_x/\mathrm{FWHM}_y$ is listed for all the VCSELs. For 13 VCSELs, $\beta > 1.02$, for 6 VCSELs, $\beta = 1.00 \pm 0.02$, while for 6 VCSELs, $\beta < 0.98$. Although, due to the high Al content of the oxidation layer (98 %) in our arrays, the oxidation rates might be slightly anisotropic, this anisotropy should depend on the crystallographic directions and thus be homogeneous across the array [84]. Consequently, we exclude deviating aperture shapes as a cause for $\beta < 1.0$. The different orientations of the p-contacts, however, could play a role for this. As described in Sec. 2.1 (Fig. 2.1), the p-contacts have the shape of a ¾-ring with openings in different directions. For those VCSELs where the opening of this ¾-ring is in x-direction, we obtain an average $\overline{\beta} = 1.14$. All the VCSELs with $\beta > 1.20$ belong to this group. For the VCSELs, where this opening is in y-direction, $\overline{\beta} = 1.00$ and all the VCSELs with $\beta < 1.00$ belong to this group. In summary, the ellipticity of the 0th order mode is distorted in the axis of the opening of the annular p-contact. This is surprising, because we could explain the opposite behaviour by reduced gain due to reduced current injection in direction of the opening. We can exclude confinement effects by the contacts as a factor, since their inner diameter is 10 µm and thus more than twice larger than the mode's FWHM. However, inhomogeneities in the mechanical strain could play a role, since Debernardi et. al. [85] suggested that the elasto-optic effect can cause stronger birefringence than the electro-optic effect.

TABLE 3.5: Ratio of FWHMs of the 0th order mode's intensity in the images in x- and y-direction for the VCSELs of sample 5 at $I \approx 2 \cdot I_{\mathrm{th}}$.

$\beta := \mathrm{FWHM}_x/\mathrm{FWHM}_y$	(1,*)	(2,*)	(3,*)	(4,*)	(5,*)
(*,1)	1.01	1.00	0.96	1.05	0.91
(*,2)	1.00	1.14	1.05	0.98	0.96
(*,3)	1.29	0.95	1.13	0.94	1.01
(*,4)	1.11	0.91	1.24	1.27	1.01
(*,5)	1.09	1.05	1.10	1.08	1.04

3.3 Self-feedback

Since the mechanism with which we aim to couple the VCSELs is based on FB, it is useful to first analyze the VCSELs' behaviour under self-FB. The results in this section were obtained with VCSELs on two different arrays of chip 2: VCSEL (3,3) of array 1 and VCSEL (3,3) of array 5, in the following for brevity referred to as C1 and C5, respectively. Note that most of the experiments described in later chapters were carried out with array 5.

3.3.1 Changes to the P-I characteristics

In Fig. 3.6, P-I characteristics of VCSEL C1 at different FB attenuations ξ are shown. The measurements were taken with microscope objective, lens, 50/50 beam splitter and mirror, and thus in a 4f-setup. These elements attenuate the FB by $\xi \approx -7.0\,\mathrm{dB}$. By introducing neutral density filters (NDFs) into the external cavity, we attenuated the FB further, down to a minimum of -35.9 dB. The values for ξ are extracted from the datasheets of the NDFs at $\lambda = 976\,\mathrm{nm}$ for a double pass. As for the data shown in Fig. 3.2, we linearly fit the first points after crossing the threshold to obtain the threshold current I_{th} and the slope efficiency η. They are listed in the upper half of Tab. 3.6 ('no DOE'), together with the threshold reduction

$$\Psi(\xi) = \frac{I_{\mathrm{th}}(\xi) - I_{\mathrm{th}}(\text{no FB})}{I_{\mathrm{th}}(\text{no FB})}. \tag{3.5}$$

We observe that – without the diffractive optical element (DOE) in the external cavity – η decreases slightly with increasing FB strength, except for the case without NDFs ($\xi = -7.0\,\mathrm{dB}$). It varies by about 4 % in total. The threshold current clearly decreases with increasing FB strength. For comparison, we introduced the DOE into the external cavity. In this case, we observe the opposite for η, i.e. an increase with increasing FB strength. A double-pass through the DOE spreads the FB with the 0th order containing about 11 % of the power, which corresponds to an FB attenuation of -9.5 dB. However, comparing the values for Ψ with DOE to the ones without DOE suggests that only about 2 % of the optical power gets back to the central VCSEL as FB. This might be due to suboptimal alignment.

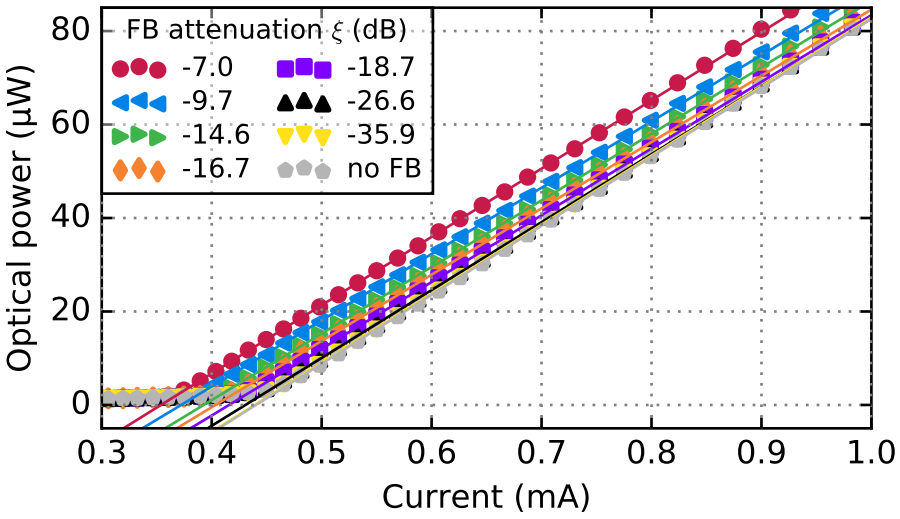

FIGURE 3.6: P-I characteristics of VCSEL (3,3) of array 1 (C1) at different FB attenuations ξ.

For VCSEL C5, we find that, without the DOE, the threshold is reduced by 3.5 % with unattenuated FB compared to the case without FB. This is considerably lower than for VCSEL C1. The slope efficiency decreases by an insignificant 1 % with FB. The large difference in threshold reduction between VCSELs C1 and C5 might be due to the modal structure of VCSEL C1, in which the 1st order mode appears at much lower pump currents than for other VCSELs of our arrays (see Subsec. 3.3.3).

TABLE 3.6: Thresholds I_{th}, their reduction Ψ and slope efficiency η of VCSEL C1 at different FB attenuations ξ.

	ξ (dB)	-7.0	-9.7	-14.6	-16.7	-18.7	-26.6	-35.9	no FB
no DOE	I_{th} (mA)	0.354	0.372	0.393	0.403	0.416	0.431	0.439	0.440
	$\eta\left(\frac{\mu W}{\mu A}\right)$	0.146	0.142	0.142	0.142	0.143	0.145	0.148	0.148
	-Ψ (%)	19.5	15.5	10.7	8.4	5.5	2.0	0.2	0.0
with DOE	I_{th} (mA)	0.419	0.427	0.429	0.432	0.432	0.432	0.432	0.432
	$\eta\left(\frac{\mu W}{\mu A}\right)$	0.155	0.152	0.151	0.151	0.150	0.148	0.148	0.148
	-Ψ (%)	3.0	1.2	0.7	0.0	0.0	0.0	0.0	0.0

3.3.2 External cavity modes

In Fig. 3.7, radio-frequency (RF) spectra of VCSELs C1 and C5 at different FB attenuations ξ are shown together with spectra recorded with blocked FB ('no FB'). The plots at the top show the spectra of VCSEL C1, on the left with the DOE placed in the external cavity and on the right without it, both at $I = 1.5\,\text{mA} = 3.4 \cdot I_{th}(\text{no FB})$. The plots at the bottom show the spectra of VCSEL C5, on the left with the DOE placed in the external cavity and at $I = 0.4\,\text{mA} = 1.3 \cdot I_{th}(\text{no FB})$, and on the right without DOE in the external cavity and at $I = 1.5\,\text{mA} = 5 \cdot I_{th}(\text{no FB})$. In all four cases, we observe peaks at multiples of the external cavity frequency f_{ext} at low ξ, although in Fig. 3.7 c) they are significantly weaker. We identify these peaks as the external cavity modes. The broadest peaks appear for medium FB for VCSEL C1 without DOE in the external cavity. At higher FB strengths, the peaks become narrower and higher. Especially at $\xi = -9.7\,\text{dB}$, distinctive double peaks are visible. From the data in Fig. 3.7 a) and b) we derive that inserting the DOE into the external cavity affects the width and height of the peaks comparably to attenuating the FB by about -12 dB. Additionally, the peaks are shifted to slightly lower frequencies. In the case of double peaks, we calculated f_{ext} from the lower-frequency one. With this, we obtain as a difference between both measurements $f_{ext}(\text{no DOE}) - f_{ext}(\text{DOE}) = 6\,\text{MHz}$. This corresponds to about 5 mm in external cavity length (or 10 mm considering that the light has to pass it twice), which is about thrice what we would expect due to the longer optical path through the DOE. For VCSEL C5, we observe significantly narrower and lower peaks at multiples of f_{ext}. This resembles the P-I behaviour, where the threshold reduction was considerably lower for C5 than for C1. For VCSEL C1 in both cases and for VCSEL C5 without the DOE, we also observed peaks at multiples of 70 MHz when the external cavity was blocked. We could not identify the cause for this. Still, we can exclude reflections at optical elements like the beam splitter or the microscope objective, since these would lead to peaks at higher frequencies.

3.3.3 Redshift

In Fig. 3.8, optical spectra of VCSELs C1 and C5 at different FB attenuations ξ are shown together with spectra recorded with blocked FB ('no FB'). Fig. 3.8 a), b), and d) were recorded simultaneously with Fig. 3.7 a), b), and d), respectively, while Fig. 3.8 c) does not correspond to Fig. 3.7 c). For VCSEL C1, at $I = 1.5\,\text{mA} = 3.4 \cdot I_{th}(\text{no FB})$ and without FB, the highest peak does not belong to a 0th but a 1st order mode. This differs significantly from the results presented for other VCSELs in Sec. 3.2. However, the most relevant features found in these measurements are the redshift and the increasing peak height of the 0th order mode with increasing FB. Especially the redshift is interesting,

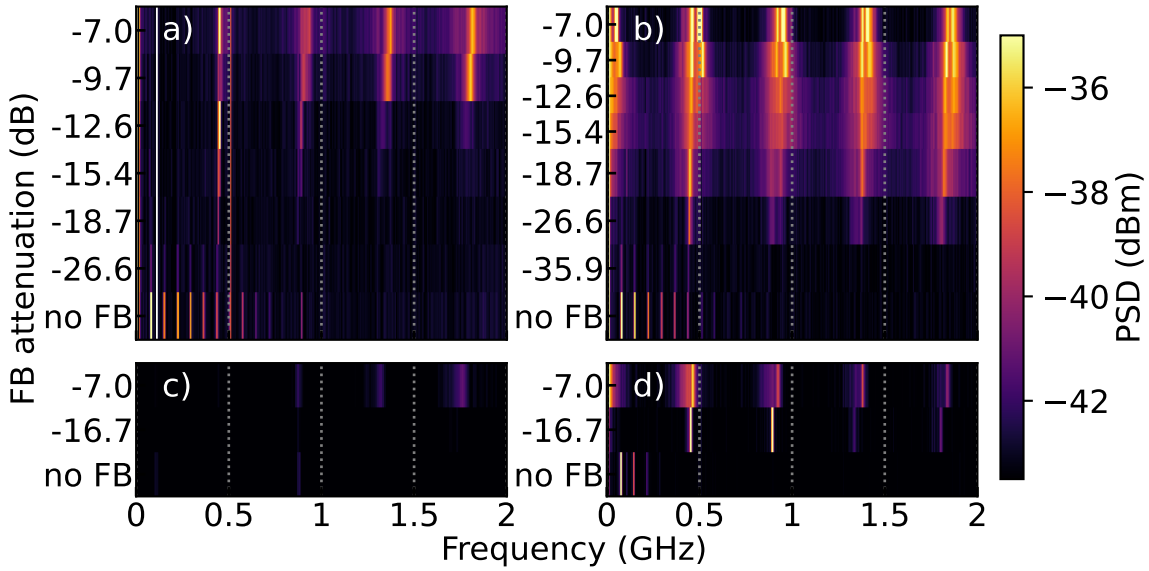

FIGURE 3.7: RF spectra of VCSELs C1 and C5 with different attenuations ξ of self-FB. Spectra with blocked FB ('no FB') shown for comparison. a) VCSEL C1 at $I = 1.5\,\mathrm{mA}$, DOE in the external cavity; b) VCSEL C1 at $I = 1.5\,\mathrm{mA}$, no DOE in the external cavity; c) VCSEL C5 at $I = 0.4\,\mathrm{mA}$, DOE in the external cavity; d) VCSEL C5 at $I = 1.5\,\mathrm{mA}$, no DOE in the external cavity.

since it can provide an estimation for the FB strength κ. From Ref. [86], we know that

$$\kappa = \frac{2\pi}{\alpha}\Delta f_{\mathrm{FB}}, \tag{3.6}$$

where α is the linewidth enhancement factor and Δf_{FB} is the redshift with FB. From fits to the data, we obtain $\kappa\alpha = 178\,\mathrm{ns}^{-1}$ for VCSEL C1 without DOE and $\kappa\alpha = 16.8\,\mathrm{ns}^{-1}$ for VCSEL C1 with DOE, which gives an estimation of -10.3 dB for the optical power in the 0th order after a double-pass through the DOE. For VCSEL C5 without DOE, we obtain $\kappa\alpha = 123\,\mathrm{ns}^{-1}$, and with DOE we obtain $\kappa\alpha = 19.4\,\mathrm{ns}^{-1}$, which gives an estimated reduction of -8.1 dB in FB strength due to the DOE. The difference in the results could be caused by a combination of slightly different α factors and alignment. Assuming that $2 < \alpha < 5$, we calculate an FB strength $36\,\mathrm{ns}^{-1} < \kappa < 62\,\mathrm{ns}^{-1}$.

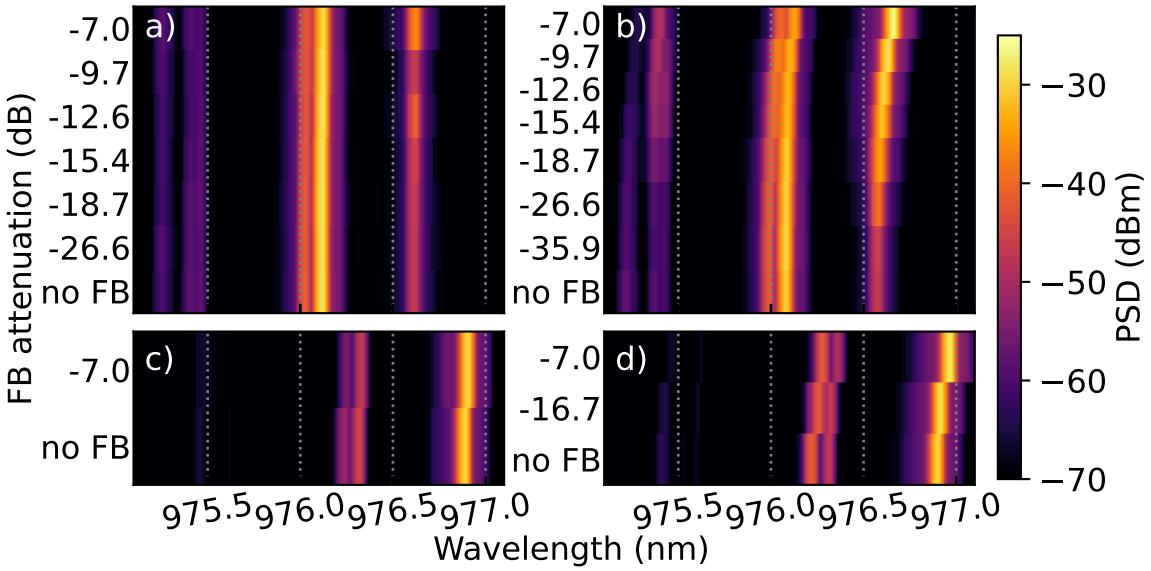

FIGURE 3.8: Optical spectra of VCSELs C1 and C5 at $I = 1.5\,\mathrm{mA}$ with different attenuations ξ of self-FB. Spectra with blocked FB ('no FB') shown for comparison. a) VCSEL C1, DOE in the external cavity; b) VCSEL C1, no DOE in the external cavity; c) VCSEL C5, DOE in the external cavity; d) VCSEL C5, no DOE in the external cavity.

3.4 Summary and conclusion

In this chapter, we have characterized the solitary VCSELs of array 5. We find that, across the array, most VCSELs behave homogeneously regarding their current-voltage (I-U) and optical power-current (P-I) characteristics. We find an average threshold current $\overline{I_{\mathrm{th}}} = (0.364 \pm 0.120)\,\mathrm{mA}$ and an average slope efficiency $\overline{\eta} = (0.244 \pm 0.036)\,\frac{\mu\mathrm{W}}{\mu\mathrm{A}}$. All of the three VCSELs that exhibited deviating I-U behavior were among the four VCSELs with deviating P-I characteristics. Analyzing the modal behaviour, we find that, for all VCSELs, the first mode that appears after crossing the threshold is the 0th order LP_{01} single-lobed mode with circular symmetry. It has an FWHM of about 4.5 µm and is for most VCSELs linearly polarized along the x-axis, which coincides with the dimension and ellipticity of the oxide aperture. All VCSELs emit single-mode (side-mode suppression ratio > 15 dB) below $I = 2 \cdot I_{\mathrm{th}}$, some do so up to higher pump currents. We characterized the behaviour of two VCSELs under self-FB: VCSEL (3,3) of array 1 and of array 5. We find that self-FB can reduce the threshold current by up to 20 %, but that this is strongly dependent on the VCSEL. We observe external cavity modes, whose intensity depends highly on the FB strength and the VCSEL. Analyzing the optical spectra, we calculate the FB strength for the external cavity without DOE as $36\mathrm{ns}^{-1} < \kappa < 62\mathrm{ns}^{-1}$.

Chapter 4

Diffractively coupled VCSEL networks

With the individual VCSELs fully characterized, we focus on another essential part of this thesis: establishing diffractive coupling experimentally. Crucially, using the DOE allows for coupling between nearest and second-nearest neighbours as well as simultaneous injection of an external laser into all the VCSELs of the array. We give proof for establishing diffractive coupling between the VCSELs as well as for simultaneous optical injection locking of nearly all the VCSELs in the array. Furthermore, we analyze how the VCSELs respond to intensity modulation of the optical injection. Note that all results in this chapter were obtained with the DOE placed in the external cavity, as opposed to most of the results in the previous chapter. The most significant results that are presented in this chapter have been published in Ref. [87].

4.1 Experimental alignment

Accurately aligning all the experimental parameters to achieve coupling between the array's VCSELs is challenging. How most of those parameters are adjusted in practice has been described in Sec. 2.3. Often, there is a straight-forward way for alignment by maximizing a correlated value that can readily be measured. However, this is less clear for the alignment procedure for adjusting DOE angle ν, which describes the DOE rotation in the plane orthogonal to the optical axis of the experiment. Yet it is a parameter of crucial importance for coupling, as illustrated in Fig. 4.1.

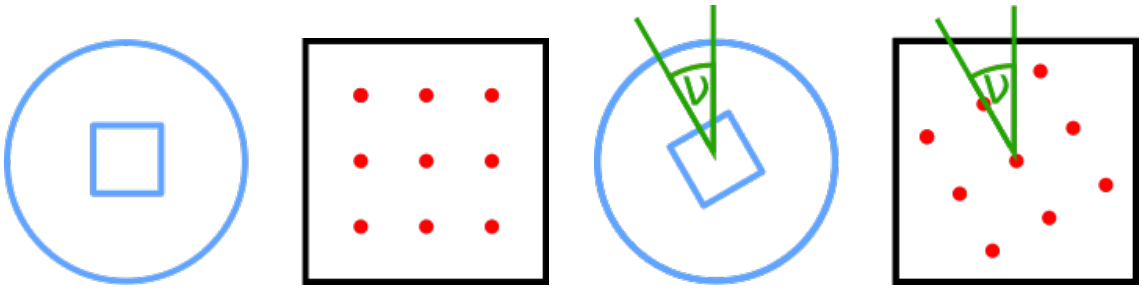

(a) Left: DOE. Right: Pattern generated by beam multiplexing at the DOE.

(b) Left: DOE rotated by ν compared to (a). Right: Resulting pattern also rotated by ν.

FIGURE 4.1: Illustration of the effects of DOE angle ν. When rotating the DOE in the plane orthogonal to the optical axis, the generated beam pattern is rotated by the same angle.

To explain the procedure with which we optimized ν, we consider the situation where the positions of array and reference fiber are aligned for maximal fiber-coupling of the light emitted by the central VCSEL (see Sec. 2.3 and Fig. 2.7). Now, only one non-central VCSEL, e.g. VCSEL (2,3), is pumped, the DOE is installed, and the external cavity is not blocked. In this configuration, the emission of VCSEL (2,3) is multiplexed by the DOE. After a roundtrip in the external cavity, a part of the corresponding diffractive order is reflected at the surface of the central VCSEL. For the correct rotation angle, the reflection is

coupled into the reference fiber. Maximizing the optical power coupled into the reference fiber P_{ref} in above-described configuration optimizes the mode overlap between VCSELs (2,3) and (3,3). Simultaneously, this also aligns the overlap between any other non-central VCSEL and VCSEL (3,3). To finally optimize the DOE angle ν, we first determine a set of pump currents at which all the non-central VCSELs of the array emit the same optical power P_0. Then, at these pump currents and with $I(3,3) = 0$, we adjust ν to maximize P_{ref}.

To double-check that this alignment method results in coupling, we installed a beam sampler and a lens imaging on a CMOS camera in the injection arm. This captures the multiplexed emission of the VCSEL array after reflection at the mirror and double-pass through the DOE, which is essentially a copy of the back-reflected intensities at the VCSEL array surface. We compared two images, one with $I(3,3) = 0.5\,\mathrm{mA}$ and all the other VCSELs switched off, and another one with all VCSELs adjusted to emit the same power. We observed that the multiplexed emission of all the VCSELs overlapped for the adjusted angles (see Fig. 4.2). This demonstrates that the alignment indeed favors coupling. We did not rely only on the camera for this alignment step because it is not as sensitive to fine-tuning as P_{ref} is.

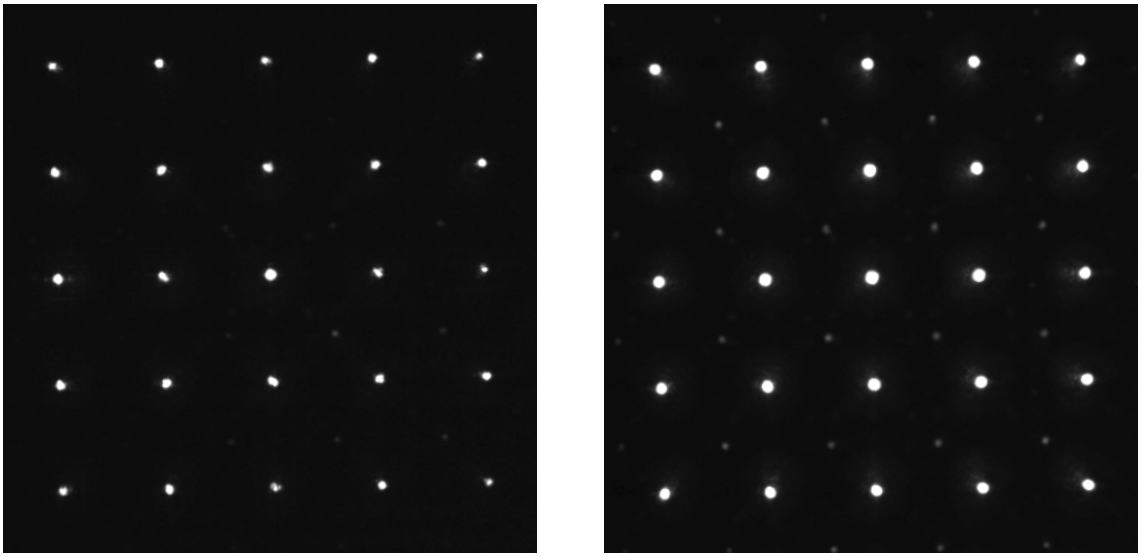

FIGURE 4.2: Overlap of multiplexed emission of different VCSELs. Left: Image of the emission of the central VCSEL after double-pass through the DOE. Right: Image of the emission of all array VCSELs after double-pass through the DOE.

One weakness of this method is that it might lead to overalignment to a small group of VCSELs due to asymmetries, as explained in the following. For perfect alignment, we would expect the contributions to P_{ref} to be proportional to the values given for a double pass through the DOE in Fig. 2.4. But even after accounting for the theoretical variations in coupling strength, there are differences of up to one order of magnitude between the reference fiber coupling efficiencies of different VCSELs, which we were not able to eliminate. This shows how alignment-sensitive the setup is. Still, in a given situation in which only ν has to be aligned, the procedure is helpful. Optimized coupling is found for all VCSELs at similar values of ν, as shown in Fig. 4.3. The plotted values are normalized according to the following approximation. For every VCSEL (c,r), including VCSEL (3,3), we measured its free-space optical power $P_{\mathrm{free}}(c,r)$ after passing microscope objective (MO) and 50/50 beam splitter (BS1). We also measured the reference fiber-coupled intensity $P_{\mathrm{ref}}(3,3)$ of VCSEL (3,3). With this, we approximate the theoretically

expected maximum of $P_{\mathrm{ref}}(c,r)$ as

$$P_{\mathrm{exp}}(c,r) = P_{\mathrm{free}}(c,r)T_{\mathrm{MO}}^2 T_{\mathrm{BS1}} R_{\mathrm{BS1}} C_{\mathrm{DOE}}(c,r) P_{\mathrm{ref}}(3,3)/P_{\mathrm{free}}(3,3), \tag{4.1}$$

where T_{MO}, T_{BS1}, and R_{BS1} are the transmission and reflection coefficients of microscope objective and 50/50 beam splitter, $C_{\mathrm{DOE}}(c,r)$ is the multiplexing matrix coefficient for a double-pass through the DOE, and the multiplication with the experimentally obtained quantity $P_{\mathrm{ref}}(3,3)/P_{\mathrm{free}}(3,3)$ accounts for the fiber-coupling efficiency and the pass through the 30/70 beam splitter (BS2). Here, we approximate the fiber-coupling efficiency $P_{\mathrm{ref}}(c,r)/P_{\mathrm{free}}(c,r)$ of every VCSEL with the experimentally measured one of VCSEL $(3,3)$, which we optimized directly. This explains why we can obtain $P_{\mathrm{ref}}(2,2)/P_{\mathrm{exp}}(2,2) > 1$ in Fig. 4.3 – the fiber-coupling efficiency of VCSEL $(2,2)$ is higher than that of VCSEL $(3,3)$.

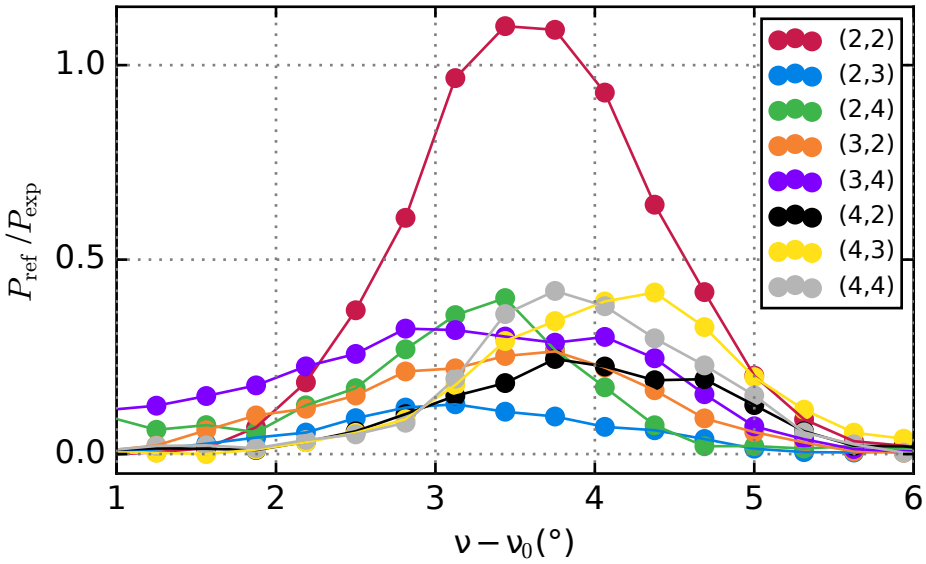

FIGURE 4.3: For all VCSELs in the 3×3-ring around the central VCSEL (3,3), the normalized reference fiber-coupled intensity $P_{\mathrm{ref}}/P_{\mathrm{exp}}$ is plotted against $\nu - \nu_0$, where ν_0 is an arbitrary angle (lines are guides to the eye). Even though the fiber-coupling efficiencies differ by up to nearly an order of magnitude between different VCSELs, their maxima lie within $\pm 1°$.

4.2 Pairwise coupling

For our VCSEL array, there are 231 possibilities for pairwise coupling configurations, thus investigating interactions for all of them would be a lengthy and unpractical task. For this reason, we limit our experiments to pairwise coupling of VCSEL (3,3) and one other VCSEL or a short-circuited VCSEL pair. In all these cases, we find signatures for optical coupling in the RF spectra. In the optical spectra, we observe optical locking in most cases, and we use the widths of the found locking regions to estimate the coupling strength. To investigate this pairwise coupling, we kept $I(3,3) = 0.5\,\mathrm{mA} = 1.7 I_{\mathrm{th}}(3,3)$ constant, while incrementing the pump current of another VCSEL (c,r) in the smallest steps that are possible with our control unit. All the other VCSELs were switched off. At every pump current $I(c,r)$, we recorded the optical and the radio-frequency (RF) spectrum of VCSEL $(3,3)$. We did not identify inadvertent lasing by VCSEL $(3,1)$, which is short-circuited with VCSEL $(3,3)$, to influence these measurements significantly. The

emission wavelengths of both VCSELs differ by more than 0.1 nm, making them distinguishable. Furthermore, the emission of VCSEL $(3,1)$ is not collected by the SM fiber that collects the emission of VCSEL $(3,3)$. The optical spectra for pairwise coupling of VCSEL (3,3) with four different individual VCSELs (c,r) are shown in Fig. 4.4. Similarly, in Fig. 4.7, the RF spectra for pairwise coupling of VCSEL (3,3) are shown, although not for the exact same set of VCSELs. All these spectra are presented as stacked color contour plots, with $I(c,r)$ given on the right y-axis in units of the threshold current of the respective VCSEL, $I_{\mathrm{th}}(c,r)$, and the difference of the emission wavelengths of the solitary VCSELs given on the left y-axis. Due to reflections (as described in Sec. 4.1), contributions from VCSEL (c,r) are visible in the spectra.

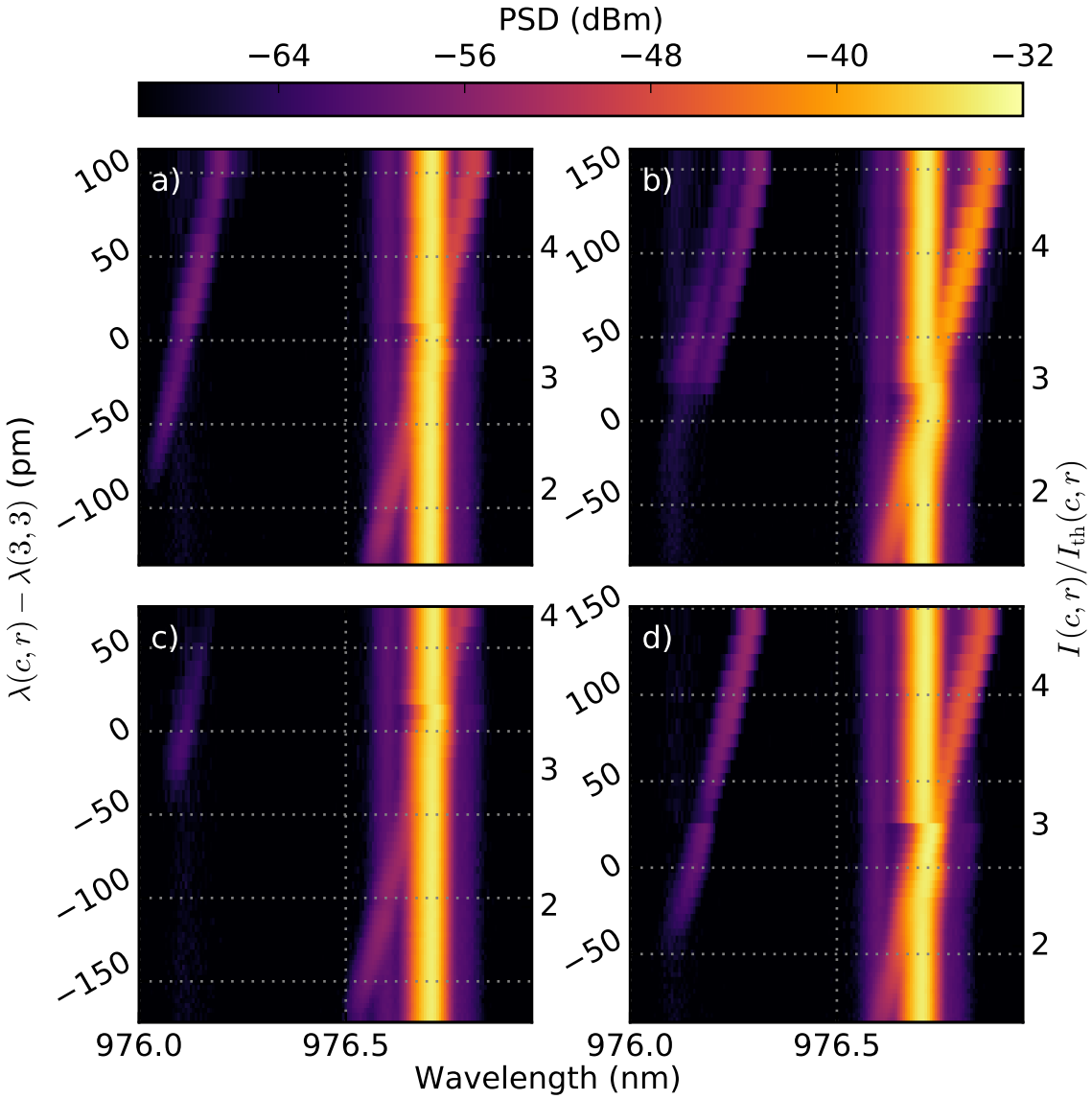

FIGURE 4.4: Stacked color-coded optical spectra of VCSEL (3,3) at $I(3,3) = 0.5\,\mathrm{mA}$ coupled to VCSEL (c,r). Contributions from VCSEL (c,r) are visible due to reflections. The right y-axis indicates the pump current $I(c,r)$ of VCSEL (c,r) in units of its threshold current, the left y-axis shows the resulting spectral mismatch between the solitary VCSELs' ground modes. a) (c,r) = (1,3), b) (c,r) = (3,2) (and due to a short-circuit (2,1)), c) (c,r) = (2,4), d) (c,r) = (3,4).

To analyze the optical spectra, we define the peak wavelength, which we determine

as described in Subsec. 2.4.2, as λ_{pair}. As before, $\lambda(c,r)$ and $\lambda(3,3)$ denote the wavelengths of the ground mode of the solitary VCSELs (c,r) and (3,3), respectively. In all the cases shown in Fig. 4.4, we find ranges of $I(c,r)$ for which $\lambda_{\text{pair}} > \lambda(3,3)$, and within these current ranges, the maximum of the measured spectrum is hence pulled towards the emission wavelength of the solitary VCSEL (c,r), i.e. $\lambda_{\text{pair}} \approx \lambda(c,r)$. Such spectral shifts are the classical signature of optical injection locking. For a quantitative analysis, in Fig. 4.5, we plot the position of λ_{pair} against the difference between $\lambda(c,r)$ and $\lambda(3,3)$. For calculating this difference, we also take into account measurements of the solitary VCSELs at similar pump currents. Besides, we linearly fit the points far from the optical locking region to account for a minimal drift of $\lambda(3,3)$ due to heating of the array when increasing the pump current of the other VCSEL. In most cases, we clearly observe $\lambda_{\text{pair}} > \lambda(3,3)$ for some region, but hardly $\lambda_{\text{pair}} < \lambda(3,3)$ within the resolution of our OSA. This is expected, and for unidirectionally coupled VCSELs, it has been observed before [18]. The two main reasons for this are that the locking region is asymmetric due to the α factor, as directly stated by Eq. 1.3, and, that to increase $\lambda(c,r)$, one has to increase $I(c,r)$, which in turn leads to an increase of $P(c,r)$. The higher the ratio $P(c,r)/P(3,3)$, the larger the detuning $|\lambda(3,3) - \lambda(c,r)|$ can be while still observing locking (s. Eq. 1.3), which further amplifies this asymmetry. Since the coupling is bidirectional, locking at $\lambda(3,3)$ is also possible, although when $\lambda(3,3) \approx \lambda(c,r)$ we have $P(c,r) > P(3,3)$ for all non-central VCSELs (c,r). (This is device-specific and is pure coincidence.) However, locking at $\lambda(3,3)$ would not be as easily observed in the spectra of VCSEL (3,3). We base our further analysis on $\Delta\lambda_{\text{pair}}(c,r) := \max|\lambda_{\text{pair}}(c,r) - \lambda(3,3)|$, the largest shift of the spectral maximum that we observe. The extracted $\Delta\lambda_{\text{pair}}(c,r)$ are summarized in Tab. 4.1.

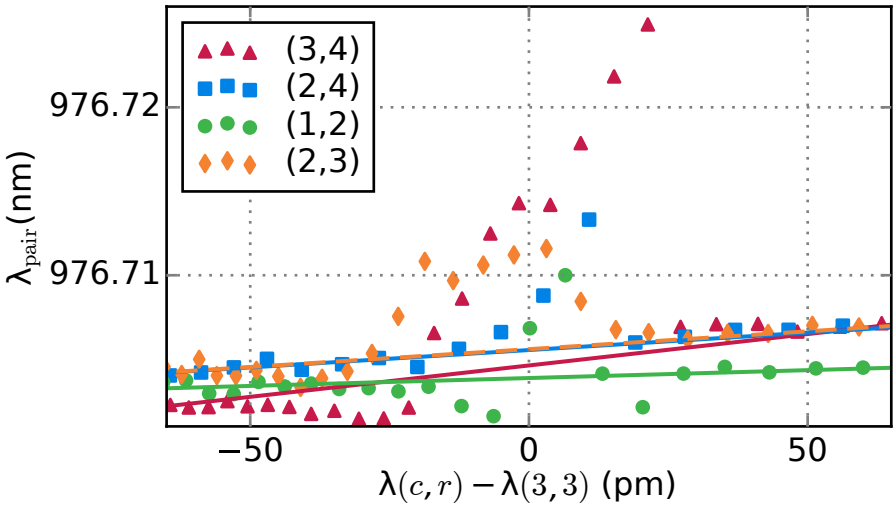

FIGURE 4.5: Peak positions λ_{pair} extracted from Fig. 4.4. Lines: linear fits to the points far from the optical locking region. $\Delta\lambda_{\text{pair}}$ is the maximal difference between the linear fit and λ_{pair}.

We found a maximal $\Delta\lambda_{\text{pair}}(c,r) = 18\,\text{pm}$ for $(c,r) = (3,4)$. In 14 of 21 cases, the signatures we found in the optical spectra were clear enough for us to classify the observed behaviour as optical injection locking of VCSEL (3,3) with the respective VCSEL or VCSEL pair. To check the compatibility of the experimental data with the theoretical predictions, we first approximate the optical power of VCSEL (c,r) at the top facet of VCSEL (3,3) by

$$P(c,r)|_{\text{tf(3,3)}} \approx T_{\text{MO}}^2 T_{\text{BS1}}^2 C_{\text{DOE}}(c,r) P(c,r), \tag{4.2}$$

TABLE 4.1: Largest shift of the spectral maximum $\Delta\lambda_{\text{pair}}(c,r) = \max(\lambda_{\text{pair}} - \lambda(3,3))$ for different VCSELs (c,r). SC: short-circuit with a more central VCSEL impedes separate measurement.

$\Delta\lambda_{\text{pair}}$ (pm)	(1,*)	(2,*)	(3,*)	(4,*)	(5,*)
(*,1)	3	SC	SC	3	SC
(*,2)	5	4	16	6	1
(*,3)	7	6	-	5	6
(*,4)	2	8	18	2	2
(*,5)	4	2	2	4	0

where $T_{\text{MO}} = 0.9$ and $T_{\text{BS1}} = 0.48$ are the transmission coefficients of microscope objective and 50/50 beam splitter, respectively, $C_{\text{DOE}}(c,r)$ is the multiplexing matrix coefficient for a double-pass through the DOE as given in Fig. 2.4, and $P(c,r)$ is the total optical power emitted by VCSEL (c,r). This approximation allows us to plot $\Delta\lambda_{\text{pair}}(c,r)$ (s. Tab. 4.1) against $\sqrt{P(c,r)/P(3,3)}\Big|_{\text{tf}(3,3)}$ in Fig. 4.6, neglecting the VCSELs for which we do not clearly observe optical locking, and fit the values linearly. The linear fit yields a slope $b = 32\,\text{pm}$. This is comparable to values obtained for identical VCSELs [9] and to VCSELs emitting at 1550 nm with optical injection via optical fibers [88]. Rearranging Eq. 1.3 and inserting the experimentally obtained quantities yields

$$\Delta\lambda_{\text{pair}}(c,r) = \frac{\lambda^2}{2\pi c} k_c \sqrt{1+\alpha^2} \sqrt{\frac{P(c,r)}{P(3,3)}}\Bigg|_{\text{tf}(3,3)} \tag{4.3}$$

where we have approximated $\Delta\omega = -2\pi c \Delta\lambda/\lambda^2$ and $|\lambda(3,3) - \lambda(c,r)| \ll \lambda$ with $\lambda = \lambda(3,3) \approx \lambda(c,r)$. Together with the linear fit we can hence approximate

$$k_c = \frac{2\pi b c}{\lambda^2\sqrt{1+\alpha^2}}. \tag{4.4}$$

Inserting realistic values of $2 < \alpha < 5$ [89–92], we obtain $13\,\text{ns}^{-1} < k_c < 29\,\text{ns}^{-1}$ as the average coupling efficiency throughout the array. The two outliers in Fig. 4.6 are VCSELs $(3,2)$ and $(3,4)$, direct neighbors of the central VCSEL. However, as we know from experimental trials (data not shown), completely misaligning and realigning the setup (as described in Subsec. 2.3.3) can change $\Delta\lambda_{\text{pair}}(c,r)$ such that the outliers would be different VCSELs. This simply reflects the sensitive alignment underlying this optical setup with multiple confocal configurations.

Before analyzing the RF spectra, note that Fig. 4.7 b) and d) contain those RF spectra that correspond to the optical spectra shown in Fig. 4.4 b) and d), respectively, and were recorded at the same time as the corresponding optical spectra. The RF spectra shown in Fig. 4.7 a) and c) were recorded for pairwise coupling of the central VCSEL to different VCSELs than the optical spectra in Fig. 4.4 a) and c). Fig. 4.7 e) and f) are identical and contain RF spectra of the solitary central VCSEL with blocked external cavity (BEC) and with feedback (FB), for comparison. In Fig. 4.7 a) - d), we observe high peaks for $f \leq 0.2\,\text{GHz}$ that are partly present in the background, i.e. they partly persist even when no photodiode is connected to the electrical spectrum analyzer (ESA). We found that the RF signature of delayed FB-induced dynamics at the external cavity's roundtrip frequency f_{ext} disappears with the DOE placed inside the external cavity (compare to Fig. 3.7 b) and d)). Since small peaks around $f = 2.6\,\text{GHz}$ and around $f = 3.1\,\text{GHz}$ appear with FB, we assume that one of those peaks corresponds to undamped relaxation oscillations of

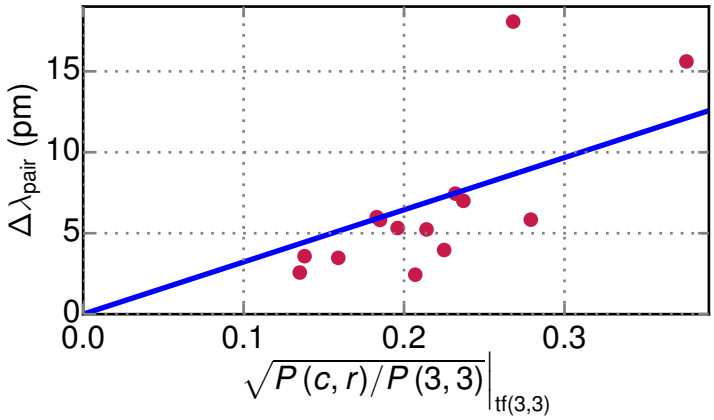

FIGURE 4.6: Maximal shift of spectral maximum vs. optical power ratio at the top facet of VCSEL (3,3) for different VCSELs (c,r).

VCSEL (3,3). Close to wavelength matching, we observe several changes in the RF spectra. Often, there is a region of $I(c,r)$, where peaks appear at frequencies $f > 3\,\mathrm{GHz}$, with a frequency spacing between consecutive peaks close to f_{ext}. Also, close to wavelength matching and below the upper boundary of the optical injection locking region, we often observe the suppression of otherwise present dynamics. This is most likely due to stable injection locking between VCSEL (3,3) and VCSEL (c,r). Importantly, we observe such signatures for the interaction of VCSEL (3,3) with all other VCSELs or short-circuited VCSEL pairs, even for coupling configurations for which we do not clearly observe optical locking in the optical spectra (as in Fig. 4.7 c)). This is experimental evidence for the successful diffractive coupling of every individual non-central VCSEL with the central VCSEL (3,3).

We saw in Tab. 4.1 and Fig. 4.6 that the width of the injection locking regions of different VCSELs to the central one does not fit the theoretical prediction. There are various possible explanations for this. To significantly reduce the coupling, mismatches have to be of the order of micrometers, since the FWHM of the VCSELs' dominant LP_{01} mode is about 4.5 µm (s. Sec. 3.2). Thus, we can exclude that inhomogeneities in the VCSELs' wavelengths play any major role for the mismatches, since we operate the VCSELs in a range of up to $\pm$ 0.5 nm, which could only cause mismatches of up to 0.05 µm (s. Eq. 2.5 for $f_{\mathrm{MO}} = 9.0\,\mathrm{mm}$, $\lambda = 976\,\mathrm{nm}$, and $a = 106\,\mu\mathrm{m}$). At wavelength matching conditions, the spectral deviations are much smaller. We can also exclude inhomogeneities from processing like lithography or oxidation as a possible factor, since they are expected to be smaller than 0.1 µm (personal communication by Tobias Heuser). Still, the pitch size of our VCSEL array might not be perfect, since the measurement uncertainty of the pitch size is 0.1 µm (personal communication by Tobias Heuser). This could lead to mismatches of up to 0.3 µm for diagonally second-nearest neighbouring VCSELs. As discussed in Sec. 2.2, with perfect alignment, deviations from the paraxial approximation cause mismatches that are smaller than 0.05 µm, even for diagonally second-nearest neighbouring VCSELs (see Fig. 2.5). However, imperfections in the alignment like minute tilts of MO, DOE, L1, BS1, or mirror could probably magnify these mismatches and could also give rise to the observed coupling inhomogeneities. Since the reflection angle of BS1 has been directly adjusted by hand and thus not with micrometer-precision, it is a possible reason for mismatches, which, however, we have not calculated in detail here. Finally, the main possibility for deviations stems from the DOE itself. The separation angle ϑ (not to be confused with angle ν as defined in Sec. 4.1) is provided with only two significant digits

resolution by the manufacturer, which leads to an uncertainty of up to 0.8 µm in terms of the ideal pitch size or 1.0 µm in terms of the DOE parameter a. Although we interpolated from values of ϑ given for a range of wavelengths for calculating the ideal array pitches, this could lead to significant mismatches. For directly neighbouring VCSELs, this deviation could reduce the overlap only slightly, but for diagonally second-nearest neigbouring VCSELs, it could lead to mismatches of up to 2.3 µm, meaning that the center of the incoming beam is focussed on the edge of the aperture of the receiving VCSEL. All of the above-mentioned effects can potentially accumulate in an imperfect alignment.

We can conclude that uncertainties in the pitch measurements potentially play a role, but the most important and major reason for mismatches is the uncertainty about the DOE's separation angle ϑ. However, these do not conclusively explain the observed coupling inhomogeneities. These inhomogeneities could be caused by deviations from the paraxial approximation due to imperfect alignment, especially of the angle of BS1.

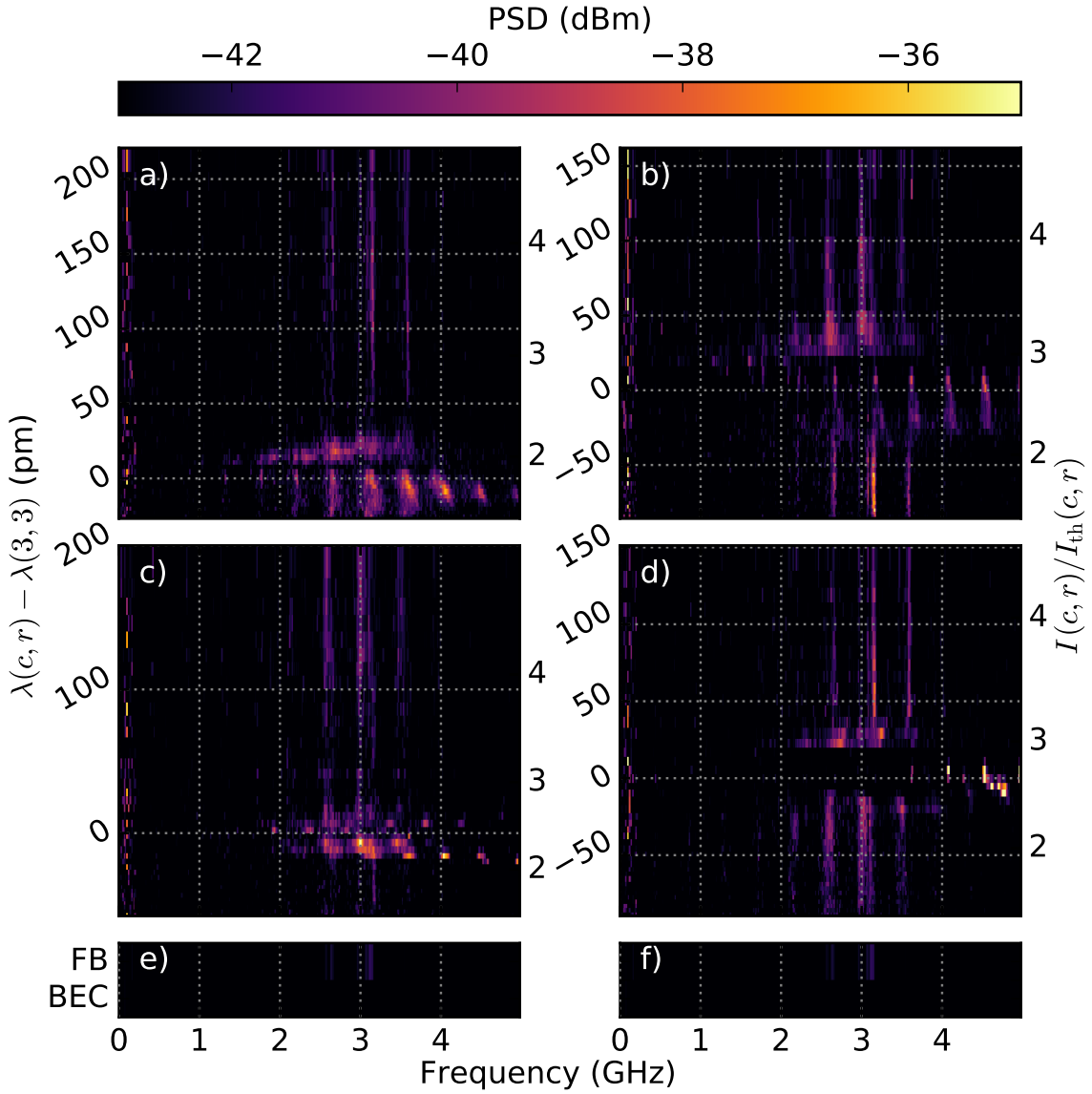

FIGURE 4.7: Stacked color-coded RF spectra of VCSEL (3,3) at $I(3,3) = 0.5\,\mathrm{mA}$ coupled to VCSEL (c,r). Left y-axis: Spectral mismatch between the solitary VCSELs' ground modes. Right y-axis: $I(c,r)$ in units of the threshold current. a) VCSEL (4,3), b) VCSEL (5,4), c) VCSEL (3,2) (and due to a short-circuit VCSEL (2,1)), d) VCSEL (3,4).

4.3 Coupling the entire array

While in the previous section we focussed on pairwise coupling, in this section we extend our study to coupling between all the VCSELs of the array, again centering our analysis around VCSEL (3,3). The most significant result that we find is a transition that occurs simultaneously in optical and RF spectra of the central VCSEL when increasing the detuning of the remaining VCSELs of the array. We interpret this as a transition from optical locking of the entire array to unlocking.

4.3.1 Characterization based on the central VCSEL

To investigate the interactions between the VCSELs in a structured way, we again fixed the pump current of the central VCSEL to constant $I(3,3) = 0.5\,\mathrm{mA}$, while we incremented the emission wavelength of all outer VCSELs simultaneously in steps of about 10 pm. The detuning we use here is

$$\Delta\lambda_{\mathrm{nc}} = \lambda_{\mathrm{nc}} - \lambda(3,3), \tag{4.5}$$

where λ_{nc} corresponds to the wavelength of highest PSD of all the remaining VCSELs combined. In Fig. 4.8, optical (left) and RF (right) spectra of VCSEL (3,3) for different $\Delta\lambda_{\mathrm{nc}}$ are shown. In Fig. 4.8 a), the green dashed line represents $\lambda(3,3)$. Even with blocked external cavity, $\lambda(3,3)$ is not constant due to heating of the array by increasing the pump current of the remaining VCSELs. The blue dotted line represents λ_{nc} as extracted from measurements in which the central VCSEL was switched off. Fig. 4.8 c) shows the RF spectra of the solitary VCSEL (3,3) with FB and blocked external cavity (BEC) for comparison. As before, the spectra in Fig. 4.8 a) and b) contain small contributions from the remaining VCSELs due to reflections (as described in Subsec. 4.1).

We clearly observe that VCSEL (3,3) emits close to λ_{nc} in the range of $-23\,\mathrm{pm} < \Delta\lambda_{\mathrm{nc}} < 55\,\mathrm{pm}$. At $\Delta\lambda_{\mathrm{nc}} = 55\,\mathrm{pm}$, we observe the reappearance of a small shoulder at $\lambda(3,3)$, and at $\Delta\lambda_{\mathrm{nc}} = 65\,\mathrm{pm}$ it becomes a distinctive peak. In the corresponding RF spectra, we observe an increased PSD at frequencies $f \leq 3\,\mathrm{GHz}$ for $\Delta\lambda_{\mathrm{nc}} \geq 55\,\mathrm{pm}$. Due to technical limitations of the VCSEL control unit, higher values of $\Delta\lambda_{\mathrm{nc}}$ are not accessible for pumping all VCSELs simultaneously, which is why we could not extend this study to larger detunings.

We explain the above-described behaviour with collective locking of all the VCSELs for $\lambda_{\mathrm{nc}} \leq 31\,\mathrm{pm}$. At $\lambda_{\mathrm{nc}} = 47\,\mathrm{pm}$, the first VCSELs unlock. Due to the VCSEL control unit only allowing for discrete pump currents, between the individual unlocked VCSELs there are wavelength inhomogeneities of up to 0.01 nm (s. Subsec. 2.3.1), which corresponds to about 3 GHz. In this case, one can observe beat frequencies between different VCSELs. Consequently, we link the peaks appearing in the RF spectra at $f < 3\,\mathrm{GHz}$ for $\Delta\lambda_{\mathrm{nc}} \geq 55\,\mathrm{pm}$ to these beat frequencies.

Taking the above considerations into account, we identify $\Delta\lambda_{\mathrm{nc,up}} = 47\,\mathrm{pm}$ as the upper boundary for full locking between VCSEL (3,3) and most of the non-central VCSELs. Similar to Eq. 4.2, we approximate the optical power of the ensemble of the non-central VCSELs at the top facet of VCSEL (3,3) at the upper locking boundary by

$$P_{\mathrm{nc}}|_{\mathrm{tf}(3,3)} \approx \sum_{(c,r)} T_{\mathrm{MO}}^2 T_{\mathrm{BS1}}^2 C_{\mathrm{DOE}}(c,r) P(c,r). \tag{4.6}$$

With this, we obtain

$$\frac{\Delta\lambda_{\mathrm{nc,up}}}{\sqrt{P_{\mathrm{nc}}/P(3,3)}\Big|_{\mathrm{tf}(3,3)}} \approx 41\,\mathrm{pm}, \tag{4.7}$$

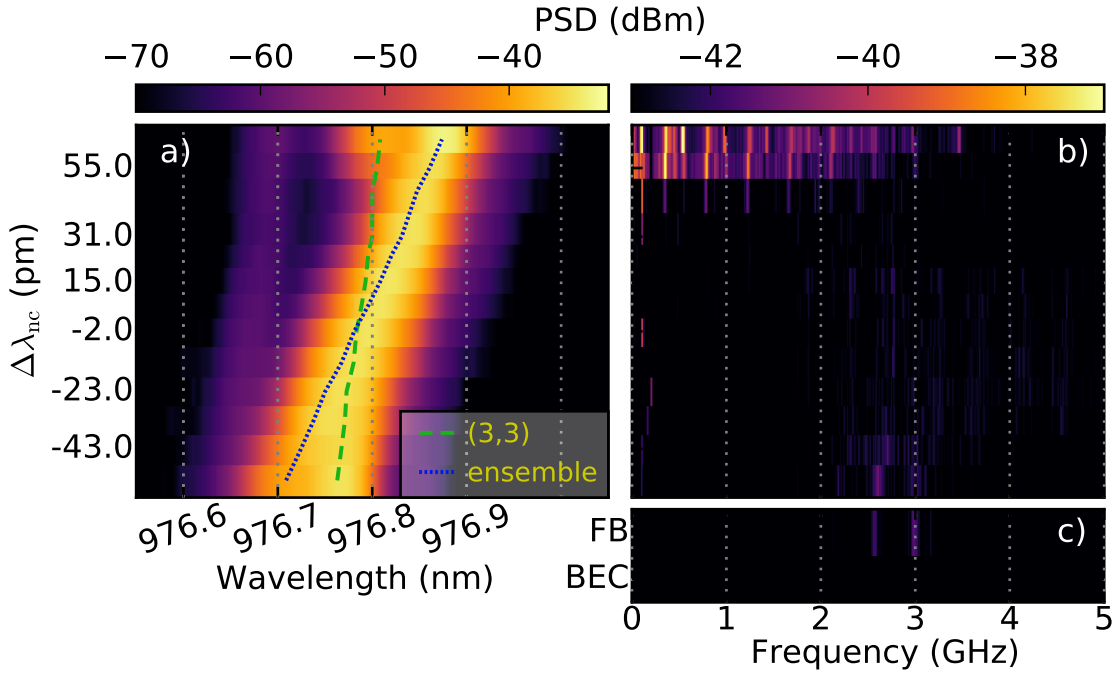

FIGURE 4.8: Stacked color-coded spectra of VCSEL (3,3) at $I(3,3) = 0.5\,\mathrm{mA}$ under entire array coupling. The y-axis represents the spectral detuning $\Delta\lambda_{\mathrm{nc}} = \lambda_{\mathrm{nc}} - \lambda(3,3)$. a) Optical spectra. Blue dotted line: spectral maximum λ_{nc} of the ensemble of the non-central VCSELs. Green dashed line: $\lambda(3,3)$ (not constant due to heating). Both obtained experimentally. The near-vertical violet trace at about 976.7 nm stems from VCSEL $(3,1)$, which is short-circuited with VCSEL (3,3) and can thus not be tuned independently. b) Corresponding RF spectra. c) RF spectra of solitary VCSEL (3,3) with FB and blocked external cavity ('BEC').

which is slightly higher than the value that we obtained from the fit in Fig. 4.6 for pairwise coupling, but still of a comparable magnitude. The proportionality of detuning and the square root of the optical power ratio is based on Eq. 1.3, which assumes a single monochromatic source and not several VCSELs with uncorrelated phases. That this ratio does not decrease when transitioning from pairwise locking to entire array locking thus corroborates our claim that most of the array's VCSELs are locked for $\Delta\lambda_{\mathrm{nc}} \leq 47\,\mathrm{pm}$. Here, we would also like to stress that we found comparable results to the ones shown in Fig. 4.8 in two more datasets.

4.3.2 Dynamical behaviour of non-central VCSELs

Up to this point in this section, we have mostly compared spectra of the central VCSEL, recorded in different experimental conditions. To get an insight into the dynamics of the whole array, we recorded RF spectra of the non-central VCSELs. For every VCSEL, we recorded two spectra: one for the solitary VCSEL with feedback and one with feedback and coupling to all the VCSELs of the array at wavelength matching conditions (s. Tab. 3.3). RF spectra for six VCSELs are shown in Fig. 4.9. The most frequently observed phenomena were as follows: In the RF spectra of four solitary VCSELs with feedback, namely (2,2), (2,3), (3,2), and (4,3), we find narrow peaks at $k f_{\mathrm{ext}}$, i.e. at integer multiples of the external cavity round-trip frequency, which we identify as external cavity modes since they decrease in height with increasing k. On the other hand, for more than half of the VCSELs (mostly those close to the edge of the array), the RF spectra of

the solitary VCSEL with feedback are similar to the background spectrum. For five VCSELs, namely (2,2), (3,2), (4,1), (4,2), and (4,3), the RF spectra in the coupled configuration show broad regions of high PSD for $f > 2.5\,\mathrm{GHz}$. Also in the coupled configuration, the RF spectra of more than half of the VCSELs (again mostly those close to the edge of the array) are similar to the background.

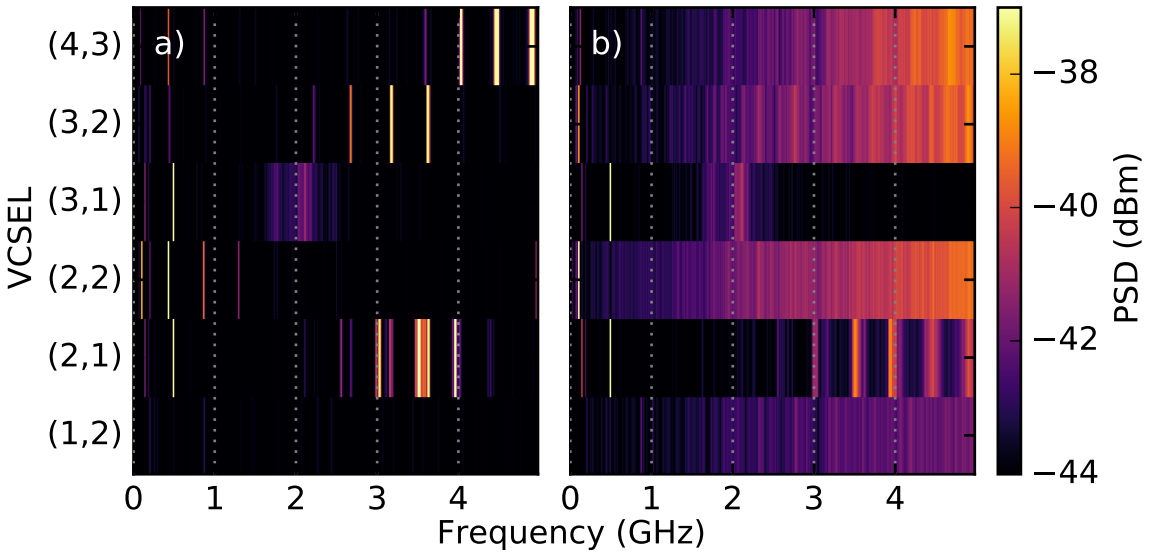

FIGURE 4.9: Stacked color-coded RF spectra of different VCSELs, which are specified on the y-axis. a) Solitary VCSEL (c, r) or short-circuited pair, with feedback. b) All VCSELs spectrally aligned, with feedback and coupling (s. Tab. 3.3).

4.3.3 Changes to the P-I characteristics

To compare the influence of coupling on the P-I characteristics of the VCSELs, we performed two experiments. In the first experiment, the pump current of all the VCSELs was incremented simultaneously, in steps of 0.01 mA, and the emitted optical power of the entire array was measured at every step. The results for blocked external cavity ('BEC') and for feedback ('FB'), i.e. not blocking the external cavity, are shown in Fig. 4.10, with a linear fit to the points corresponding to $I \geq 0.5\,\mathrm{mA}$. We used this linear fit to calculate a threshold current I_{th} and a slope efficiency η for both cases. From this, we can calculate the threshold reduction

$$\Psi_0 = \frac{I_{\mathrm{th}}(\mathrm{FB}) - I_{\mathrm{th}}(\mathrm{BEC})}{I_{\mathrm{th}}(\mathrm{BEC})} = \frac{0.376\,\mathrm{mA} - 0.380\,\mathrm{mA}}{0.380\,\mathrm{mA}} = -1.05\% \tag{4.8}$$

and the increase in slope efficiency

$$\zeta_0 = \frac{\eta(\mathrm{FB}) - \eta(\mathrm{BEC})}{\eta(\mathrm{BEC})} = \frac{2.34\,\mathrm{mW/mA} - 2.26\,\mathrm{mW/mA}}{2.26\,\mathrm{mW/mA}} = 3.42\%. \tag{4.9}$$

As can be seen from Fig. 4.10, the threshold reduction is barely visible in the plot and significantly smaller than the one of the central VCSEL with self-feedback without the DOE obtained in Subsec. 3.3.1. (Note that most of the results presented in that subsection were obtained with a different array.) The increase in slope efficiency, though, is visible in

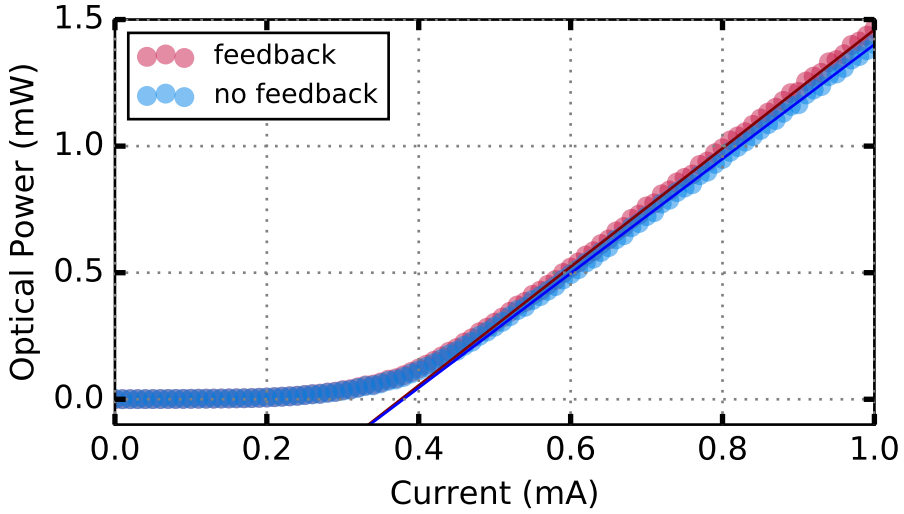

FIGURE 4.10: Optical power of the entire array vs. pump current I, at which all the VCSELs were pumped simultaneously – with feedback and coupling (red data), and with blocked external cavity (blue data). Lines: linear fits to the data for $I > 0.5\,\mathrm{mA}$.

the plot and larger than for the solitary VCSEL. Possible reasons for this increase are reflections of every VCSEL's emission at the DBR mirrors of its nearest and second-nearest neighbours as well as coupling effects of the lasers.

To investigate this further, we conducted a second experiment. For all 22 individually or only pairwise addressable VCSELs (c,r), we measured the increase in slope efficiency with feedback, $\zeta(c,r)$, analogically to Eq. 4.9 for two configurations: configuration 1 in which only the respective VCSEL is pumped, and configuration 2, in which all the other VCSELs are spectrally aligned (pump currents as listed in Tab. 3.3). The difference is, that in the first case, the increase can only be caused by self-feedback and reflections at the surface of other VCSELs, while in the second case the VCSELs can influence each other through coupling. For the first case, we calculated the threshold reductions $\Psi(c,r)$ analogically to Eq. 4.8, and results were similar to the ones shown in Fig. 4.10. For only two VCSELs (c,r) we measure $|\Psi(c,r)| > 1\%$, which means that for most VCSELs the threshold reduction due to coupling was below the measurement uncertainty. Still, for many VCSELs (c,r) there was a significant increase in $\eta(c,r)$ with feedback for both cases. In configuration 1, we obtain an average increase in slope efficiency

$$\overline{\zeta} = \frac{1}{22}\sum_{(c,r)} \zeta(c,r) = 3.8\%, \tag{4.10}$$

where 22 is the number of individually or pairwise addressable VCSELs. In configuration 2, we obtain $\overline{\zeta} = 4.3\%$. When comparing these results to the ones from Fig. 4.10, we can conclude that most of ζ_0 (as defined in Eq. 4.9) is caused by reflections at the array's surface.

In conclusion, we did not observe any significant threshold reduction due to coupling between VCSELs. We did observe an increase in slope efficiency, but this can be attributed mainly to reflections at the array surface.

4.4 External optical injection

As mentioned earlier, the DOE placed in the external cavity not only allows for coupling between VCSELs, but also for simultaneous optical injection from an external laser into all the VCSELs of the array. In this section, we present how the VCSELs respond to optical injection. We prove simultaneous optical injection-locking of all VCSELs of the array and find that their responses to intensity-modulated optical injection are promising for reservoir computing (RC).

4.4.1 Optical injection locking of the entire array

To investigate the simultaneous injection into all the VCSELs of the array, we recorded optical spectra of every VCSEL while varying the emission wavelength λ_{inj} of the injection laser by modifying its temperature T_{inj}. The injection laser's pump current was kept constant at $I_{\mathrm{inj}} = 450\,\mathrm{mA} = 9.66 I_{\mathrm{th,inj}}$. The resulting optical spectra of four VCSELs are shown in Fig. 4.11. Note that in comparison to the experimental setup shown in Fig. 2.7, an optical isolator is installed instead of a Mach-Zehnder modulator, which leads to an increase of the injection power by about 6 dB. We recorded similar data for all 24 non-central VCSELs. Due to the experimental geometry, it is impossible to record a similar spectrum for the central VCSEL without a gigantic crosstalk from the injection laser. The VCSELs were tuned to emit at the globally matched wavelength λ_{match} (s. Tab. 3.3). For all VCSELs, we found a range of T_{inj} at which their emission wavelength switched from λ_{match} to λ_{inj}. In this region, we also observed a suppression of the side mode of the respective VCSEL. These are classical signatures of optical injection locking. As visible in Fig. 4.11, the upper locking boundary is clearly defined, since the transitions to side-mode suppression and wavelength shift are abrupt. At the lower boundary, these transitions are continuous, which makes it harder to define a clear boundary. We define two measures for the width of the injection locking region. First, the highest detuning between the injection laser and the VCSEL at which we observe a side-mode suppression of at least 5 dB. For 21 of 24 VCSELs, this provides a clear result, while for the remaining 3 VCSELs, the side-mode's intensity was too low or their suppression was too weak. We define this detuning as $\Delta\lambda_{\mathrm{lock}}$, and it is indicated in Fig. 4.11 by a green dashed line. Second, the maximal shift of the spectral peak wavelength with respect to the VCSEL's wavelength far from the injection locking region, as shown for pairwise coupling in Fig. 4.5, which we define as $\Delta\lambda_{\mathrm{peak}}$. For this, we extracted the peak wavelength from the spectra as described in Subsec. 2.4.2. The peak wavelength of every spectrum is indicated by a blue dot in Fig. 4.11. The values for the width of the locking region that we obtain with both methods are given in Tab. 4.2.

TABLE 4.2: Left: highest detuning between VCSEL and injection laser at which we observe a side-mode suppression of more than 5 dB ($\Delta\lambda_{\mathrm{lock}}$). Right: maximal shift of the peak wavelength under optical injection locking to the external laser ($\Delta\lambda_{\mathrm{peak}}$). We observe good agreement between both sets of values.

$\Delta\lambda$ (pm)	(1,*)	(2,*)	(3,*)	(4,*)	(5,*)
(*,1)	15/14	22/20	-/59	9/8	16/18
(*,2)	26/24	33/33	62/62	33/33	-/5
(*,3)	51/51	45/45	-	41/41	34/32
(*,4)	29/29	45/46	75/76	-/20	11/9
(*,5)	29/28	53/53	23/22	32/33	14/12

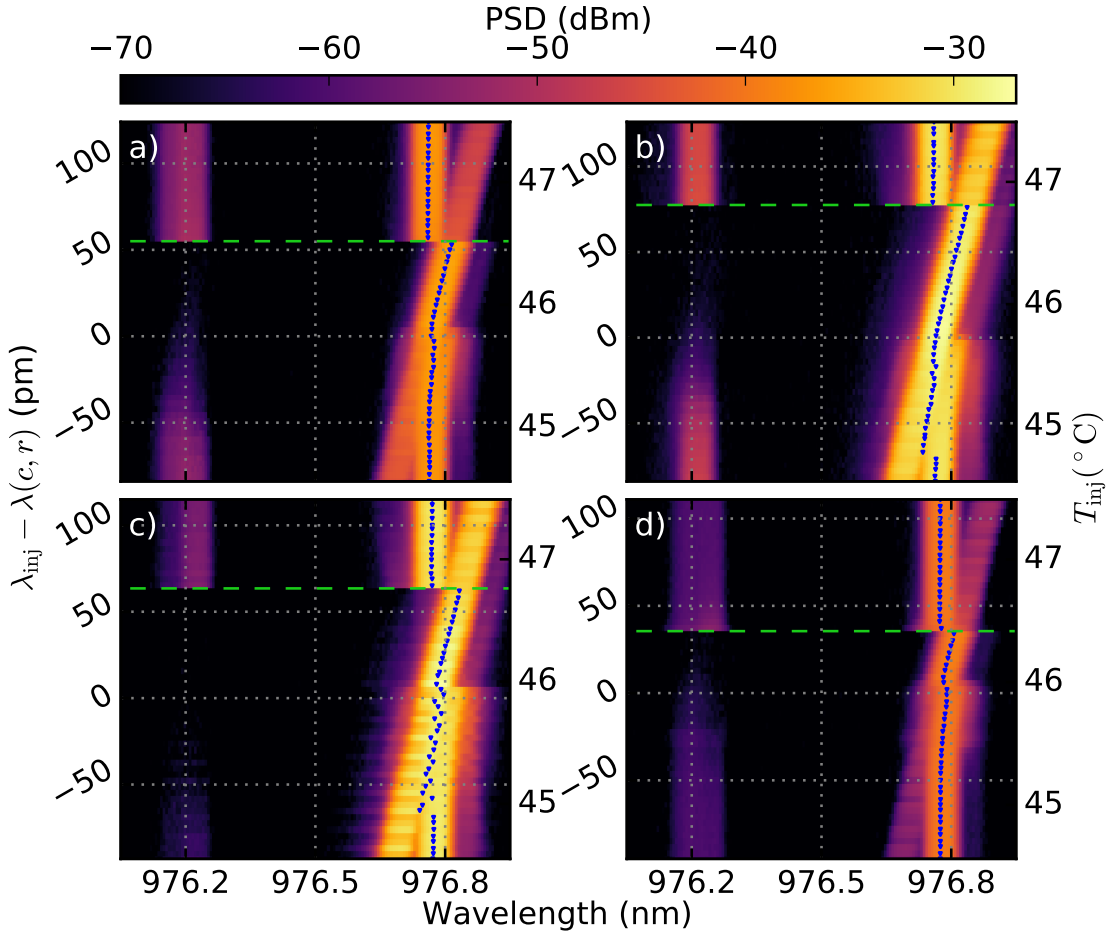

FIGURE 4.11: Stacked color-coded optical spectra of four different VCSELs with injection from an external DBR laser. The injection laser frequency λ_{inj} was varied via T_{inj} and is given on the y-axis. Blue dots indicate the spectral maxima, which we obtained as described in Subsec. 2.4.2. Green dashed lines indicate the upper boundaries of side-mode suppression. Top left: VCSEL (2,5), bottom left: VCSEL (3,2), top right: VCSEL (3,4), bottom right: VCSEL (5,3).

We assume a similar scaling for injection locking to an external injection laser as for bidirectional coupling between two VCSELs. To verify this hypothesis, we approximate the optical power of the injection laser at the top facet of VCSEL (c,r) by

$$P_{\mathrm{inj}}\big|_{\mathrm{tf}(c,r)} \approx T_{\mathrm{MO}} T_{\mathrm{BS1}} R_{\mathrm{BS1}} C_{\mathrm{DOE}}(c,r) P_{\mathrm{inj}}, \tag{4.11}$$

where P_{inj} is the optical power of the injection laser after the optical isolator, $T_{\mathrm{MO}} = 0.9$, $T_{\mathrm{BS1}} = 0.48$, and $R_{\mathrm{BS1}} = 0.46$ are the transmission and reflection coefficients of microscope objective and 50/50 beam splitter, respectively, and $C_{\mathrm{DOE}}(c,r)$ is the multiplexing matrix coefficient for a double-pass through the DOE as given in Fig. 2.4. From this approximation and the values in Tab. 4.2, we obtain the data plotted in Fig. 4.12. The linear fit gives a slope of $b = 39$ pm, which is slightly higher than what we obtained for bidirectional coupling between array VCSELs and close to the value for entire array coupling. Using Eq. 4.4 with $2 < \alpha < 5$, we obtain $15\,\mathrm{ns}^{-1} < k_c < 35\,\mathrm{ns}^{-1}$, which is comparable to values found for similar VCSELs [9] and for VCSELs emitting at 1550 nm with optical injection via optical fibers [88]. This indicates that the external injection laser is optically well-aligned.

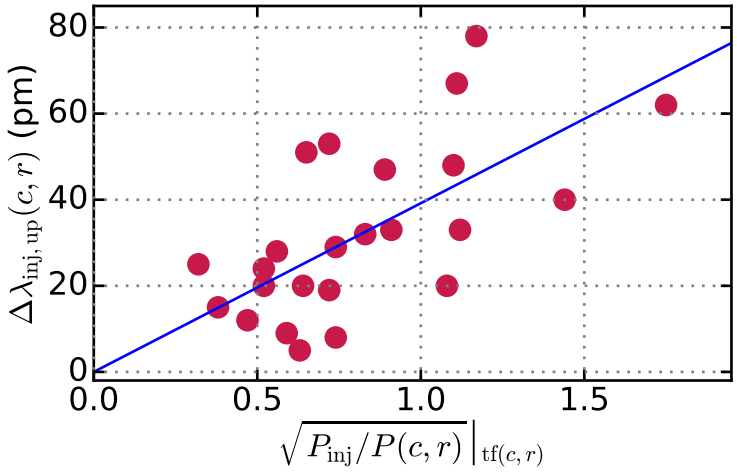

FIGURE 4.12: Maximal detuning at which we observe optical injection locking to the external laser vs. optical power ratio at top facet of VCSEL (c, r). Blue line: linear fit.

After this first experimental confirmation that the alignment allows for simultaneous injection into all the VCSELs, we aimed to simultaneously lock all array VCSELs to the injection laser. Plotting the spectral peaks that were extracted from spectra like in Fig. 4.11 together in Fig. 4.13, we observe that at around $\lambda_{\mathrm{inj}} = 976.79\,\mathrm{nm}$, due to optical injection locking, most of the initially slightly spectrally inhomogeneous VCSELs emit at the same wavelength. However, we find no wavelength λ_{inj} at which all the VCSELs are locked simultaneously. So, to prove simultaneous optical injection locking of all array VCSELs, we left the injection laser temperature constant at $T_{\mathrm{inj}} = 46.8\,^{\circ}\mathrm{C}$ and optimized the VCSELs' pump currents for visibility of locking effects, which results in tuning them closer to the upper locking boundary. Still, we stayed within $0.2\,I_{\mathrm{th}}$ of I_{match} for all VCSELs. Then, we recorded three optical spectra of each VCSEL: one with feedback and injection, one with blocked external cavity and thus blocked injection, and one with feedback but without injection. The results for four VCSELs are shown in Fig. 4.14. For all the independently tunable VCSELs and one VCSEL of each short-circuited pair (i.e. 21 out of 23 VCSELs, not only the shown ones), we observe a shift of the right peak or suppression of the left peak or both when comparing the spectra recorded with optical injection to the spectra recorded without it. We conclude that all of these VCSELs are simultaneously optically injection locked to the external injection laser.

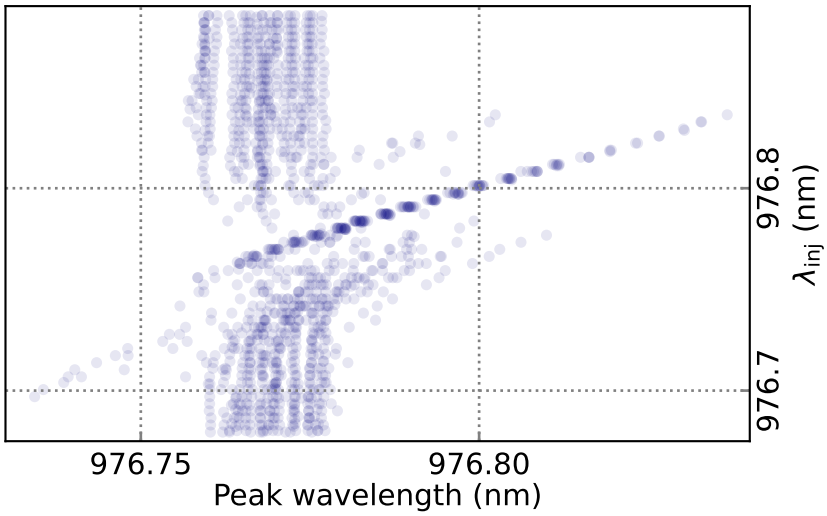

FIGURE 4.13: Wavelengths of spectral peaks of different VCSELs under optical injection at different wavelengths. Under optical injection at around $\lambda_{inj} = 976.79\,nm$, most of the slightly spectrally inhomogeneous VCSELs are forced to the same wavelength.

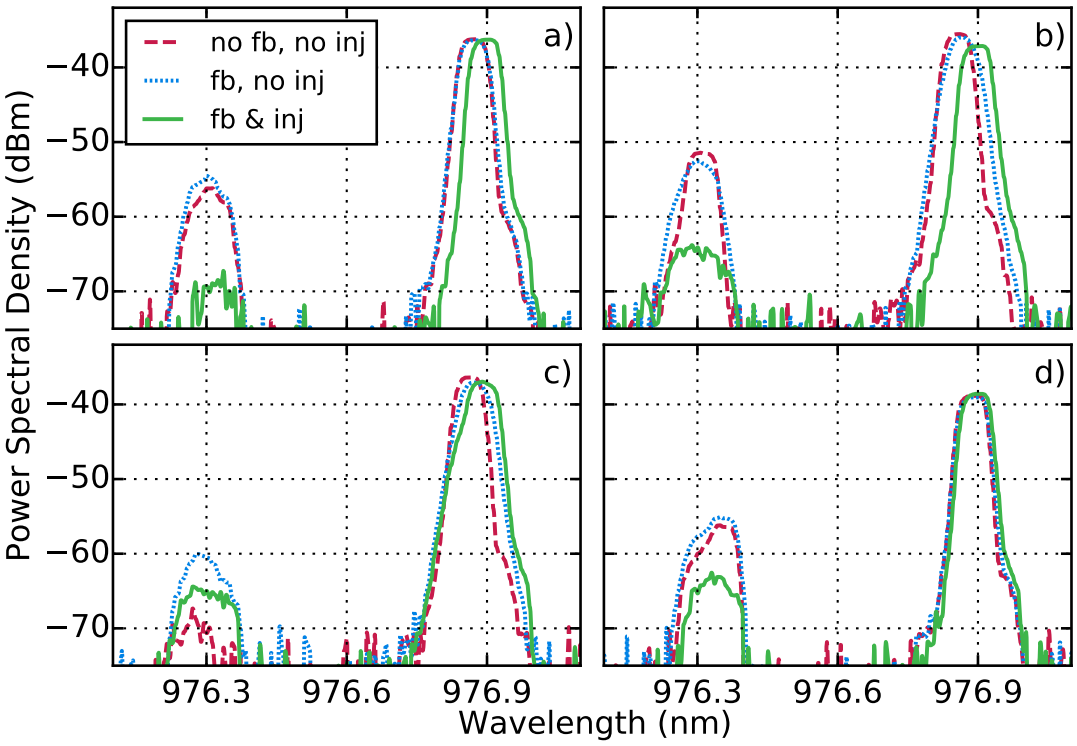

FIGURE 4.14: Optical spectra of four different VCSELs in three different configurations. The dashed red lines correspond to blocking the external cavity, which results in no feedback and no injection. The dotted blue lines correspond to blocking the injection path, which does not affect the feedback. The solid green lines correspond to a configuration with both feedback and injection. a) VCSEL (2,5), b) VCSEL (3,4), c) VCSEL (3,2), d) VCSEL (5,3). For all independently tunable VCSELs (i.e. 21 out of 23 VCSELs, not only the shown ones), we observe a shift of the right peak or suppression of the left peak or both due to optical injection.

4.4.2 Dynamic response to intensity-modulated injection

Knowing that it is possible to achieve simultaneous optical injection locking of 21 array VCSELs, it is interesting how the individual VCSELs react when modulating said injection. For this, we modulated the intensity of an external injection laser as described in Sec. 2.3. We injected a series of 1000 uniformly distributed pseudo-random numbers from 0 to 1 at an input rate of $f_{\text{in}} = 454.54545\,\text{MS/s}$. We define the n^{th} number of this series as r_n. We chose f_{in}, because $f_{\text{in}} = f_{\text{ext}} = \tau_{\text{ext}}^{-1}$, with τ_{ext} being the external cavity round-trip time. Furthermore, operating at f_{in} means that one r_n is injected every 2.2 ns, which at an oscilloscope sampling rate of $f_{\text{smp}} = 5\,\text{GS/s}$ is equal to 11 sampling points. An integer number of sampling points per injected r_n is convenient for processing and for compensating for the lag that is described in the following. To verify that $f_{\text{in}} = \tau_{\text{ext}}^{-1}$, we recorded two time traces. The first time trace was the (attenuated) signal of the injection laser, the second time trace was the reflection of that signal at the surface of VCSEL (2,3). We expect both time traces to be qualitatively similar and the second one to lag behind by τ_{ext}, since the signal passes through the external cavity before being detected. In Fig. 4.15, both time traces are plotted with different scalings. The injection signal was shifted by τ_{ext} to the right to compensate for the expected lag. Indeed, we observe that they are qualitatively nearly identical. Also, we verified that this is true for the entire range of 1000 random numbers.

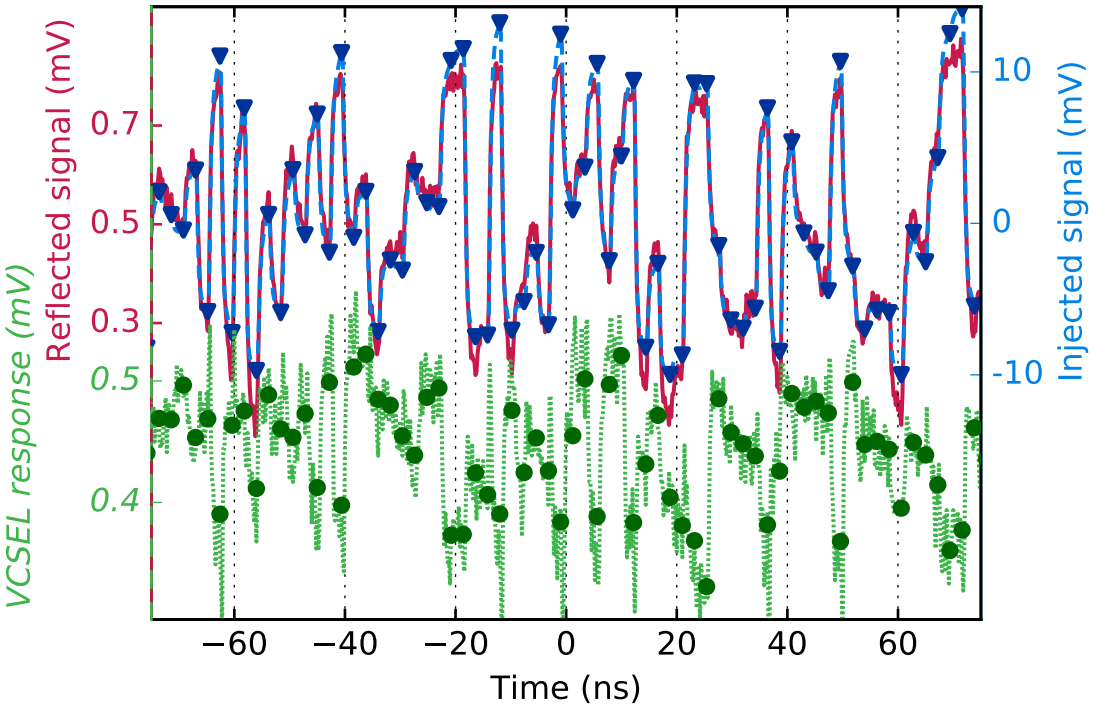

FIGURE 4.15: Injection laser time trace, directly measured (blue dashed line) and after reflection at the surface of VCSEL (2,3) (red solid line), and response of VCSEL (2,3) (green dotted line). The dark green circles represent q_n, the averaged response to the injection of r_n. The dark blue triangles represent s_n, the last sample point of the injection signal corresponding to r_n (for exact definition see text and Eqs. 4.12 and 4.13). The blue dashed line was shifted $\tau_{\text{ext}} = 2.2\,\text{ns}$ to the right. All time traces were averaged 1024-fold to improve the SNR. Notice the different y-axes.

As a next step, we recorded the dynamical response of the VCSELs to injection. Due

to the experimental geometry, we could only record the response of one VCSEL at a time and repeated the experiment at identical conditions. To record the responses, the VCSEL pump currents were adjusted as for optimized optical injection locking, as described in the previous subsection. In Fig. 4.15, the injection laser signal is plotted as well as the response of VCSEL (2,3). It is apparent that the VCSEL's response (green) differs qualitatively from the injection (blue) and the reflection (red). Additionally, the figure contains two scatter plots, which will be explained in the following. We define the i^{th} point of the recorded injection laser signal as S_i and the i^{th} point of the recorded response of VCSEL (c, r) as $Q_i(c, r)$. When correctly synchronized, the points from S_{11n} to S_{11n+10} and from Q_{11n} to Q_{11n+10} correspond to the injection of r_n. The blue triangles represent

$$s_n := S_{11n+10}, \tag{4.12}$$

which is the last point corresponding to the injection of the respective r_n. It makes sense to check how accurate the random number injection is at this point, since there the signal has had the most time to approach the injected value. We obtain that $\{s_n\}$ and $\{r_n\}$ have a Pearson correlation of $\rho = 0.990$, which means that the experimentally measured intensity modulation follows the theoretically desired one nearly exactly. The green circles represent

$$q_n(c, r) := \frac{1}{9} \sum_{j=0}^{8} Q_{11n+j+2}(c, r), \tag{4.13}$$

the average of the response of VCSEL (c, r) (in Fig. 4.15, $(c, r) = (2, 3)$) to the injection of r_n, excluding the first two points for transient behavior. We use this average for analyzing the VCSELs' responses to the injection.

In Fig. 4.16, the average response $q_n(c, r)$ of four different VCSELs (c, r) to the injection of random numbers r_n is shown. To analyze the responses, we fit the data with a linear function $g_1(r_n)$ and with a 5th order polynomial $g_5(r_n)$. We observe different behaviors, like linear and non-linear responses and noise-dominated signals. We use four measures to characterize linear, nonlinear, and noisy responses. To quantify linearity, we use the Pearson correlation ρ of $\{r_n\}$ and $\{q_n\}$. To quantify how much a response resembles pure Gaussian noise, we use the p-value of the omnibus test by D'Agostino [93]. To quantify the nonlinearity of the response, we define

$$y_{\text{NL}} := \max_{x \in [0;1]} |g_5(x) - g_1(x)| / U_{\text{noise,RMS}}, \tag{4.14}$$

where $U_{\text{noise,RMS}} = 0.0133\,\text{mV}$, as obtained from the following considerations. The root mean square (RMS) vertical noise floor of the oscilloscope is given as 1.28 mV. Periodically averaging 1024-fold reduces the noise by a factor of 32 [94] to 0.04 mV, averaging nine consecutive sample points reduces this further down to $U_{\text{noise,RMS}} = 0.0133\,\text{mV}$. For the signal-to-noise ratio (SNR), we divided the standard deviation of the signal by $U_{\text{noise,RMS}}$. In Tab. 4.3, these four measures are given. They are averaged over three measurement series. The given deviation equals half the maximal deviation between values from different measurements. Most VCSELs did not respond consistently to the injection, as is evident from the large deviations. This means that the VCSEL response is very sensitive to the exact experimental conditions, which cannot even be completely restored by realignment to the reference fiber. Also, there are some VCSELs, especially those in column 5, whose signal is comparable to the noise floor, so we have probably recorded mainly noise. Still, we can make important observations, such as that there are VCSELs that respond consistently linearly to the injection, like (3,4), (4,3) or (1,3). Others, notably (2,3) and (2,4) respond mainly nonlinearly. For many other VCSELs, the inconsistency

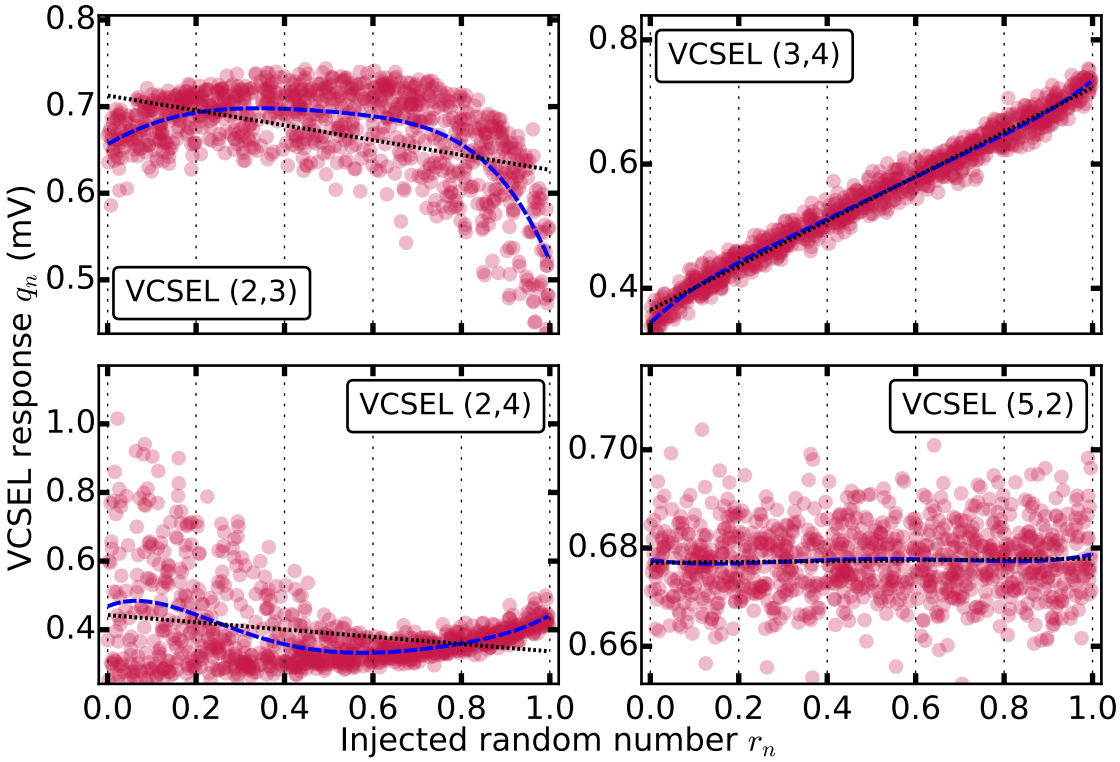

FIGURE 4.16: Dynamic responses of four different VCSELs to the injection of random numbers with the injection laser. Every red circle represents the response q_n to a random number r_n. The responses are fitted linearly (dotted black line) and with a 5th order polynomial (dashed blue line). The VCSELs exhibit a large variety in their responses. Some VCSELs follow the injection signal linearly, like (3,4), others respond nonlinearly, like (2,3) or (2,4). Moreover, VCSEL (2,4) shows a large spread of responses to the same random number, hinting hysteresis or chaos. For some VCSELs, like (5,2), we measured a very low SNR.

in their responses makes general statements impossible. We cannot conclusively relate the optical injection locking range to how linear, non-linear, or noisy a response is. The measure for linearity correlates with $\rho = 0.55$ with the locking range, the measure for noise with $\rho = -0.55$, and the measure for non-linearity with $\rho = 0.40$. At least the first two suggest that a broad locking range favours a more linear and less noisy response, although these values are too small for conclusive statements. However, here we also have to take into account that we retuned the VCSELs, so that they are all similarly detuned from the upper locking boundary. The only significant correlation is the one between SNR and locking range, with $\rho = 0.69$.

Still, we can conclude that, although we have to fight with a low SNR, we observe varied and interesting responses of the VCSELs to the injection, which are promising prerequisites for implementing reservoir computing with the experimental system.

TABLE 4.3: Pearson correlation ρ, measure for nonlinearity y_{NL} (see Eq. 4.14), D'Agostino p-value for normality, and signal-to-noise ratio (SNR) for the VCSELs' dynamic response to injection, given below each other in the given order. The given uncertainty is half the difference between the highest and the lowest value we obtained in three measurements. Due to technical limitations of the control unit there are no results for VCSEL (1,5). Due to the experimental geometry, it is impossible to obtain results for VCSEL (3,3).

$\rho(r_n, q_n(c,r))$ y_{NL} D'Agostino p SNR	(1,*)	(2,*)	(3,*)	(4,*)	(5,*)
(*,1)	0.19 ± 0.70 1.33 ± 1.49 0.22 ± 0.33 1.90 ± 1.05	0.35 ± 0.19 0.31 ± 0.28 0.21 ± 0.30 0.65 ± 0.04	0.56 ± 0.27 0.67 ± 0.60 0.12 ± 0.17 0.96 ± 0.29	-0.33 ± 0.17 0.37 ± 0.13 0.00 ± 0.00 0.70 ± 0.07	0.25 ± 0.35 0.10 ± 0.04 0.45 ± 0.12 0.50 ± 0.08
(*,2)	0.16 ± 0.34 0.31 ± 0.09 0.02 ± 0.03 1.01 ± 0.36	0.04 ± 0.65 1.29 ± 0.55 0.00 ± 0.00 1.29 ± 0.54	0.55 ± 0.57 1.75 ± 0.55 0.00 ± 0.00 6.91 ± 4.20	-0.32 ± 0.05 0.68 ± 0.46 0.21 ± 0.17 1.49 ± 1.16	0.10 ± 0.07 0.09 ± 0.03 0.47 ± 0.46 0.56 ± 0.02
(*,3)	0.81 ± 0.10 0.51 ± 0.36 0.00 ± 0.00 2.40 ± 1.30	0.07 ± 0.71 5.07 ± 2.74 0.00 ± 0.00 3.51 ± 0.37	-	0.90 ± 0.05 2.41 ± 1.58 0.00 ± 0.00 2.93 ± 1.02	0.31 ± 0.36 0.34 ± 0.22 0.24 ± 0.23 0.76 ± 0.27
(*,4)	0.81 ± 0.19 1.07 ± 0.69 0.15 ± 0.23 4.82 ± 2.88	0.11 ± 0.54 4.61 ± 3.17 0.00 ± 0.00 6.28 ± 2.19	0.94 ± 0.06 1.47 ± 0.41 0.00 ± 0.00 7.07 ± 1.80	0.40 ± 0.54 0.62 ± 0.25 0.00 ± 0.00 1.05 ± 0.36	-0.10 ± 0.16 0.32 ± 0.18 0.51 ± 0.24 0.54 ± 0.11
(*,5)	-	0.47 ± 0.59 1.19 ± 0.76 0.00 ± 0.00 2.18 ± 1.74	0.56 ± 0.55 2.64 ± 1.81 0.00 ± 0.00 3.09 ± 1.65	-0.17 ± 0.71 0.92 ± 0.30 0.00 ± 0.00 0.92 ± 0.26	0.14 ± 0.09 0.12 ± 0.02 0.18 ± 0.01 0.46 ± 0.05

4.5 Summary and conclusion

In this chapter, we have elaborated on various results obtained with the diffractively coupled VCSELs. We observe optical injection locking of the central VCSEL (3,3) with 14 of 21 individual non-central VCSELs or VCSEL pairs, and the radio-frequency spectra of the central VCSEL show signatures of interaction with all non-central VCSELs or VCSEL pairs. When coupling the entire array, we observe optical injection locking of VCSEL (3,3) with most of the VCSELs within the array. We observe optical injection locking to an external DBR laser for all VCSELs and achieve simultaneous locking of all 21 independently tunable VCSELs. Analyzing the optical injection locking regions, we find coupling coefficients (as defined in Eq. 1.3) in the range $13\,\mathrm{ns}^{-1} < k_c < 35\,\mathrm{ns}^{-1}$ for pairwise and entire array coupling, and for external optical injection, assuming a linewidth enhancement factor of $2 < \alpha < 5$. Furthermore, these coupling coefficients are of the same order of magnitude as measured in previous experiments with similar and with different VCSELs, both with more direct optical injection without diffractive coupling. Besides, we find that the coupling does not significantly contribute to a threshold reduction. It does, though, cause a higher slope efficiency, although this is probably due to reflections on the VCSEL array surface. Finally, we investigated the dynamic response of the VCSELs

to modulated injection. We find that most VCSELs do not show a consistent response to the modulation. Moreover, for some VCSELs, the signal is so small that our measurements are dominated by noise. Still, we find a rich variety of responses for different VCSELs. Some VCSELs respond consistently linearly, while others show different types of nonlinearities.

We can conclude that we have demonstrated coupling of the central VCSEL to every individual non-central VCSEL. This coupling and the properties we find for external optical injection are promising prerequisites for implementing reservoir computing, which will be treated in depth in the next chapter.

Chapter 5

Towards reservoir computing (RC)

Knowing how the VCSELs behave under coupling and injection conditions, their information processing properties can be explored. In this chapter, we will introduce the intended implementation and evaluate the reservoir's performance on some basic benchmark tasks.

5.1 A VCSEL reservoir computer

As explained in Sec. 1.3, a reservoir computer consists of an input layer, a reservoir with recurrent connections between nonlinear elements, and an output layer, as well as connections from one layer to another. All of these layers and connections corresponds to different parts of our experimental setup, as shown in Fig. 5.1 and explained in the following.

The input layer of our reservoir computer is realized by the intensity-modulated injection laser. That laser's output passes a Mach-Zehnder modulator (MZM), which, in combination with an arbitrary waveform generator (AWG), allows for modulation of the injection laser's intensity according to the desired input information. For technical details regarding the modulation, see Sec. 2.3. In our case, periodically repeated sequences of N real values were injected into the reservoir at a rate equal to the external cavity frequency f_{ext}. We will denote these values by r_n, where $1 \leq n \leq N$.

The VCSELs represent the nodes of our reservoir. Both the connections between nodes and the connections from the input layer to the reservoir are established via the external cavity. The connections from the input to the reservoir correspond to the injection (see Sec. 4.4). Since we inject into all the VCSELs of the array, the input layer is connected to every node of the reservoir, although the strengths of these connections are not homogeneous. In a hypothetical perfect alignment, they are given by the values in Fig. 2.4. Since the connections between nodes correspond to the coupling between VCSELs, the theoretical and experimental details related to this can be found in Sec. 2.2 and Sec. 4.1, respectively. In summary, the reservoir nodes are locally connected to their nearest and second-nearest neighbours and all the connections are bidirectional. Being established with the same mechanism, they vary in their magnitude in a similar fashion as the connections from the input to the nodes.

To obtain the response of the nodes to the input, we record the VCSELs' signals with a photodiode and an oscilloscope. As described in Subsec. 4.4.2, we average the VCSELs' response over various repetitions of the same input sequence. In our experiments, we use the same input rate f_{in} and oscilloscope sampling rate f_{smp} as in Sec. 4.4.2, which means that 11 sampling points of the averaged VCSEL output correspond to the injection of one r_n. We obtain the response $q_n(c,r)$ of VCSEL (c,r) to r_n as in Eq. 4.13, i.e. by discardig the first 2 sampling points and averaging over the remaining 9 that correspond to the injection of r_n. To simplify the notation, we number the VCSELs' responses. For this, we assign a natural number j, where $1 \leq j \leq J$, to each VCSEL (c,r), whose response we use in the output layer. Since two of our 25 VCSELs cannot be used as nodes, $J \leq 23$. The signal of VCSEL (3,3) cannot be detected due to the experimental geometry and VCSEL

(1,5) was switched off due to problems with the VCSEL control unit. This leads to the notation

$$q_{n,j} := q_n(c, r). \tag{5.1}$$

The output layer is implemented offline, using a conventional computer.

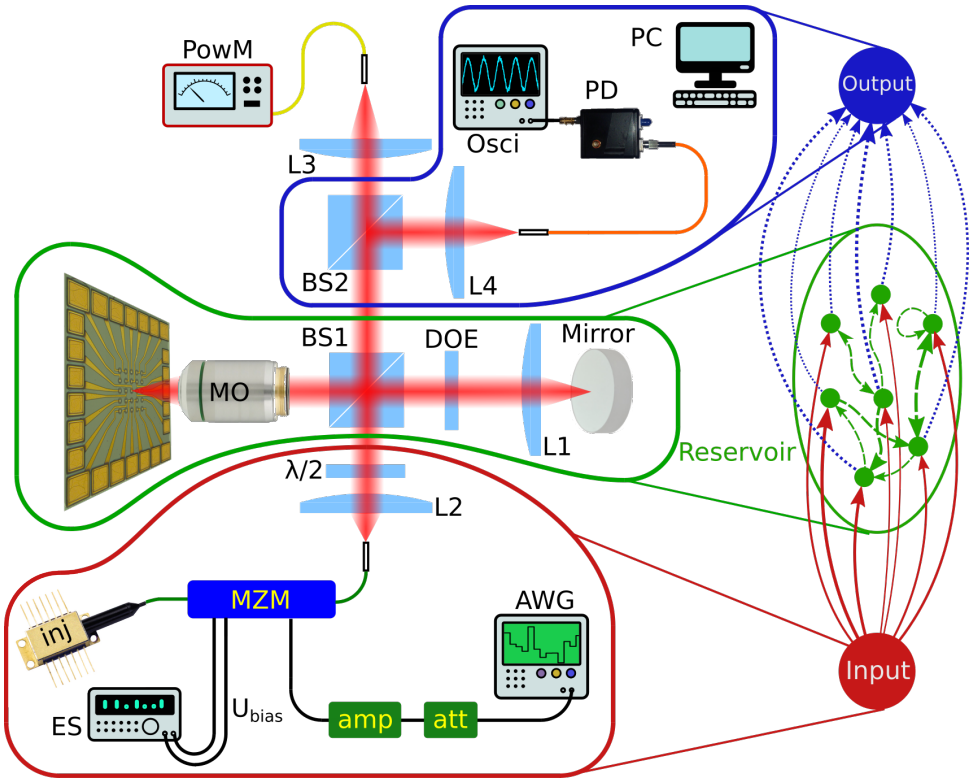

FIGURE 5.1: Correspondence of the experimental components to the layers of a reservoir computer. In our setup, the input is realized via modulated injection, and the VCSELs that are coupled via diffraction in the external cavity constitute the reservoir. For computing, the output of every VCSEL still has to be recorded separately, and the weights are applied offline on a conventional computer. Abbreviations as in Fig. 2.7.

To obtain the output of a reservoir computer, the nodes' responses are multiplied by output weights w_j contained in the J-dimensional vector $\mathbf{w}_{\text{train}}$. As described in Sec. 1.3, these weights are determined by a process called training. For all our tasks, we know the target output series, whose elements we define as y_n, where $1 \leq n \leq N$. We split our data in two data sets: the training set for determining the output weights and the testing set for evaluating the reservoir's computing performance. We define the set S such that it contains all the indices n that correspond to the training set. Then, we use ridge regression / Tikhonov regularization, which means that we find a weight vector $\mathbf{w}_{\text{train}}$ such that

$$\mathbf{w}_{\text{train}} = \text{argmin}_{\mathbf{w}\in\mathbb{R}^J} \left(\sum_{n\in S} \left(y_n - \sum_{j=1}^{J} q_{n,j} w_j \right)^2 + \alpha \sum_{j=1}^{J} w_j^2 \right), \tag{5.2}$$

where the scalar α is a penalizing parameter that forces the weights to smaller values.

The n^{th} value of the reservoir output a_n is then

$$a_n = \sum_{j=1}^{J} w_j q_{n,j}. \tag{5.3}$$

For tasks with non-continuous target values, like e.g. classification tasks, it might be necessary to map this output onto the possible results. Comparing a_n to y_n for all $n \notin S$ by using a suitable measure, one can evaluate the performance of the reservoir. This is called testing, often based on k-fold cross-validation. For this, the data set is split into k equally large subsets. All of them but one are used for training and the remaining one is used for testing. This procedure is repeated until every subset has been used for testing once, and the reservoir performance is the average of the k tests.

5.2 Basic benchmark performance

The first step towards RC with VCSEL arrays that we took was testing the performance on several benchmark tasks like the memory capacity (MC), the exclusive or (XOR) task, header recognition (HR), and digital-to-analog conversion (DAC). For all the results presented in this chapter, we injected a sequence consisting of random inputs r_n with $1 \leq n \leq N = 1000$. For the memory task, r_n were random numbers; for the other tasks r_n were random bits. The input was periodically repeated, and the VCSELs' responses were averaged to improve the signal-to-noise ratio (SNR). Note that, with a hardware-implemented output layer, the uncorrelated noise of different emitters would be averaged, which would improve the SNR [95] and reduce the need for periodical averaging. We obtained the weights by offline training with a target sequence y_n, as described in Eq. 5.2. For all the tasks, we performed five-fold cross-validation as described in the previous section. The reservoir performance is always evaluated based on the testing and not on the training. Which measure we used for our analysis differs for each task, and is specified in the respective section. For training, when not specified otherwise, we set the ridge regression parameter to $\alpha = 0.1$, although varying α over various orders of magnitude did not significantly change the results, which is commonly observed in analog hardware systems due to the presence of noise. Unless specified otherwise, all experiments were carried out under the same conditions as the ones in Subsec. 4.4.2, i.e. the injection laser temperature $T_{\text{inj}} = 46.8°\text{C}$ and for all the VCSELs $\lambda \approx \lambda_{\text{match}}$ (s. Tab. 3.3) with a slight modification for optimized locking. The main experimental parameter that we varied was the injection laser attenuation ϵ. We also recorded time traces with the VCSELs switched off, but with fiber tip and lens in the same position as for recording the VCSEL response, which means that we recorded the reflection of the injection laser at the VCSEL surfaces. This gives us the same number of nodes and thus makes it possible to obtain values for comparison to this linear version of the reservoir, where the nonlinearity is simply in the readout layer [96]. For the three tasks XOR, HR, and DAC, we did not record separate experimental data sets, but carried out the offline training on the exact same data.

5.2.1 Memory capacity (MC)

Memory is an important property for several reservoir computing tasks [75]. To quantify the memory of our reservoir, we calculate the memory capacity as defined by Jaeger [97]. This means that the reservoir is trained to retrieve the random numbers r_{n-k} that were

injected k steps before. Thus, target values differ for every k according to

$$y_{n,k} = r_{n-k}, \tag{5.4}$$

which is illustrated in Fig. 5.2. Hence, each k requires a dedicated training step to optimize the readout weights.

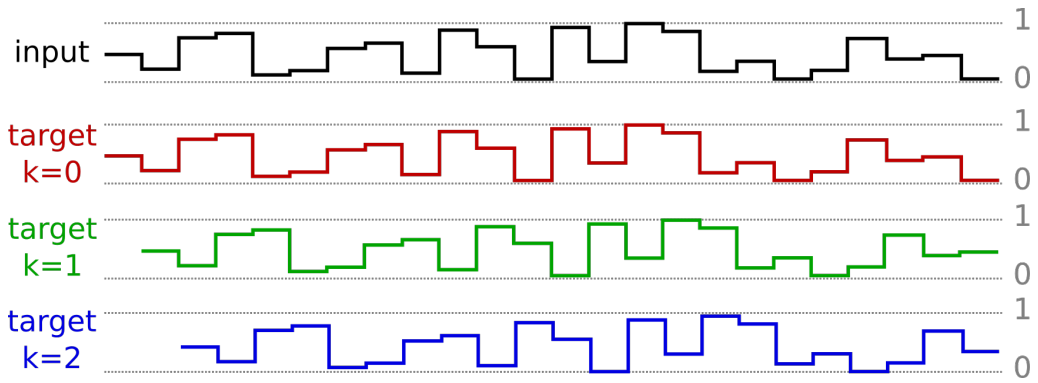

FIGURE 5.2: Example target values for the MC task for a given input. For each k, the reservoir aims to reproduce the input value from k time steps ago. For example, for $k = 0$, the target equals the input.

We calculate the memory correlation M_k as the squared Pearson correlation between the output $a_{n,k}$ and the target r_{n-k} for the testing set, i.e.

$$M_k = \left(\frac{\sum_{n \notin S} (a_{n,k} - \bar{a})(r_{n-k} - \bar{r})}{\sigma_A \sigma_R} \right)^2, \tag{5.5}$$

where $\bar{a}$ and $\bar{r}$ are the means of the sets $\{a_n\}_n$ and $\{r_n\}_n$, σ_A and σ_R are their standard deviations, and S contains all the indices of the training set. Actually, the weights differ for each cycle of the cross-validation. However, as explained in the introduction to this section, we obtain exactly one output $a_{n,k}$ for every n and k, and we evaluate the testing results in relation to this output. The value M_k corresponds to the ability of the reservoir to retrieve the input that was introduced k steps before. Note that there are publications that do not use the square as in the original definition, which is why our memory properties could seem lower than they are in comparison. We define the memory capacity MC as

$$\mathrm{MC} = \sum_{k=0}^{K} M_k, \tag{5.6}$$

where K is an integer that we choose such that M_k is small for $k > K$. This avoids that principally negligible M_k, which can e.g. be due to noise, contribute to the memory capacity. The selection of a particular K is based on a heuristic estimation, yet as long as we choose the same K, we can compare values between measurements.

In Fig. 5.3, data for M_k is shown for different experimental conditions. We observe that the currently injected random number ($k = 0$) can always be reproduced well. After that, the memory correlation decreases mostly monotonically until in all the shown cases it has decayed to $M_k < 0.03$ for $k \geq 10$. We observe that using the VCSEL signals instead of the reflection increases M_k for $k \geq 2$. An injection laser attenuation $\epsilon = 2\,\mathrm{dB}$ led to a decrease of M_k for $k \leq 2$ but to an increase for $3 \leq k \leq 8$. We observed similar behaviour for $\epsilon = 6\,\mathrm{dB}$. Importantly, when using the reflection of the injection laser at the VCSEL surfaces instead of the VCSELs' outputs, the memory does not decay immediately, most

notably $M_1 = 0.82$. Here, the most important contribution is probably the inherent memory of the AWG, which has been observed before and has been ascribed to the AWG's finite analog bandwidth [75]. Interestingly, the memory capacity that we obtained for the reflections is comparable to the one obtained for the direct output of the AWG by Julián Bueno [98], although there are essential differences between the two experiments. In Ref. [98], more than 10 times more nodes were used, the correlation was not squared, and, most importantly, both modulation and detection were about one order of magnitude faster. We modulated the signal at about 500 MS/s and detected it at 5 GS/s, while in Ref. [98], the modulation was at 5 GS/s and the detection at 40 GS/s. Still, in both cases, M_0 and M_1 are close to 1, but decay quickly for higher k. Thus, in our case, not the full memory that we obtain for the reflections can be ascribed to the AWG's finite analog bandwidth. However, even with the VCSELs switched off, there might be a contribution from the VCSELs. In Tab. 5.1, the memory capacities, calculated as the sums $\sum_{k=0}^{9} M_k$, are summarized for the data shown in Fig. 5.3 and another measurement. The absolute values obtained differ, which again shows the system's sensitivity to the exact alignment, but the dependence on the injection laser attenuation ϵ is similar. We observe the most significant difference between using the reservoir output and using the reflections. Comparing the memory capacities obtained from the VCSELs' outputs, we observe a slightly increased MC for $\epsilon = 2$ dB. For $\epsilon = 6$ dB, the memory capacity is lower than for $\epsilon = 0$ dB.

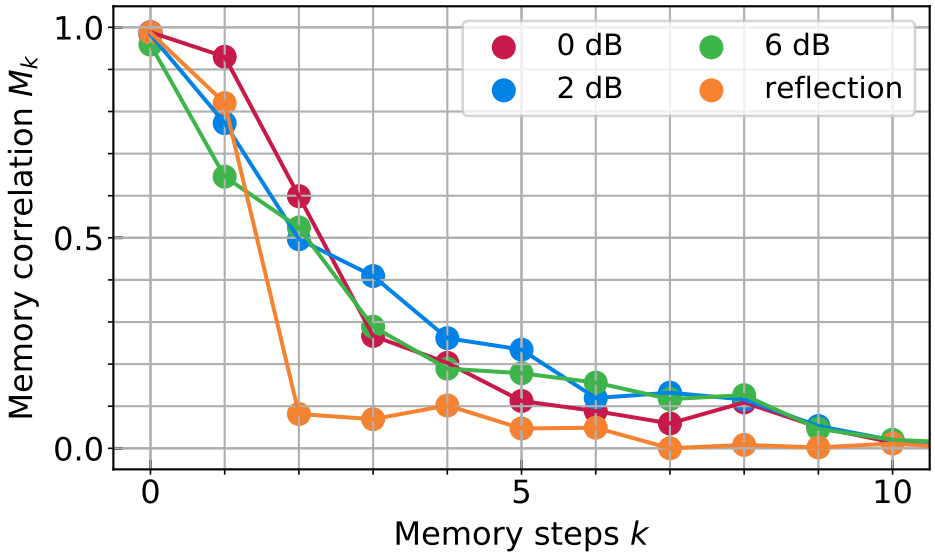

FIGURE 5.3: Memory correlation of the reservoir vs. number of time steps back k for different ϵ (attenuations of the injection laser) and when using the reflections at the VCSEL surfaces instead of the VCSELs' signals. Experimental conditions: $T_{\text{inj}} = 46.8°\text{C}$ and $\lambda \approx \lambda_{\text{match}}$ for all VCSELs.

TABLE 5.1: Memory capacities (MC) for different ϵ and for only the reflections at the VCSEL surfaces.

attenuation ϵ	0 dB	2 dB	6 dB	reflection only
MC (1st/2nd series)	3.41 / 3.22	3.58 / 3.29	3.23 / 2.62	2.17 / 2.15

To investigate further the role of the injection laser for the memory, we measured M_k and MC for different T_{inj} (and consequently different λ_{inj}) for $\epsilon = 0$ dB. The results are

summarized in Fig. 5.4 and Tab. 5.2. Again, there is a discrepancy between two supposedly identical measurements taken on different days, the one for $\epsilon = 0\,\mathrm{dB}$ in Fig. 5.3 and Tab. 5.1 and the one for $T_{\mathrm{inj}} = 46.8\,^{\circ}\mathrm{C}$ in Fig. 5.4 and Tab. 5.2. Consequently, we will concentrate on observed dependences by comparing results from the same measurement series. Here, we obtain the highest memory capacity for $T_{\mathrm{inj}} = 46.8\,^{\circ}\mathrm{C}$. The memory capacity decreases nearly symmetrically for deviations from this temperature. The memory correlations M_k show the same tendency. Still, there are differences, e.g. that $M_1(47.2\,^{\circ}\mathrm{C}) \approx M_1(46.7\,^{\circ}\mathrm{C}) > M_1(46.9\,^{\circ}\mathrm{C})$ or that M_2 or M_5 are highest at $46.9\,^{\circ}\mathrm{C}$. Fig. 5.4 suggests that the memory increases with the number of optically injection-locked VCSELs. However, for no condition we are able to lock all the VCSELs, because the locking measurements were carried out with an isolator instead of the MZM. Full injection locking of all the VCSELs might not be beneficial but we are unable to provide the experimental data to make a robust claim in this direction.

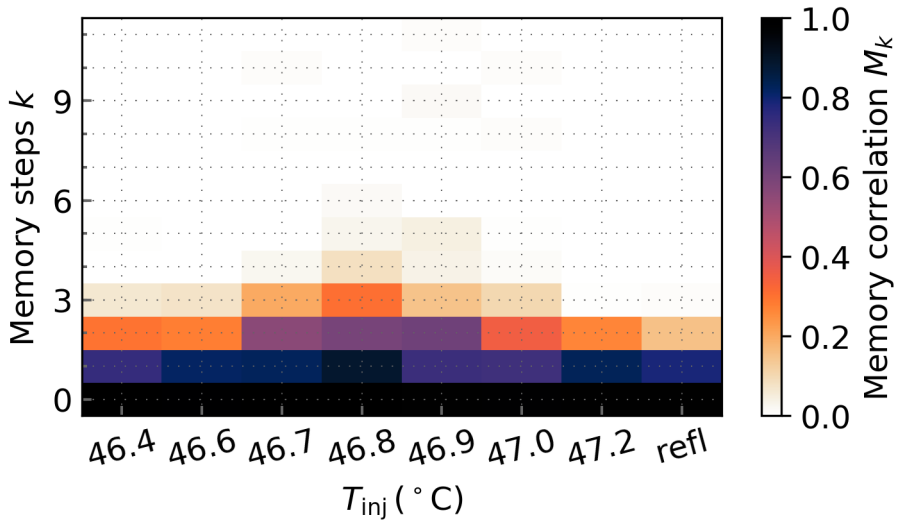

FIGURE 5.4: Memory correlation of the reservoir vs. number of time steps back k for different injection laser temperatures T_{inj} and for only the reflections at the VCSEL surfaces ("refl").

TABLE 5.2: Memory capacities for different injection laser temperatures and for only the reflections at the VCSEL surfaces.

T_{inj} (°C)	46.4	46.6	46.7	46.8	46.9	47.0	47.2	reflection
MC	2.11	2.17	2.61	2.88	2.59	2.19	2.09	1.95

5.2.2 Exclusive or (XOR) task

To further characterize the reservoir's performance, we let it compute the XOR task, which is frequently used as a benchmark task, since its version for 2 bits is one of the most basic nonlinear tasks. As opposed to the memory capacity task, the input consists of random bits instead of random numbers, still denoted by r_n. For k-bit XOR tasks, weights w_j are obtained by training with target values

$$y_n = \left(\sum_{n-k+1}^{n} r_n \right) \bmod 2. \tag{5.7}$$

This is equal to the XOR function of the last k bits (with the last one being the currently injected one) in a binary representation. For $k = 2$, an example target series for a given input is shown in Fig. 5.5.

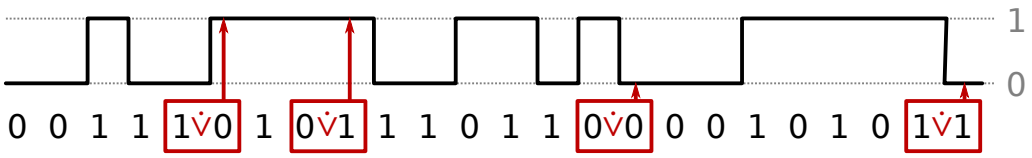

FIGURE 5.5: Example target values for the 2-bit XOR task for a given input (0s and 1s below).

Since only binary outputs make sense for this task, we round the output, which is then

$$a_n = \left\lfloor 0.5 + \sum_{j=1}^{J} w_j q_{n,j} \right\rfloor , \tag{5.8}$$

where the brackets represent the floor function, i.e. rounding down to the next-largest integer. Although in this way it is theoretically possible to obtain other values than zero and one, we did not observe this. We evaluate the reservoir performance via the error rate ER, defined by

$$\mathrm{ER} = \frac{1}{N} \sum_{n=1}^{N} ((a_n + y_n) \bmod 2). \tag{5.9}$$

In Tab. 5.3, the resulting error rates are listed. For both tasks, we obtain the best performance for $\epsilon = 0\,\mathrm{dB}$. This makes sense, since zero-step and one-step memory are essential for this task and both are highest for $\epsilon = 0\,\mathrm{dB}$. Notably, for the 2-bit XOR task, using the reflections as responses gives an error that is about seven times lower than random guessing, which is surprising for a nonlinear task. We are not sure whether the nonlinearity that is decisive for this performance occurs within the AWG, a non-ideal compensation of the MZM's nonlinearity, in the detection, or in the interaction of the injection laser with the switched-off VCSELs. For the 3-bit XOR task, the best performance that we observe is only about twice as good as random guessing.

TABLE 5.3: Error rates for the 2-bit and 3-bit XOR task at different experimental configurations.

attenuation ϵ	0 dB	2 dB	6 dB	10 dB	reflection only
ER 2-bit XOR (%)	1.5	2.8	15.8	25.8	7.0
ER 3-bit XOR (%)	26.2	35.9	40.0	46.2	38.5

To further analyze the lowest-error case ($\epsilon = 0\,\mathrm{dB}$), we count how often the wrong result has been obtained for a certain bit sequence. This is listed in Tab. 5.4. While for the 2-bit XOR task, we observe a slightly lower precision for the sequences ending in zero, for the 3-bit XOR task it is the other way round, with the difference in performance being much more significant. There, for sequences ending in zero, we still obtain ER = 7.0 % (about seven times better than random guessing), while for sequences ending in one, the error rate is about as good as random guessing with ER = 45.6 %. We observe better performance for sequences ending in zero for all the recorded data sets. To find the reason for this, we compared it to the 1-step-back 2-bit XOR task. There, the target value is the XOR function of the bits injected one and two steps before, i.e. $y_n = (r_{n-2} + r_{n-1}) \bmod 2$, as illustrated in Fig. 5.6. For this task, we obtain ER = 13.0 %. Interestingly, this also depends strongly on the currently injected bit, which in this case does not form part of

the classified bit sequence. When it is a zero, ER decreases to 4.6 %, while it increases to 21.5 % when the last bit is a one. An initial guess for the origin is that high injection power compromises the retrieval and transformation of the information.

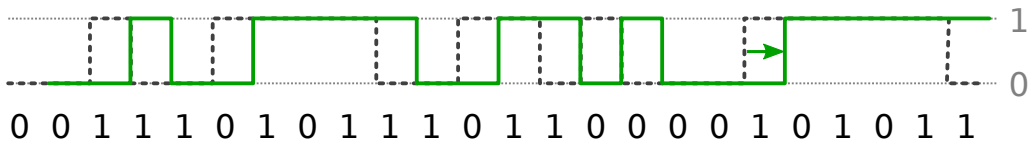

FIGURE 5.6: Example target values (solid green line) for the 1-step-back 2-bit XOR task compared to the simple 2-bit XOR task (dotted black line) for a given input (0s and 1s below).

TABLE 5.4: Error rates for the 2-bit and 3-bit XOR task by bit sequence.

bit sequence	00	01	10	11	000	001	010	011	100	101	110	111
ER (%)	2.0	0.8	2.4	0.8	5.5	40.0	5.4	58.3	9.6	38.7	7.5	45.7

5.2.3 Header recognition (HR)

The next task for which we trained the reservoir offline was header recognition (HR), another frequently used benchmark task. For k-bit HR, one chooses a target sequence X, consisting of k bits. We will denote the m^{th} bit of the target sequence X by x_m. The target reservoir output is

$$y_n(X) = \begin{cases} 1 \text{ if } r_{n-k+m} = x_m \ \ \forall m \in \mathbb{N} \cap [1;k] \\ 0 \text{ otherwise,} \end{cases} \tag{5.10}$$

so it is $y_n = 1$ if and only if the last k injected bits match the sequence X. An example for this is shown in Fig. 5.7. As in the XOR task, we round the output, i.e.

$$a_n = \left\lfloor 0.5 + \sum_{j=1}^{J} w_j q_{n,j} \right\rfloor \tag{5.11}$$

and compare it to the desired one to obtain the error rate for that bit sequence

$$\mathrm{ER}_X = \frac{1}{N} \sum_{n=1}^{N} ((a_n + y_n) \bmod 2). \tag{5.12}$$

We average the error rates for all 2^k possible k-bit sequences to calculate the overall error rate for k-bit HR. Note that in this task, the trivial guess $a_n = 0 \ \forall n$ yields an error rate of approximately $\mathrm{ER}_0 = 2^{-k}$ for a series of random bits. Therefore, we list the results we obtained for $k \in \{2;3;4\}$ in Tab. 5.5 in units of the respective ER_0. For all k, we obtain the best performance for $\epsilon = 0\,\mathrm{dB}$, recognizing every header correctly for $k = 2$. For $k = 3$, the error rate is still roughly 15 times lower than for the trivial guess, while for $k = 4$ it is not even twice lower. Interestingly, using only the reflection at the VCSEL surfaces yields comparable results to $\epsilon = 6\,\mathrm{dB}$ and better results than $\epsilon = 10\,\mathrm{dB}$.

For $\epsilon = 0\,\mathrm{dB}$, the error rates per 3-bit sequence are listed in Tab. 5.6 and per 4-bit sequence in Tab. 5.7. As for the XOR task, the error rate varies with the last bit of the sequence. For 3-bit HR, $\mathrm{ER}/\mathrm{ER}_0 = 0.002$ for sequences ending in zero and $\mathrm{ER}/\mathrm{ER}_0 =$

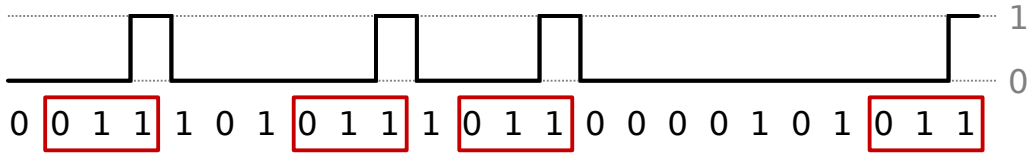

FIGURE 5.7: Example target values (black line) for the 3-bit HR task for a given input (0s and 1s below) and for the target sequence $X = 011$ (occurrences marked in red).

TABLE 5.5: Error rates (ER) for the 2-bit, 3-bit and 4-bit header recognition (HR) task at different experimental configurations in units of ER_0 (the error rate for the trivial guess).

attenuation ϵ	0 dB	2 dB	6 dB	10 dB	reflection only
2-bit header ER/ER_0	0.000	0.008	0.046	0.150	0.051
3-bit header ER/ER_0	0.068	0.167	0.439	0.617	0.449
4-bit header ER/ER_0	0.561	0.696	0.958	0.985	0.926

0.134 for sequences ending in one. For 4-bit HR, $ER/ER_0 = 0.282$ for sequences ending in zero and $ER/ER_0 = 0.840$ for sequences ending in one.

TABLE 5.6: Error rates (ER) for the 3-bit HR task by bit sequence in units ER_0 (the error rate for the trivial guess).

sequence X	000	001	010	011	100	101	110	111
ER_X/ER_0	0.000	0.048	0.000	0.320	0.000	0.056	0.008	0.112

TABLE 5.7: Error rates (ER) for the 4-bit HR task by bit sequence in units of ER_0 (the error rate for the trivial guess).

sequence X	0000	0001	0010	0011	0100	0101	0110	0111
ER_X/ER_0	0.112	0.896	0.080	0.736	0.224	0.752	0.208	0.928
sequence X	1000	1001	1010	1011	1100	1101	1110	1111
ER_X/ER_0	0.432	0.896	0.288	0.928	0.560	0.880	0.352	0.704

5.2.4 Digital-to-analog conversion (DAC)

Our final benchmark task is k-bit digital-to-analog conversion (DAC), where the goal is to map the 2^k different bit sequences to the interval $[0;1]$ with equal spacing between them. The target output can be defined in two ways, depending on which bit is the most significant bit (MSB). If we define the first bit of the sequence as the MSB, the target output of the reservoir is

$$y_n = \sum_{m=1}^{k} \frac{2^{k-m} r_{n-k+m}}{2^k - 1}, \tag{5.13}$$

as illustrated in Fig. 5.8 a) for $k = 2$ with an example sequence. If we define the last bit of the sequence as the MSB, the target output of the reservoir is

$$y_n = \sum_{m=1}^{k} \frac{2^{m-1} r_{n-k+m}}{2^k - 1}, \tag{5.14}$$

as illustrated in Fig. 5.8 b) for $k = 2$ with the same example sequence. Since no rounding is required here, the reservoir output is

$$a_n = \sum_{j=1}^{J} w_j q_{n,j}. \tag{5.15}$$

To evaluate the performance of the reservoir, we calculated the normalized root mean square error (NRMSE) in both cases as

$$\mathrm{NRMSE} = \sqrt{\frac{1}{N} \sum_{n=1}^{N} (a_n - y_n)^2}. \tag{5.16}$$

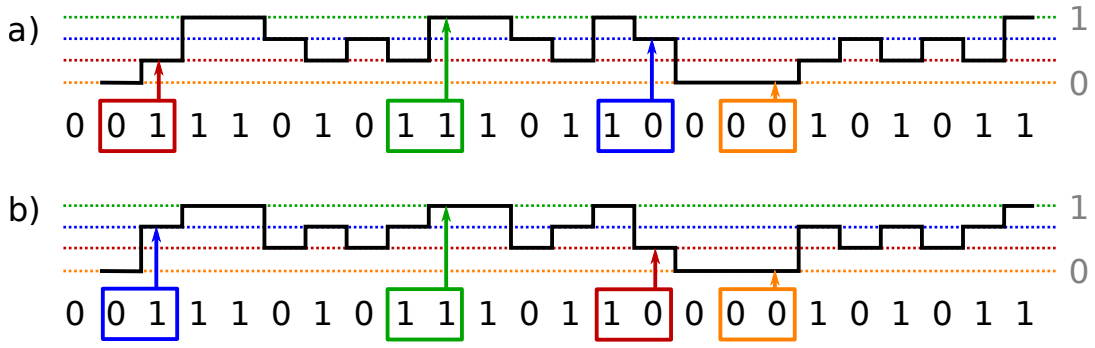

FIGURE 5.8: Example target values (black line) for the 2-bit DAC task for a given input (0s and 1s below). The different 2-bit sequences are mapped to equally spaced values between 0 and 1. a) The first bit is the most significant bit (MSB). b) The last bit is the MSB.

First, we analyze the version of this task in which the last bit of the sequence is the MSB. In Tab. 5.8, the results for 1- to 6-bit DAC are given for $\epsilon = 0\,\mathrm{dB}$. As confirmed by these results, in this case, the difficulty of this task does not increase significantly with k, since the target output for k is an approximation of the target output for $k+1$. Moreover, we calculate the NRMSE using the reservoir output a_n obtained for $k = 4$ and the target output y_n obtained for $k = 6$. This yields an error of NRMSE = 0.044, which corroborates our statement. Thus, throughout this thesis, we base our analysis on the other version of this task.

TABLE 5.8: Normalized root mean square error (NRMSE) for 1- to 6-bit digital-to-analog conversion (DAC) for $\epsilon = 0\,\mathrm{dB}$ when the last bit is the MSB.

k	1	2	3	4	5	6
k-bit DAC NRMSE	0.031	0.034	0.040	0.042	0.042	0.041

DAC with the first bit as the MSB is highly memory-related and its difficulty increases rapidly with k. The challenge for the reservoir is to give the highest weight to the bit that was injected the longest ago without neglecting the more recently injected bits. In Tab. 5.9, the NRMSE is given for different k and for different experimental configurations for the first bit being the MSB. For comparison, we give the NRMSE that would result from trivially guessing $a_n = 0.5\ \forall n$. For the simple 1-bit DAC, which is just a reconstruction of the current bit, we obtain nearly equal performances for $\epsilon = 0\,\mathrm{dB}$ and for the reflections. For 2-bit DAC, $\epsilon = 0\,\mathrm{dB}$ gives the lowest error, while for 3- and 4-bit DAC, $\epsilon = 0\,\mathrm{dB}$ and $\epsilon = 2\,\mathrm{dB}$ yield similar performances. For $\epsilon = 0\,\mathrm{dB}$, we observe a major decrease in performance upon increasing k from one to three. For $k = 1$, the NRMSE is 16 times lower than the trivial guess, for $k = 2$, it is still 5.5 times lower, while for $k = 3$ it is only 2.1 times lower.

TABLE 5.9: Normalized root mean square error (NRMSE) for 1- to 4-bit digital-to-analog conversion (DAC) for different experimental configurations and the trivial guess of constant 0.5 with the first bit being the MSB.

attenuation ϵ	0 dB	2 dB	6 dB	10 dB	reflection only	trivial guess
1-bit DAC NRMSE	0.031	0.053	0.083	0.132	0.032	0.500
2-bit DAC NRMSE	0.065	0.095	0.140	0.175	0.123	0.373
3-bit DAC NRMSE	0.152	0.149	0.210	0.190	0.225	0.329
4-bit DAC NRMSE	0.212	0.222	0.247	0.250	0.264	0.310

In Fig. 5.9, the results of 2- and 3-bit DAC are visually compared by plotting the reservoir output a_n against the target output y_n. We clearly observe how for $k = 2$ the average output for a certain target value (the point in the middle of the two error bars) is much closer to its respective target output than for $k = 3$. Also, the standard deviations of the reservoir outputs – shown by the error bars – are about twice lower for $k = 2$. Finally, for $k = 2$, the linear fit to a_n is close to the ideal result, while for $k = 3$ it deviates clearly.

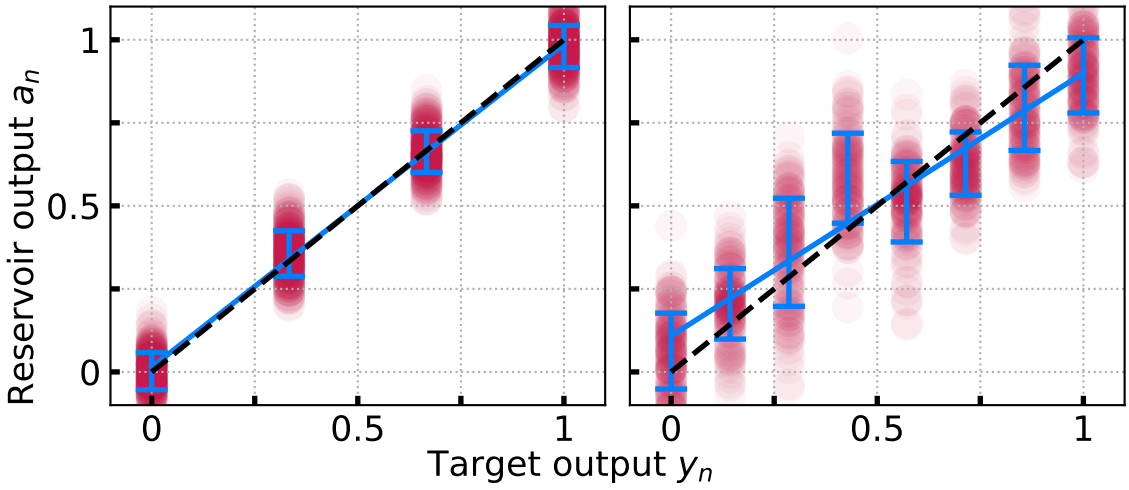

FIGURE 5.9: 2- and 3-bit digital-to-analog conversion (DAC) with the first bit being the MSB. Red scatter plot: a_n vs. y_n; blue line plot: linear fit to a_n; black dashed line: ideal result. The blue error bars are centered around the average output for the respective target value and indicate the standard deviation. Results for $\epsilon = 0\,\mathrm{dB}$.

5.3 Role of output nodes

In this section, we investigate how connecting different sets of reservoir nodes to the output layer can influence the computing performance. Connecting a node to the output layer means using the corresponding VCSEL's signal for training and testing. Note that nodes that are not connected to the output layer can still contribute indirectly to the performance, since they form part of the reservoir's dynamics and can thus enhance dimensionality. While we find that it is important which nodes are connected to the output layer, we could not correlate the performance increase with measures of the signals that we recorded for the corresponding VCSELs.

5.3.1 Reservoir performance for different output configurations

Carrying out several algorithmic analyses, we find that not only the number of VCSELs connected to the output layer has an impact on the reservoir performance, but that the exact set of VCSELs is of crucial importance. We obtained these results carrying out the following analyses separately for all the different tasks. One algorithm started with the full set of $J = 23$ nodes/VCSELs and calculated the respective performance indicator Z ($Z \in \{\mathrm{MC}; \mathrm{ER}; \mathrm{ER}/\mathrm{ER}_0; \mathrm{NRMSE}\}$). Then, it calculated Z for every possible set containing $J = 22$ nodes and selected the set for which Z was highest. In the next step, it calculated Z for every possible 21-node-subset thereof and selected the one giving the highest Z. It continued removing nodes in this manner until only one node was left. We ran the same algorithm aiming for the lowest Z instead of the highest.

Additionally, we ran another algorithm that started with the single node that, as a single-node output layer, yielded the highest Z. Then, it checked which 2-node output layer containing that node gave the highest Z. It continued by always adding that node to the J-node output layer that would result in the highest Z of the $J+1$-node output layer. We ran the same algorithm aiming for the lowest Z.

For most J, these algorithms do not guarantee finding the set of nodes for which Z is highest or lowest, but they are 19 orders of magnitude faster than an exhaustive search. The resulting $Z(J)$ are visualized in Fig. 5.10. We set the performance of the empty output

layer to MC = 0 for the memory task, ER = 50 % for the XOR task, $ER/ER_0 = 1$ for header recognition, and NRMSE = 0.373 for 2-bit DAC (NRMSE for the trivial guess). The data for MC was obtained with $\epsilon = 2$ dB, the rest of the data with $\epsilon = 0$ dB. For most J, the algorithm that removed nodes from the output layer produced similar or even equal results to the algorithm that added nodes. Since, at the same time, for most J, there is a significant difference in Z between the minimizing and maximizing algorithms, we can conclude that the reservoir performance does not only depend on J, but also crucially on the exact set of nodes used to create the output.

For example, for the memory capacity, it is possible to obtain MC = 3.00 with $J = 8$ or with $J = 20$, depending on which nodes are used. For $J = 19$, we can obtain MC = 3.58 as for $J = 23$, while with $J = 14$, MC = 3.48 is possible, a reduction of less than 3 % while using only 3/5 of the nodes for output. Surprisingly, for the 2-bit XOR task, ER is lower for $10 \leq J \leq 22$ than for the full set of $J = 23$ nodes. We obtain the lowest ER = 0.8 % for 17 or 18 nodes. To check if this could be optimized further, we computed ER for all possible 18-node output layers. Still, the lowest value that we found was ER = 0.8 %. When running the adding and the removing algorithms for the 3-bit XOR task, we found the best performance ER = 25.0 % for $J = 19$ nodes, which means a much less significant improvement upon removing nodes than for the 2-bit XOR task. For the 3-bit HR task, we again obtain the lowest error for $J < 23$, in this case $ER/ER_0 = 0.057$ for $J = 20$. For the 2-bit DAC task, we observe the strongest dependence on the exact set of nodes used to create the output. Here, it is possible to obtain a lower NRMSE with 2 well-chosen nodes than with 18 poorly chosen ones. Similar to the other cases, we obtain the lowest error for $J < 23$, although the difference is minimal in this case, with NRMSE = 0.067 for $J = 18$ and NRMSE = 0.068 for $J = 23$. Analyzing data sets recorded under similar conditions, we obtained similar results. Note that this includes the case in which only the reflections on the VCSEL surfaces were used.

We further analyzed the data shown in the top left plot of Fig. 5.10 by visualizing the M_k that make up $MC = \sum_{k=0}^{9} M_k$. In Fig. 5.11, the corresponding M_k are plotted for different J and for the different algorithms. In the top plots, the data sets for adding nodes are represented, in the bottom plots the data sets for removing nodes. For the data shown on the left, the algorithm aimed for high memory capacity, while for the data shown on the right, it aimed for low memory capacity. We notice that, for the high-MC-plots, $MC \approx 1$ for $J = 1$ is mostly due to $M_0 \approx 1$. However, in the top right plot, we observe that for $J = 17$, we can obtain $M_0 \approx 0.7$. In the high-MC-plots, we also observe that for $J > 17$, M_k does not change significantly for most k and that for most J, M_k decreases with increasing k. In the plots on the right, we find an explanation for the different MCs obtained with the low-MC-algorithms for some J. The algorithm that removes nodes was stuck in a local minimum with high M_0, while the one adding did not add nodes that lead to high M_0 until high J.

5.3.2 Contribution of individual nodes

The next goal was to find out, which individual nodes in the output layer contributed how much to the reservoir performance. Although we find weak tendencies, like the VCSELs in the 5th column contributing less to the performance and direct neighbours of the central VCSEL tending to contribute more, the results are little consistent, and we cannot make strong general statements. Surprisingly, even the signal-to-noise ratio (SNR) is only a weak indicator of how much adding a node to the output layer improves the computation performance. For our investigations, we ran the following algorithm. One node is randomly chosen, and the performance indicator Z ($Z \in \{MC, ER, ER/ER_0, NRMSE\}$) is computed with only this node in the output layer. Then, another random node is added,

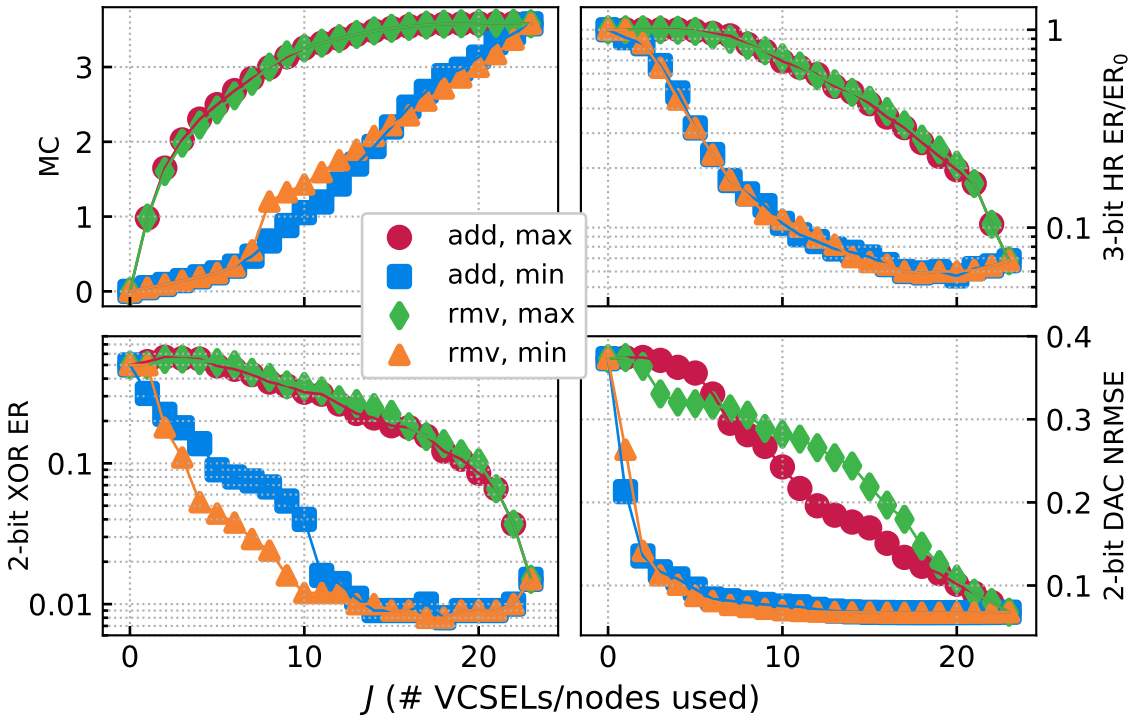

FIGURE 5.10: Memory capacity at $\epsilon = 2$ dB; XOR ER, HR ER/ER$_0$, and DAC NRMSE at $\epsilon = 0$ dB for different numbers of nodes J when adding (in the legend denoted by "add") or removing ("rmv") nodes to or from the output layer such that the new reservoir output results in the highest ("max") or lowest ("min") MC, ER or NRMSE. Lines are guides to the eye. For a more detailed description of the algorithm used for adding and removing nodes, see text.

and Z is computed again. This is done at every step until all 23 nodes are used to create the output. After that, the algorithm starts again with one node and repeats this process 5000 times in total. To obtain the average contribution of one node, we calculate the average change of Z upon addition of that node, where, again, we set the performance of the empty output layer to MC $= 0$ for the memory task, ER $= 50\,\%$ for the XOR task, ER/ER$_0$ $= 1$ for header recognition, and NRMSE $= 0.373$ for 2-bit DAC. For the memory, this data is shown in Fig. 5.12. Here, the average increase of every M_k is shown, too. The positions of the line and scatter plots correspond to the positions of the VCSELs in the array, so e.g. the 4th plot from the left and 2nd from the top corresponds to VCSEL (4,2). The background color and the number in the top right corner show the average increase of MC upon connecting this VCSEL to the output layer. The scatter plots visualize the average increase of M_k when this VCSEL was added versus the step k. We observe that especially the VCSELs in column 5 show nearly no direct contribution to the memory. Considering their low signal strength (compare to VCSEL (5,2) in Fig. 4.16), this is expected. In general, VCSELs that are closer to the central VCSEL and further left tend to contribute more to the memory. Although these are generally also the VCSELs for whose signals we measured a better SNR, both quantities are not strongly correlated, as we show in the next paragraphs.

In Figs. 5.13 and 5.14, results obtained with the same algorithm but for different tasks are shown. We observe that for different tasks or just different ϵ, the contributions of individual nodes vary. Further analysis (not shown) shows that this even varies between measurements recorded under the same experimental conditions. Still, there is a general

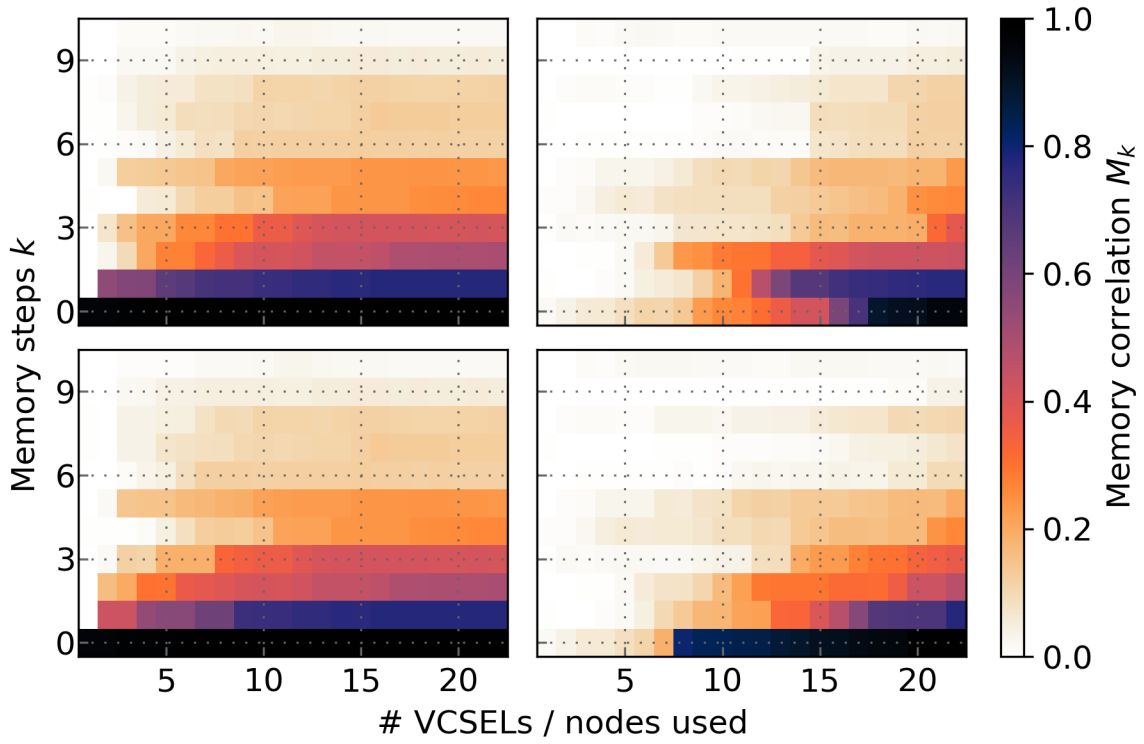

FIGURE 5.11: Memory correlations M_k at $\epsilon = 2\,\text{dB}$ and $T_{\text{inj}} = 46.8\,^{\circ}\text{C}$ for different numbers J of output nodes using different algorithms for adding (starting at $J = 0$) or removing (starting at $J = 23$) nodes to or from the output layer (see text and Fig. 5.10). Top left: adding nodes, aiming for high MC. Top right: adding nodes, aiming for low MC. Bottom left: removing nodes, aiming for high MC. Bottom right: removing nodes, aiming for low MC.

trend that the VCSELs in the 5th column contribute least to the performance, while the neighbours of the central VCSEL and VCSELs (3,5) and (1,1) contribute most. Other than that, we do not find any common tendencies for all the data sets and tasks. Note that, to exclude random fluctuations, we repeated the algorithm for some data sets and found that it reproduced the result with an average deviation of $< 1\%$.

To evaluate more rigorously if there are nodes whose connection to the output layer is generally more important for computing, we calculate the Pearson correlation ρ for data pairs that, for each VCSEL, consist of the average de- or increase of the performance indicators Z that we obtained with the above-described algorithm for two different tasks. These corresponding data are listed in Tab. 5.10. We find that, on average, how important one output node is for a particular task, is not a strong indicator for how important it is for another task. Note that we observe these low correlations even though, for each ϵ, the XOR task, the HR task, and the DAC task were evaluated for the same data set.

We also calculate the correlations of the nodes' contributions to the MC task at different configurations. The results are given in Tab. 5.11. We observe that even these values do not correlate strongly, with $0.54 < \rho < 0.74$.

To conclude this analysis, we want to determine if the properties of the dynamic response of the VCSELs (s. Tab. 4.3) correlate with the performance at the RC tasks. For this, we calculate the correlation between the performance in- or decrease upon connecting that node to the output layer and the properties of the dynamical response at the most similar conditions. Those properties are the Pearson correlation of the injected bit and the response (a measure for the linearity of the response), a measure for non-linearity (y_{NL})

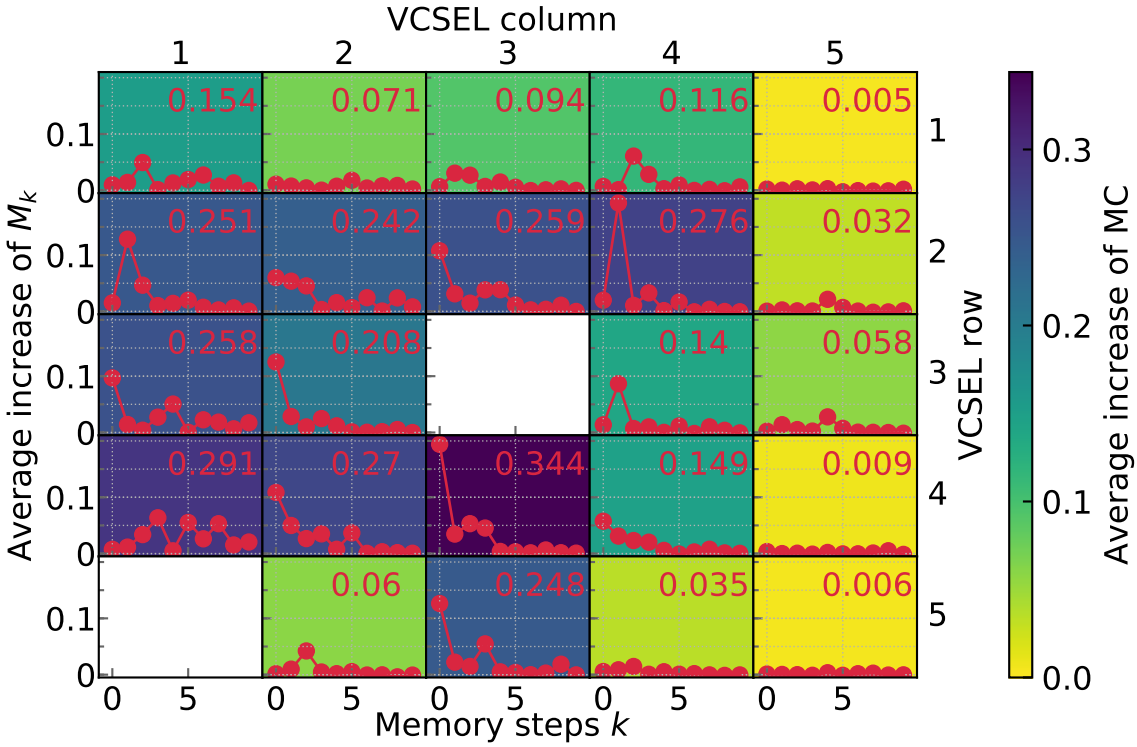

FIGURE 5.12: Average increase of MC upon connecting the respective node to the output layer. The values were averaged over 5000 runs, each starting at $J = 0$ and ending at $J = 23$, while measuring MC and M_k at every step. The plot position corresponds to the position of the VCSEL in the array. The number and the background color visualize the average increase of MC when connecting the VCSEL to the output layer, and the scatter plots show the increase of the different M_k. Experimental conditions: $\epsilon = 2\,\mathrm{dB}$, $T_{\mathrm{inj}} = 46.8\,^{\circ}\mathrm{C}$.

that is defined in Eq. 4.14, the D'Agostino p value (a measure for how much the response resembles random noise), and the SNR. The properties were introduced in Subsec. 4.4.2. The correlations between the performance and the properties are listed in Tab. 5.12. We observe that for most tasks, a high D'Agostino p value is not favourable, although the correlation is weak. A mostly linear response of a node correlates weakly with a high contribution to the performance. However, our aim is not to create a linear reservoir. Besides, when using the most linear response that we have, the reflections, the performance was worse than with less linear responses. We therefore conclude that in our case linearly responding nodes contribute much to the performance as they are not abundantly available inside the VCSEL reservoir. Finally, a high y_{NL} correlated slightly positively with the performance in- or decrease in all cases. This can have several reasons. The most obvious one is that RC requires nonlinearity. Surprisingly, even the SNR does not correlate strongly with how much a node adds to the reservoir performance. This is an especially curious result considering that the SNR is of the order of 1 in many cases.

Summarizing, none of the analyses in this subsection enables us to reliably identify the best output nodes for RC. Thus, it is difficult to predict how the reservoir performance could be improved.

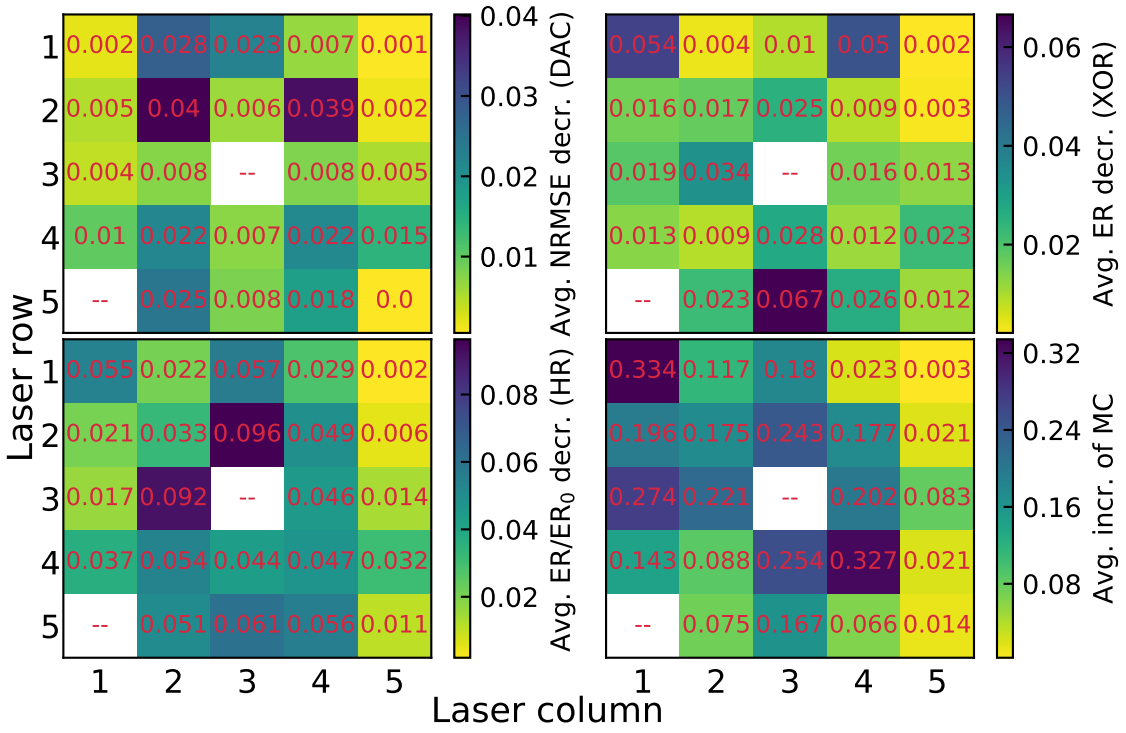

FIGURE 5.13: Average change in RC performance upon connecting different nodes to the output layer at $\epsilon = 0$ dB. The nodes were added in random order. The shown results are averages of 5000 runs.

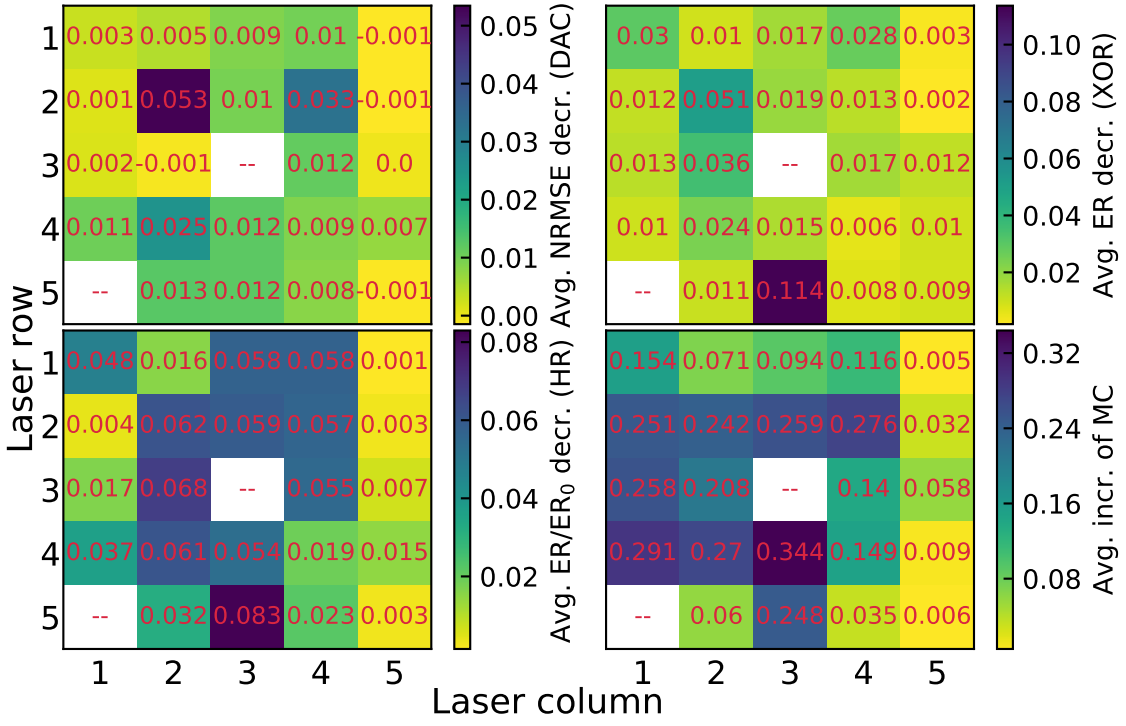

FIGURE 5.14: Average change in RC performance upon connecting different nodes to the output layer at $\epsilon = 2$ dB. The nodes were added in random order. The shown results are averages of 5000 runs.

TABLE 5.10: Pearson correlation ρ of the contribution of different output nodes to the performance at $\epsilon = 0\,\mathrm{dB}$ (top) and at $\epsilon = 2\,\mathrm{dB}$ (bottom).

$\epsilon = 0\,\mathrm{dB}$	MC	2-bit XOR ER	3-bit HR ER/ER$_0$	2-bit DAC NRMSE
MC	1	0.259	0.489	0.062
2-bit XOR ER	0.259	1	0.439	-0.253
3-bit HR ER/ER$_0$	0.489	0.439	1	0.193
2-bit DAC NRMSE	0.062	-0.253	0.193	1
$\epsilon = 2\,\mathrm{dB}$	MC	2-bit XOR ER	3-bit HR ER/ER$_0$	2-bit DAC NRMSE
MC	1	0.359	0.594	0.443
2-bit XOR ER	0.359	1	0.673	0.317
3-bit HR ER/ER$_0$	0.594	0.673	1	0.533
2-bit DAC NRMSE	0.443	0.317	0.533	1

TABLE 5.11: Pearson correlation ρ of contribution of nodes to MCs at different conditions.

ρ	$\epsilon = 0\,\mathrm{dB}$	$\epsilon = 2\,\mathrm{dB}$	reflections
$\epsilon = 0\,\mathrm{dB}$	1	0.640	0.543
$\epsilon = 2\,\mathrm{dB}$	0.640	1	0.735
reflections	0.543	0.735	1

TABLE 5.12: Pearson correlation ρ of contribution of nodes to performance at different tasks and dynamical properties of the recorded time trace at $\epsilon = 0\,\mathrm{dB}$ (top) and at $\epsilon = 2\,\mathrm{dB}$ (bottom). Note that there are two Pearson correlations here, the one of the dynamical responses with the input and the one correlating the responses of the nodes to the contribution to the performance.

$\epsilon = 0\,\mathrm{dB}$	MC	2-bit XOR ER	3-bit HR ER/ER$_0$	2-bit DAC NRMSE
Pearson	0.656	-0.094	0.512	0.039
y_{NL}	0.306	0.036	0.571	0.306
D'Ago	-0.347	0.111	-0.306	-0.146
SNR	0.400	0.127	0.455	-0.093
$\epsilon = 2\,\mathrm{dB}$	MC	2-bit XOR ER	3-bit HR ER/ER$_0$	2-bit DAC NRMSE
Pearson	0.739	0.484	0.536	0.258
y_{NL}	0.733	0.437	0.676	0.583
D'Ago	-0.578	-0.322	-0.328	-0.265
SNR	0.715	0.348	0.591	0.153

5.4 Summary and conclusion

In this chapter, we have introduced our concept for RC with VCSEL arrays. In short, the VCSELs serve as nodes, the injection laser as an input layer and the recurrent connections between the nodes as well as the connections from the input to the reservoir are established via diffraction in the external cavity. The output is recorded separately for each node, and the training is carried out offline on a conventional computer.

We have evaluated the performance of the reservoir with different benchmark tasks like the memory capacity (MC), the XOR task, header recognition (HR) and digital-to-analog conversion (DAC). We obtain memory capacities of up to 3.6. The absolute value depends on the particular measurement conditions and the alignment, but it is low enough to consider classifying the VCSEL RC system as an extreme learning machine [99]. It is highest for good spectral alignment of injection laser and VCSELs and for slightly attenuating the injection laser. For the other three tasks (XOR, HR, and DAC), we obtain the best performances when not attenuating the injection laser. For the 2-bit XOR task, we obtain error rates below 1 %, while for the 3-bit XOR task the best performance is an error rate of ¼ with the error being lower when the last bit of the analyzed sequence is a zero. We obtain error-free 2-bit HR, while for 3-bit HR the best performance we observe is about 18 times better than random guessing. For three bits and for four bits, the accuracy of classification depends highly on the last bit of the sequence, with lower errors if it is a zero. For the 2-bit DAC task, we obtain a minimal NRMSE of 0.065. Here, the error stems mainly from symmetric deviations around an average close to the target value, while for 3-bit or 4-bit DAC, not only the standard deviations between all the outputs with an identical target value are larger, but also the averages of these outputs deviate significantly from the target. Our results for the 2-bit XOR, 2-bit HR and 2-bit DAC tasks are comparable to the ones obtained in Ref. [67]. We use one fifth of the nodes used there, but in our case the training is performed offline with real-valued weights, while in Ref. [67] it is implemented online with Boolean weights.

Further analysis suggests that in most cases connecting about 18 VCSELs to the output layer is optimal and that some nodes' outputs hardly contribute to the computing performance. We could not identify reliable indicators to predict which properties of the recorded responses of some VCSELs make them more valuable for certain computations. Since we obtained the best RC benchmark performances when not attenuating the injection laser and when maximally spectrally aligning it to the VCSELs, a stronger injection laser signal might improve the performance. Finally, considering the low SNR that we measure in the VCSELs' responses, there is probably room for improvement in an approach with further optimized alignment and optical elements, like for example in an integrated system.

Chapter 6

Conclusion and outlook

In this thesis, we experimentally investigated the diffractive coupling and injection locking of vertical-cavity surface-emitting lasers (VCSELs) in large arrays and implemented a reservoir computer based on this system. With our experiments, we have explored a scalable approach for coupling tens or potentially hundreds of lasers. Our results are relevant for fundamental research, since they enable us to experimentally study the dynamics of a real-world complex network. Moreover, with our approach, we investigate a system that bears the potential for a fully hardware-implemented and parallel photonic neural network.

First, we thoroughly characterized the individual VCSELs. Then, we investigated their spectral and dynamical behaviour under optical injection and pairwise coupling, as well as when coupling the entire array. Finally, we introduced a concept for reservoir computing (RC) using VCSEL arrays, implemented it experimentally, and tested the system on four basic benchmark tasks.

The experiments in this thesis were carried out with custom-manufactured GaInAs quantum well VCSELs that are arranged in 5×5 square lattice arrays with a pitch of about 80 µm. The VCSELs' apertures are slightly elliptic for polarization control, and every VCSEL is individually electrically contacted and thus individually addressable via its bias current. Most results were obtained with one main array, which contained three pairs of short-circuited VCSELs. For only a few experiments, we used a different array. By using a microscope objective, a diffractive optical element (DOE), a lens, and a mirror, the VCSELs were diffractively coupled and subjected to feedback. This scheme allows for bidirectional coupling of nearest and second-nearest neighboring VCSELs as well as for simultaneous optical injection into all 25 VCSELs of an array, using an external DBR laser. For some experiments, the DBR laser's intensity was modulated using an arbitrary waveform generator in combination with a Mach-Zehnder modulator. Most of the experimental data were recorded by fiber-coupling the VCSELs' outputs and feeding an optical spectrum analyzer (OSA) or a photodiode, whose output was fed into an electrical spectrum analyzer or an oscilloscope.

We began our experiments by characterizing the individual VCSELs, and find that they behave homogeneously regarding their I-U and P-I characteristics, with an average threshold current $I_{\mathrm{th}} = 0.364\,\mathrm{mA}$ and an average slope efficiency of $0.244\,\mu\mathrm{W}/\mu\mathrm{A}$. For currents $I \leq 2I_{\mathrm{th}}$, all VCSELs emit single-mode with a side-mode suppression ratio of at least 15 dB. The ground mode is a 0th order LP_{01} single-lobed mode with circular symmetry, which has an FWHM of about 4.5 µm. For 22 out of 25 VCSELs, this ground mode is linearly polarized along the major axis of the elliptic aperture. When subjecting the central VCSEL of the main array to feedback, its threshold current is reduced by up to 3.5 %. Moreover, with feedback, we observed external cavity modes and a redshift, from which we estimated a feedback strength of $36\,\mathrm{ns}^{-1} \leq \kappa \leq 62\,\mathrm{ns}^{-1}$ for $2 \leq \alpha \leq 5$, where α is the linewidth enhancement factor.

After the fundamental characterization of the individual VCSELs, we investigated how the VCSELs reacted to coupling and optical injection. First, we investigated pairwise

coupling of the central VCSEL with every other individual VCSEL (or short-circuited VCSEL pair). For all the investigated pairwise coupling configurations, we find signatures for successful coupling in the RF spectra of the central VCSEL. Furthermore, we observe mutual optical locking of the central VCSEL with 14 of 21 individual non-central VCSELs (or VCSEL pairs). Next, we investigated the optical coupling of the entire array. Upon increasing the common wavelength of all the non-central VCSELs and thus increasing their detuning from the central VCSEL, we observe a clear transition that occurs simultaneously in both the optical and the RF spectra of the central VCSEL. We interpret this as a transition from optical locking of the entire array to unlocking. For every individual VCSEL, we observe optical injection locking to an external DBR laser, and we achieve simultaneous optical injection locking for all 21 independently tunable VCSELs. From the spectral widths of the locking regions, we estimate coupling coefficients of $13\,\mathrm{ns}^{-1} < k_c < 35\,\mathrm{ns}^{-1}$ for $2 \leq \alpha \leq 5$. The amounts obtained for optical injection are slightly higher than the ones for coupling, and both are comparable to values from earlier experiments with similar arrays [9] and to values obtained in fiber-based injection experiments with VCSELs emitting at 1550 nm [88].

In the next step, we investigated the dynamic response of the VCSELs to modulating the intensity of the injection laser according to a series of 1000 pseudo-random numbers. We modulated the injected signal at 454.54545 MHz, which gives us 11 sampling points per injected value, when detecting the VCSELs' outputs at 5 GS/s, and which also equals the external cavity frequency. To increase the signal-to-noise ratio (SNR) of the recorded VCSEL signals, for every output point, we averaged over 1024 modulation periods and over nine consecutive sampling points, while discarding two samples for transition. To characterize the VCSELs' responses, we analyzed the dependence of the above-described averaged output signals on the injected pseudo-random numbers. For some VCSELs, their averaged output is hardly affected by the modulation of the injected signal. For others, we observe different types of nonlinear dependences, and some VCSELs' response depends consistently close-to-linearly on the modulated injection. However, for most VCSELs, their response is not reliably reproducible.

Having experimentally verified injection locking and diffractive coupling of the VCSELs, we implemented RC experimentally and tested the system on basic benchmark tasks. For this, our experimental scheme served as a reservoir computer. A reservoir computer typically consists of an input layer with fixed connections to the reservoir, which in turn is composed of nodes with fixed recurrent connections between them. The only connections that are modified to train the system are the output weights. In our experimental setup, the VCSELs serve as reservoir nodes, the information input occurs via the injection laser, and both the recurrent connections between the nodes and the connections from the input to the reservoir are established via diffraction in the external cavity. The output is recorded separately for every node, and the training is carried out offline via ridge regression on a conventional computer. To evaluate the performance of the reservoir, we tested it on four basic benchmark tasks: the memory capacity (MC) task, the exclusive or (XOR) task, header recognition (HR), and digital-to-analog conversion (DAC). The maximal MC that we obtain is 3.6, and it is highest when the injection laser is spectrally aligned to the VCSELs and attenuated by 2 dB. Stronger attenuation lowers the MC. We obtain minimal errors of 1 % for the 2-bit XOR task, error-free 2-bit HR, and a minimal NRMSE of 0.065 for 2-bit DAC with the first bit as the most significant bit. Analyzing also the 3-bit versions of these tasks, we recognize trends that are similar for all or most of the tasks. In all tasks, the performance of the reservoir was highly dependent on the particular nodes that were connected to the output layer, and not only on the number of nodes. It usually improved upon disconnecting up to five nodes from the output layer, thus only using 18 instead of 23 nodes, as long as these nodes were chosen well. From

properties of the corresponding VCSEL's signal, we can not reliably predict how much the computing performance will change upon connecting a reservoir node to the output layer, although we find a slight correlation of this change with the SNR of the nodes' measured signals. When the input consists of bits – which is the case for the XOR task, HR, and DAC – the reservoir performance is generally better when the currently injected bit is a zero than when it is a one. An initial guess for the reason for this is that high injection power compromises the retrieval and transformation of the information. For XOR, HR, and DAC, we obtain the best performances when not attenuating the injection laser.

Based on our results, we suggest several options how to modify the experiment or to extend these investigations in the future. First, an injection laser providing higher output power would allow for exploring a wider parameter space. Since the best RC performance was obtained when not attenuating the injection, it might be further improved by using a stronger injection signal. Another interesting option is combining the current RC scheme with a feedback-based approach by converting every physical node into various virtual nodes along the delay line, which would increase the number of reservoir nodes and thus boost the available phase-space dimension. Additionally, it would be interesting to explore the information processing capabilities of larger arrays. The number of electrically pumped VCSELs in an array is limited, because contacting the inner VCSELs becomes increasingly difficult when adding emitters to the array. However, with optically pumped quantum-dot micropillar lasers (QDMPLs), larger arrays can be implemented [100], although here one faces new challenges. QDMPLs have to be operated at cryogenic temperatures, and not every QDMPL is tunable independently of the others. For all these approaches, the main obstacle that has to be overcome is the low detection SNR. One way to increase both detection SNR and injection signal up to four-fold, is replacing the central beamsplitter by a polarizing beamsplitter (PBS) and introducing a $\lambda/4$-waveplate between this PBS and the mirror, while placing the DOE between the array and the PBS. However, in that case, one would always have a tradeoff of detection SNR and coupling strength between VCSELs. Also, additional aberrations would be introduced, since there are more optical elements between DOE and mirror, and the external laser would only inject into the central 3×3-array of VCSELs. In all the mentioned schemes, an attractive approach is using spatial-light modulators (SLMs) to implement different output weights experimentally and thus cut the need for recording the VCSELs' responses separately. With this hardware-implemented output layer, the SNR would be improved by adding up the signals of different VCSELs, whose noise is uncorrelated. Furthermore, an SLM could replace the cavity mirror and thus enable reconfiguration of the coupling to a certain degree.

In summary, we have successfully coupled and injection-locked a network of 25 VCSELs, using an approach that allows for extending to more VCSELs. Our experiments are a first step towards implementing RC with diffractively coupled VCSELs. There are various possibilities to modify and to adapt the experimental scheme. The main challenge remaining is the low SNR of the VCSELs' responses to modulated injection.

Acronyms and other abbreviations

ADOPD	**Ad**aptive **Op**tical **D**endrites
amp	**amp**lifier
att	**att**enuator
AWG	**A**rbitrary **W**aveform **G**enerator
BEC	**B**locked **E**xternal **C**avity
BS	**B**eam **S**plitter
CCD	**C**harge-**C**oupled **D**evice
CD	**C**ompact **D**isc
CMOS	**C**omplementary **M**etal-**O**xide-**S**emiconductor
CQFP	**C**eramic **Q**uad **F**lat **P**ackage
CSIC	**C**onsejo **S**uperior de **I**nvestigaciones **C**ientíficas
cw	**c**onstant **w**ave
DAC	**D**igital-to-**A**nalog **C**onversion
DBR	**D**istributed **B**ragg **R**eflector
DC	**D**irect **C**urrent
DOE	**D**iffractive **O**ptical **E**lement
DVD	**D**igital **V**ideo/**V**ersatile **D**isc
ER	**E**rror **R**ate
ES	**E**lectrical **S**ourcemeter
ESA	**E**lectrical **S**pectrum **A**nalyzer
ESN	**E**cho **S**tate **N**etwork
FESC	**F**ísica **E**xperimental de **S**istemas **C**omplejos
FB	**F**eed**b**ack
FWHM	**F**ull **W**idth at **H**alf **M**aximum
HR	**H**eader **R**ecognition
IFISC	**I**nstitut de **F**ísica **I**nterdisciplinària i **S**istemes **C**omplexos
inj	**inj**ection laser
L	**L**ens
laser	**l**ight **a**mplification by **s**timulated **e**mission of **r**adiation
LP modes	**L**inearly **P**olarized modes
LSM	**L**iquid **S**tate **M**achine
MC	**M**emory **C**apacity
MM	**M**ulti-**M**ode
MO	**M**icroscope **O**bjective
MSB	**M**ost **S**ignificant **B**it
MZM	**M**ach-**Z**ehnder **M**odulator
NA	**N**umerical **A**perture
NDF	**N**eutral **D**ensity **F**ilter
NRMSE	**N**ormalized **R**oot **M**ean **S**quare **E**rror
OSA	**O**ptical **S**pectrum **A**nalyzer
Osci	**Osci**lloscope
PBS	**P**olarizing **B**eam **S**plitter
PC	**P**ersonal **C**omputer
PCB	**P**rinted **C**ircuit **B**oard
PD	**P**hoto**d**etector
PM	**P**olarization **M**aintaining
PowM	**Pow**er**m**eter

PSD	**P**ower **S**pectral **D**ensity
RC	**R**eservoir **C**omputing
RF	**R**adio **F**requency
RMS	**R**oot **M**ean **S**quare
RO	**R**elaxation **O**scillation
S (only in MS or GS)	**S**amples (Megasamples or Gigasamples)
SAA	**S**mall-**A**ngle **A**pproximation
SC	**S**hort **C**ircuit
SFM	**S**pin-**F**lip **M**odel
SL	**S**emiconductor **L**aser
SLM	**S**patial **L**ight **M**odulator
SM	**S**ingle **M**ode
SNR	**S**ignal-to-**N**oise **R**atio
UIB	**U**niversitat de les **I**lles **B**alears
VCSEL	**V**ertical-**C**avity **S**urface-**E**mitting **L**aser
XOR	E**x**clusive **Or**

Symbols

Symbol	*Name & Description*	*Basic unit (without prefix)*
a	DOE parameter	m
a_n	n^{th} point of reservoir output	1
(c,r)	VCSEL in column c and row r	-
C_{DOE}	multiplexing matrix coefficient of the DOE	1
E	electric field	Vm^{-1}
f_{ext}	external cavity frequency	Hz
f_{RO}	relaxation oscillation frequency	Hz
g	gain per unit length	m^{-1}
$g_{1/5}$	1st / 5th order polynomial fits	-
I	light intensity (Chap. 1) current	Wm^{-2} A
$I(c,r)$	pump current of VCSEL (c,r)	A
I_{th}	threshold current	A
J	spin quantum number (Chap. 1) number of nodes used for RC	1
k	time steps back (MC task) number of bits (HR, DAC, and XOR tasks)	1
$k_{1/2}$	distance of VCSEL from array center	p
k_c	coupling coefficient	s^{-1}
l_n	distance of n^{th} VCSEL to optical axis	m
m	carrier number difference of magnetic sublevels	1
M_k	memory correlation for k time steps back	1
n	carrier density in active region (Chap. 1) index for RC input / target / output series (Chap. 5)	1
N	difference between actual carriers and carriers at transparency (Chap. 1) length of injected sequence (Chap. 5)	1
p	pitch, distance between not diagonally neighbouring VCSEL value of D'Agostino omnibus test	m 1
P	optical power	W
$P(c,r)$	optical power emitted by VCSEL (c,r)	W
P_{ref}	optical power in reference fiber	W
P_{inj}	optical power of the injection laser (after isolator or MZM, depending on setup)	W
$P\|_{\text{tf},(c,r)}$	optical power at the top facet of VCSEL (c,r)	W
q_n	averaged response of a VCSEL to the injection of r_n	V
r_n	n^{th} random number of the used series	1
R_{OFC}	reflection coefficient of optical free-space component OFC	1
s	pixel size	m / pixel
S	photon number (Chap. 1) indices $n \in \mathbb{N}$ for which r_n in the training set (Chap. 5)	1
T_{inj}	injection laser temperature	°C
T_{OFC}	transmission coefficient of optical free-space component OFC	1
U	voltage	V
w_j	output weight for j^{th} reservoir node	V^{-1}
$w_{x/y}$	beam width in x/y-direction	m
x	direction orthogonal to beam path and optical table	m
y	direction orthogonal to beam path and parallel to optical table	m
y_n	n^{th} value of RC target output series	1
y_{NL}	measure for nonlinearity of VCSEL response	1
z	direction of propagation of the light / beam path	m
Z	reservoir performance ER, NRMSE, or MC	1
α	linewidth enhancement factor parameter for ridge regression (Chap. 5)	1

β	ratio of beam diameter in x- and y-direction	1
γ	lifetime or decay/relaxation rate	s
ϵ	injection laser attenuation	dB
ζ	change of η with feedback	%
η	refractive index (Chap. 1) slope efficiency	1 WA^{-1}
ϑ	angle of 1st DOE diffraction order for orthogonal incoming beam	$^\circ$
$\theta_n^{\pm}$	angles between 1st DOE diffraction order and optical axis	$^\circ$
κ	feedback strength	s^{-1}
λ	wavelength	m
$\lambda(c,r)$	peak emission wavelength of VCSEL (c,r)	m
λ_{pair}	peak wavelength of spectra for pairwise coupling	m
λ_{match}	wavelength usually used for spectrally aligning the VCSELs	m
ν	DOE angle perpendicular to optical axis	$^\circ$
ξ	feedback attenuation	dB
ρ	Pearson correlation	1
σ_X	standard deviation of quantity X	1
τ_c	cavity photon lifetime	s
τ_{ext}	external cavity round-trip	s
ϕ	phase of the optical field (Chap. 1) angle of linear polarizer (Chap. 3)	rad $^\circ$
φ_n	angle between VCSEL beam and optical axis	$^\circ$
χ	electric susceptibility	1
Ψ	change of I_{th} with feedback	%
ω	angular frequency of light	Hz
$\forall$	for all	-
$\overline{*}$	arithmetic mean of quantity $*$	-

Used instruments and components

Instrument or component	*Provider and model number*	*Abbreviation*	*Properties / technical details*
Achromatic lens	Thorlabs AC254-080-B	L1	$f = 80\,\mathrm{mm}$
Arbitrary Waveform Generator	Tektronix AWG7122B	AWG	Sampling rate: 12 GS/s
Aspheric lens	Thorlabs AL1225-B	L2	$f = 25.0\,\mathrm{mm}$, NA = 0.23
Aspheric lens	Thorlabs AL2018	L3	$f = 18.0\,\mathrm{mm}$, NA = 0.49
Beamsplitter cube	Thorlabs BS014	50/50 BS or BS1	at 975 nm, p-polarized: 47.3 % transmission (T), 45.7 % reflection (R) s-polarized: 49.1 % T, 42.6 % R
Beamsplitter cube	Thorlabs BS023	30/70 BS or BS2	at 975 nm, p-pol.: 25.5 % T, 66.4 % R s-pol.: 28.7 % T, 61.0 % R
Broadband electrical amplifier	SHF 826H	amp	70 kHz to 25 GHz
Calcite beam displacer	Thorlabs BD40	-	350 nm to 2.3 µm; 4 mm beam separation
CCD camera	PCO Sensicam QE	-	see manual
Ceramic quad flat package	Kyocera PB23866	CQFP	-
CMOS camera	Thorlabs DCC1545M	-	see manual
Dielectric mirror	Thorlabs BB1-E03	mirror	750 nm to 1100 nm
Diffractive optical element	Holoor MS-261-970-Y-X	DOE	3×3 pattern separation angle $\vartheta = 0.52°$ at 975 nm
Electric sourcemeter	Keithley 2611B	ES	Measurement resolution: 100 fA / 100 nV
Electrical spectrum analyzer	Anritsu MS2667C	ESA	9 kHz to 30 GHz
External DBR injection laser	Thorlabs DBR976PN	inj	$\lambda = 976.4\,\mathrm{nm}$ at 25 °C linewidth $\Delta f \approx 5\,\mathrm{MHz}$
In-fiber optical isolator	unknown	-	isolation at 976 nm: 26 dB insertion loss at 976 nm: 2 dB
Linear polarizer	Thorlabs LPNIR050-MP	-	100000:1 extinction ratio from 850 nm to 1600 nm
Mach-Zehnder modulator	Eospace AZ-0K5-10-PFA-PFA-970	MZM	extinction ratio: 25 dB
Microscope objective	Olympus LCPLN20XIR	MO	$f_{\mathrm{MO}} = 9\,\mathrm{mm}$, NA = 0.45
Absorptive neutral density filters	Thorlabs NExxA	NDFs	transmission at 976 nm between 0.117 % and 53.9 %
Optical spectrum analyzer	Anritsu MS9710C	OSA	FWHM resolution: 50 pm, read resolution: 5 pm
Oscilloscope	Lecroy Wavemaster 816Zi	Osci	16 GHz bandwidth, 40 GS/s
Photodiode	New Focus 1554-A-50	PD	3-dB-bandwidth 10 kHz to 12 GHz
Plano-convex lens	Thorlabs LA1027-B	L4	$f = 34.9\,\mathrm{mm}$
Polarizing beamsplitter cube	Thorlabs CM1PBS253	PBS	900 nm - 1300 nm
Ruled reflective diffraction grating	Thorlabs GR13-1210	DG	1200 grooves/mm
Tunable electrical attenuator	Narda 4745-69	att	DC to 18 GHz
$\lambda/2$ waveplate	Thorlabs WPH10M-980	$\lambda/2$	-

Bibliography

1. Hecht, J. Short history of laser development. *Optical Engineering* **49,** 1 –23. https://doi.org/10.1117/1.3483597 (2010).
2. Wills, S. The Laser at 60. *Opt. Photon. News* **31,** 30–39. https://www.optica-opn.org/home/articles/volume_31/may_2020/features/the_laser_at_60/ (2020).
3. *Handbook of Lasers and Optics* 2nd ed. (ed Träger, F.) ISBN: 978-3-642-19408-5 (Springer, 2012).
4. Soriano, M. C., García-Ojalvo, J., Mirasso, C. R. & Fischer, I. Complex photonics: Dynamics and applications of delay-coupled semiconductors lasers. *Reviews of Modern Physics* **85,** 421–470. ISSN: 0034-6861, 1539-0756. http://link.aps.org/doi/10.1103/RevModPhys.85.421 (2013).
5. Iga, K. Surface-emitting laser-its birth and generation of new optoelectronics field. *IEEE Journal of Selected Topics in Quantum Electronics* **6,** 1201–1215 (2000).
6. Soda, H., Iga, K.-I., Kitahara, C. & Suematsu, Y. GaInAsP/InP Surface Emitting Injection Lasers. *Japanese Journal of Applied Physics* **18,** 2329–2330. https://doi.org/10.1143/jjap.18.2329 (1979).
7. Iga, K., Koyama, F. & Kinoshita, S. Surface emitting semiconductor lasers. *IEEE Journal of Quantum Electronics* **24,** 1845–1855 (1988).
8. Yu, S. F. *Analysis and Design of Vertical Cavity Surface Emitting Lasers* ISBN: 978-0-471-39124-1 (Wiley, 2003).
9. Heuser, T. *et al.* Developing a photonic hardware platform for brain-inspired computing based on 5 x 5 VCSEL arrays. *J. Phys. Photonics* **2,** 044002. ISSN: 2515-7647 (2020).
10. San Miguel, M., Feng, Q. & Moloney, J. Dynamics in Surface-Emitting Semiconductor Lasers. *Physical Review A* **52,** 1728–1739 (1995).
11. Mulet, J. & Balle, S. Spatio-temporal modeling of the optical properties of VCSELs in the presence of polarization effects. *IEEE Journal of Quantum Electronics* **38,** 291–305 (2002).
12. Henry, C. H. Theory of the Linewidth of Semiconductor Lasers. *IEEE Journal of Quantum Electronics* **18,** 259–264. ISSN: 15581713 (1982).
13. Osinski, M. & Buus, J. Linewidth Broadening Factor in Semiconductor Lasers–An Overview. *IEEE Journal of Quantum Electronics* **23,** 9–29. ISSN: 15581713 (1987).
14. Fordell, T. & Lindberg, Å. M. Experiments on the linewidth-enhancement factor of a vertical-cavity surface-emitting laser. *IEEE Journal of Quantum Electronics* **43,** 6–15. ISSN: 00189197 (2007).
15. Hohl, A., Gavrielides, A. & Erneux, T. Localized Synchronization in Two Coupled Nonidentical Semiconductor Lasers. *Physical Review Letters* **78,** 4745–4748. ISSN: 10797114 (1997).
16. Mulet, J., Mirasso, C., Heil, T. & Fischer, I. Synchronization scenario of two distant mutually coupled semiconductor lasers. *Journal of Optics B: Quantum and Semiclassical Optics* **6,** 97–105. ISSN: 14644266 (2004).

17. Heil, T., Fischer, I., Elsässer, W., Mulet, J. & Mirasso, C. R. Chaos Synchronization and Spontaneous Symmetry-Breaking in Symmetrically Delay-Coupled Semiconductor Lasers. *Phys. Rev. Lett.* **86,** 795–798. https://link.aps.org/doi/10.1103/PhysRevLett.86.795 (2001).
18. Ozaki, M. *et al.* Leader-laggard relationship of chaos synchronization in mutually coupled vertical-cavity surface-emitting lasers with time delay. *Phys. Rev. E* **79,** 026210. https://link.aps.org/doi/10.1103/PhysRevE.79.026210 (2009).
19. Yang, W. *et al.* Experimental investigation on the nonlinear dynamics of two mutually coupled 1550 nm multi-transverse-mode vertical-cavity surface-emitting lasers. *Applied Optics* **58,** 1271–1275. ISSN: 1559-128X (2019).
20. Wieczorek, S., Krauskopf, B., Simpson, T. B. & Lenstra, D. The dynamical complexity of optically injected semiconductor lasers. *Physics Reports* **416,** 1–128. ISSN: 03701573 (2005).
21. Henry, C. H., Olsson, N. A. & Dutta, N. K. Locking Range and Stability of Injection Locked 1.54 µm InGaAsP Semiconductor Lasers. *IEEE Journal of Quantum Electronics* **21,** 1152–1156. ISSN: 15581713 (1985).
22. Chang, C.-H., Chrostowski, L. & Chang-Hasnain, C. Injection locking of VCSELs. *IEEE Journal of Selected Topics in Quantum Electronics* **9,** 1386–1393 (2003).
23. Ohtsubo, J. *Semiconductor Lasers: Stability, Instability and Chaos* 3rd ed. ISBN: 978-3-642-30146-9 (Springer, 2013).
24. Lang, R. & Kobayashi, K. External Optical Feedback Effects on Semiconductor Injection Laser Properties. *IEEE Journal of Quantum Electronics* **16,** 347–355. ISSN: 15581713 (1980).
25. Panajotov, K., Sciamanna, M., Arteaga, M. A. & Thienpont, H. Optical feedback in vertical-cavity surface-emitting lasers. *IEEE Journal on Selected Topics in Quantum Electronics* **19,** 1700312. ISSN: 1077260X (2013).
26. Tkach, R. & Chraplyvy, A. Regimes of feedback effects in 1.5-µm distributed feedback lasers. *Journal of Lightwave Technology* **4,** 1655–1661 (1986).
27. Olsson, A & Tang, C. Coherent Optical Interference Effects in External-Cavity Semiconductor Lasers. *IEEE Journal of Quantum Electronics* **17,** 1320–1323 (1981).
28. Jiang, S., Pan, Z., Dagenais, M., Morgan, R. A. & Kojima, K. Influence of External Optical Feedback on Threshold and Spectral Characteristics of Vertical-Cavity Surface-Emitting Lasers. *IEEE Photonics Technology Letters* **6,** 34–36. ISSN: 19410174 (1994).
29. Jiang, S., Dagenais, M. & Morgan, R. A. Spectral Characteristics of Vertical-Cavity Surface-Emitting Lasers with Strong External Optical Feedback. *IEEE Photonics Technology Letters* **7,** 739–744. ISSN: 19410174 (1995).
30. Argyris, A., Bourmpos, M. & Syvridis, D. Experimental synchrony of semiconductor lasers in coupled networks. *Optics Express* **24,** 5600–5614. ISSN: 1094-4087. https://www.osapublishing.org/abstract.cfm?URI=oe-24-5-5600 (2016).
31. Hill, M., Frietman, E., de Waardt, H., Khoe, G.-D. & Dorren, H. All fiber-optic neural network using coupled SOA based ring lasers. *IEEE Transactions on Neural Networks* **13,** 1504–1513 (2002).
32. Kanno, K., Hida, T., Uchida, A. & Bunsen, M. Spontaneous exchange of leader-laggard relationship in mutually coupled synchronized semiconductor lasers. *Physical Review E* **95,** 052212. ISSN: 2470-0045. http://link.aps.org/doi/10.1103/PhysRevE.95.052212 (2017).

33. Lehman, A. C. & Choquette, K. D. One- and Two-Dimensional Coherently Coupled Implant-Defined Vertical-Cavity Laser Arrays. *IEEE Photonics Technology Letters* **19,** 1421–1423 (2007).
34. Gao, Z. *et al.* Bottom-Emitting Coherently Coupled Vertical Cavity Laser Arrays. *IEEE Photonics Technology Letters* **28,** 513–515. ISSN: 10411135 (2016).
35. Bao, L. *et al.* Near-diffraction-limited coherent emission from large aperture antiguided vertical-cavity surface-emitting laser arrays. *Applied Physics Letters* **84,** 320–322. https://doi.org/10.1063/1.1640799 (2004).
36. Bao, L. *et al.* Modeling, fabrication, and characterization of large aperture two-dimensional antiguided vertical-cavity surface-emitting laser arrays. *IEEE Journal of Selected Topics in Quantum Electronics* **11,** 968–981 (2005).
37. Kao, T. Y., Reno, J. L. & Hu, Q. Phase-locked laser arrays through global antenna mutual coupling. *Nature Photonics* **10,** 541–546. ISSN: 17494893. http://dx.doi.org/10.1038/nphoton.2016.104 (2016).
38. Lyakh, A., Maulini, R., Tsekoun, A., Go, R. & Patel, C. K. N. Continuous wave operation of buried heterostructure 46µm quantum cascade laser Y-junctions and tree arrays. *Optics Express* **22,** 1203–1208. ISSN: 1094-4087. https://www.osapublishing.org/oe/abstract.cfm?uri=oe-22-1-1203 (2014).
39. Katz, J., Margalit, S. & Yariv, A. Diffraction coupled phase-locked semiconductor laser array. *Applied Physics Letters* **42,** 554–556. https://doi.org/10.1063/1.94025 (1983).
40. Jia, Z. *et al.* Phase-locked array of quantum cascade lasers with an intracavity spatial filter. *Applied Physics Letters* **111,** 061108. ISSN: 00036951 (2017).
41. Ma, Y. *et al.* Phase-locking dynamics of a 2D VCSEL hexagonal array with an integrated Talbot cavity. *Opt. Express* **30,** 9892–9903. http://opg.optica.org/oe/abstract.cfm?URI=oe-30-6-9892 (2022).
42. Fischer, I. *et al.* Zero-Lag Long-Range Synchronization via Dynamical Relaying. *Phys. Rev. Lett.* **97,** 123902. https://link.aps.org/doi/10.1103/PhysRevLett.97.123902 (12 2006).
43. Nixon, M. *et al.* Controlling synchronization in large laser networks. *Physical Review Letters* **108,** 214101. ISSN: 00319007 (2012).
44. Antyukhov, V. *et al.* Effective phase locking of an array of lasers. *Pis'ma Zh. Eksp. Teor. Fiz.* **44,** 63–65 (1986).
45. Liu, B, Liu, Y & Braiman, Y. Coherent beam combining of high power broad- area laser diode array with a closed-V-shape external Talbot cavity. *Optics Express* **18,** 7361–7368 (2010).
46. Brunner, D. & Fischer, I. Reconfigurable semiconductor laser networks based on diffractive coupling. *Optics Letters* **40,** 3854–3857. ISSN: 0146-9592, 1539-4794. https://www.osapublishing.org/abstract.cfm?URI=ol-40-16-3854 (2015).
47. Maktoobi, S. *et al.* Diffractive Coupling For Photonic Networks: How Big Can We Go? *IEEE Journal of Selected Topics in Quantum Electronics* **26,** 7600108. ISSN: 1077-260X. arXiv: 1907.05661 (2019).
48. Bueno, J. *et al.* Reinforcement Learning in a large scale photonic Recurrent Neural Network. *Optica* **5,** 756–760. ISSN: 2334-2536 (2018).
49. Agrawal, G. P. Line Narrowing in a Single-Mode Injection Laser Due to External Optical Feedback. *IEEE Journal of Quantum Electronics* **20,** 468–471. ISSN: 15581713 (1984).

50. Brunner, D., Luna, R., Delhom i Latorre, A., Porte, X. & Fischer, I. Semiconductor laser linewidth reduction by six orders of magnitude via delayed optical feedback. *Optics Letters* **42,** 163. ISSN: 0146-9592. https://www.osapublishing.org/abstract.cfm?URI=ol-42-1-163 (2017).

51. Peil, M. *et al.* Rainbow refractometry with a tailored incoherent semiconductor laser source. *Applied Physics Letters* **89,** 091106 (2006).

52. Uchida, A. *et al.* Fast physical random bit generation with chaotic semiconductor lasers. *Nature Photonics* **2,** 728–732. ISSN: 17494885 (2008).

53. Oliver, N., Soriano, M. C., Sukow, D. W. & Fischer, I. Fast random bit generation using a chaotic laser: Approaching the information theoretic limit. *IEEE Journal of Quantum Electronics* **49,** 910–918. ISSN: 00189197 (2013).

54. Sakuraba, R., Iwakawa, K., Kanno, K. & Uchida, A. Tb/s physical random bit generation with bandwidth-enhanced chaos in three-cascaded semiconductor lasers. *Opt. Express* **23,** 1470–1490. http://opg.optica.org/oe/abstract.cfm?URI=oe-23-2-1470 (2015).

55. Guo, Y. *et al.* Ultrafast and real-time physical random bit extraction with all-optical quantization. *Advanced Photonics* **4,** 1 –8. https://doi.org/10.1117/1.AP.4.3.035001 (2022).

56. Porte, X., Soriano, M. C., Brunner, D. & Fischer, I. Bidirectional private key exchange using delay-coupled semiconductor lasers. *Optics Letters* **41,** 2871–2874. ISSN: 0146-9592. https://www.osapublishing.org/abstract.cfm?URI=ol-41-12-2871 (2016).

57. Dudley, J. M., Genty, G., Mussot, A., Chabchoub, A. & Dias, F. Rogue waves and analogies in optics and oceanography. *Nature Reviews Physics* **1,** 675–689. ISSN: 25225820 (2019).

58. Roelfsema, P. R., Engel, A. K., König, P. & Singer, W. Visuomotor integration is associated with zero time-lag synchronization among cortical areas. *Nature* **385,** 157–161. https://doi.org/10.1038/385157a0 (1997).

59. Vicente, R., Gollo, L. L., Mirasso, C. R., Fischer, I. & Pipa, G. Dynamical relaying can yield zero time lag neuronal synchrony despite long conduction delays. *Proceedings of the National Academy of Sciences* **105,** 17157–17162. https://www.pnas.org/doi/abs/10.1073/pnas.0809353105 (2008).

60. Gollo, L. L., Mirasso, C. & Villa, A. E. Dynamic control for synchronization of separated cortical areas through thalamic relay. *NeuroImage* **52,** 947–955. ISSN: 10538119. http://dx.doi.org/10.1016/j.neuroimage.2009.11.058 (2010).

61. Vardi, R. *et al.* Synthetic reverberating activity patterns embedded in networks of cortical neurons. *Europhysics Letters* **97.** ISSN: 02955075. arXiv: 1201.0339 (2012).

62. Brunner, D., Soriano, M. C., Mirasso, C. R. & Fischer, I. Parallel photonic information processing at gigabyte per second data rates using transient states. *Nature Communications* **4,** 1364. ISSN: 2041-1723. http://www.nature.com/doifinder/10.1038/ncomms2368 (2013).

63. Skalli, A. *et al.* Photonic neuromorphic computing using vertical cavity semiconductor lasers. *Opt. Mater. Express* **12,** 2395–2414. http://opg.optica.org/ome/abstract.cfm?URI=ome-12-6-2395 (2022).

64. Hejda, M., Robertson, J., Bueno, J., Alanis, J. A. & Hurtado, A. Neuromorphic encoding of image pixel data into rate-coded optical spike trains with a photonic VCSEL-neuron. *APL Photonics* **6,** 060802. ISSN: 23780967. https://doi.org/10.1063/5.0048674 (2021).

65. Robertson, J., Hejda, M., Bueno, J. & Hurtado, A. Ultrafast optical integration and pattern classification for neuromorphic photonics based on spiking VCSEL neurons. *Scientific Reports* **10,** 6098. ISSN: 20452322 (2020).

66. Vatin, J., Rontani, D. & Sciamanna, M. Experimental reservoir computing using VCSEL polarization dynamics. *Optics Express* **27,** 18579–18584 (2019).

67. Porte, X. *et al.* A complete, parallel and autonomous photonic neural network in a semiconductor multimode laser. *J. Phys. Photonics* **3,** 024017. ISSN: 25157647. arXiv: 2012.11153 (2021).

68. Verstraeten, D., Schrauwen, B., D'Haene, M. & Stroobandt, D. An experimental unification of reservoir computing methods. *Neural Networks* **20,** 391–403. ISSN: 0893-6080. https://www.sciencedirect.com/science/article/pii/S089360800700038X (2007).

69. Jaeger, H. The "echo state" approach to analysing and training recurrent neural networks. *GMD Report* **148.** http://publica.fraunhofer.de/documents/B-73131.html (2001).

70. Jaeger, H. & Haas, H. Harnessing Nonlinearity: Predicting Chaotic Systems and Saving Energy in Wireless Communication. *Science* **304,** 78–80. ISSN: 0036-8075, 1095-9203. http://science.sciencemag.org/content/304/5667/78 (2004).

71. Maass, W., Natschläger, T. & Markram, H. Real-Time Computing Without Stable States: A New Framework for Neural Computation Based on Perturbations. *Neural Computation* **14,** 2531–2560. ISSN: 0899-7667. https://doi.org/10.1162/089976602760407955 (Nov. 2002).

72. Appeltant, L. *et al.* Information processing using a single dynamical node as complex system. *Nature Communications* **2,** 468. ISSN: 20411723. arXiv: 1111.7219. http://dx.doi.org/10.1038/ncomms1476 (2011).

73. Torrejon, J. *et al.* Neuromorphic computing with nanoscale spintronic oscillators. *Nature* **547,** 428–431. ISSN: 14764687. arXiv: 1701.07715. http://dx.doi.org/10.1038/nature23011 (2017).

74. Aaser, P. *et al. Towards making a cyborg: A closed-loop reservoir-neuro system* in *Proc. of ECAL 2017, the Fourteenth European Conference on Artificial Life* (2017), 430–437. https://direct.mit.edu/isal/proceedings/ecal2017/430/99563.

75. Bueno, J., Brunner, D., Soriano, M. C. & Fischer, I. Conditions for reservoir computing performance using semiconductor lasers with delayed optical feedback. *Optics Express* **25,** 2401–2412. ISSN: 1094-4087. https://www.osapublishing.org/abstract.cfm?uri=oe-25-3-2401 (2017).

76. Dong, J., Rafayelyan, M., Krzakala, F. & Gigan, S. Optical Reservoir Computing Using Multiple Light Scattering for Chaotic Systems Prediction. *IEEE Journal of Selected Topics in Quantum Electronics* **26,** 1–12 (2020).

77. Argyris, A., Bueno, J. & Fischer, I. Photonic machine learning implementation for signal recovery in optical communications. *Scientific Reports* **8,** 8487. ISSN: 20452322. arXiv: 1710.01107 (2018).

78. Antonik, P., Marsal, N., Brunner, D. & Rontani, D. *Classification of Human Actions in Videos with a Large-Scale Photonic Reservoir Computer* in *Artificial Neural Networks and Machine Learning – ICANN 2019: Workshop and Special Sessions* (eds Tetko, I. V., Kůrková, V., Karpov, P. & Theis, F.) (Springer International Publishing, Cham, 2019), 156–160. ISBN: 978-3-030-30493-5.

79. Vatin, J., Rontani, D. & Sciamanna, M. Enhanced performance of a reservoir computer using polarization dynamics in VCSELs. *Optics Letters* **43,** 4497–4500. ISSN: 0146-9592 (2018).

80. Rafayelyan, M., Dong, J., Tan, Y., Krzakala, F. & Gigan, S. Large-Scale Optical Reservoir Computing for Spatiotemporal Chaotic Systems Prediction. *Phys. Rev. X* **10,** 041037. https://link.aps.org/doi/10.1103/PhysRevX.10.041037 (2020).

81. Dietrich, C. *Design and Realization of a Dynamic Semiconductor Laser Network* MA thesis (Westfälische Wilhelms-Universität Münster, 2015).

82. Chen, Z. *et al. Deep Learning with Coherent VCSEL Neural Networks* 2022. https://arxiv.org/abs/2207.05329.

83. Bava, G. P., Debernardi, P. & Fratta, L. Three-dimensional model for vectorial fields in vertical-cavity surface-emitting lasers. *Phys. Rev. A* **63,** 023816. https://link.aps.org/doi/10.1103/PhysRevA.63.023816 (2 2001).

84. Choquette, K. D. *et al.* Selective oxidation of buried AlGaAs versus AlAs layers. *Applied Physics Letters* **69,** 1385. https://doi.org/10.1063/1.117589 (1996).

85. Debernardi, P., Bava, G., Degen, C., Fischer, I. & Elsasser, W. Influence of anisotropies on transverse modes in oxide-confined VCSELs. *IEEE Journal of Quantum Electronics* **38,** 73–84 (2002).

86. Porte, X., Soriano, M. C. & Fischer, I. Similarity properties in the dynamics of delayed-feedback semiconductor lasers. *Physical Review A* **89,** 023822 (2014).

87. Pflüger, M. *et al.* Injection locking and coupling the emitters of large VCSEL arrays via diffraction in an external cavity. *Opt. Express* **31,** 8704–8713. https://opg.optica.org/oe/abstract.cfm?URI=oe-31-5-8704 (2023).

88. Hurtado, A., Labukhin, D., Henning, I. D. & Adams, M. J. Injection Locking Bandwidth in 1550-nm VCSELs Subject to Parallel and Orthogonal Optical Injection. *IEEE Journal of Selected Topics in Quantum Electronics* **15,** 585–593 (2009).

89. Blokhin, S. A. *et al.* Emission-Line Width and α-Factor of 850-nm Single-Mode Vertical-Cavity Surface-Emitting Lasers Based on InGaAs/AlGaAs Quantum Wells. *Semiconductors* **52,** 93–99. ISSN: 10637826 (2018).

90. Summers, H. D., Dowd, P., White, I. H. & Tan, M. R. Calculation of Differential Gain and Linewidth Enhancement Factor in 980-nm InGaAs Vertical Cavity Surface-Emitting Lasers. *IEEE Photonics Technology Letters* **7,** 736–738. ISSN: 19410174 (1995).

91. Gerhardt, N. C. & Hofmann, M. R. Experimental analysis of the optical gain and linewidth enhancement factor of GaInNAs/GaAs lasers. *Journal of Physics Condensed Matter* **16,** S3095 –S3106. ISSN: 09538984 (2004).

92. Hsu, A., Seurin, J. F., Chuang, S. L. & Choquette, K. D. Optical feedback in vertical-cavity surface-emitting lasers. *IEEE Journal of Quantum Electronics* **37,** 1643–1649. ISSN: 00189197 (2001).

93. D'Agostino, R. B., Belanger, A. & D'Agostino, R. B. J. A Suggestion for Using Powerful and Informative Tests of Normality. *The american statistician* **44,** 316–321 (1990).

94. Hassan, U. & Anwar, M. S. Reducing noise by repetition: Introduction to signal averaging. *European Journal of Physics* **31,** 453–465. ISSN: 01430807 (2010).

95. Semenova, N. & Brunner, D. Noise-mitigation strategies in physical feedforward neural networks. *Chaos* **32,** 061106. https://doi.org/10.1063/5.0096637 (2022).

96. Vandoorne, K. *et al.* Experimental demonstration of reservoir computing on a silicon photonics chip. *Nature Communications* **5,** 1–6. ISSN: 20411723 (2014).

97. Jaeger, H. Short Term Memory in Echo State Networks. *GMD Report* **152,** 12–13. http://publica.fraunhofer.de/documents/B-73131.html (2001).

98. Bueno, J. *Photonic Information Processing* PhD thesis (Universitat de les Illes Balears, 2018).

99. Ortín, S. *et al.* A Unified Framework for Reservoir Computing and Extreme Learning Machines based on a Single Time-delayed Neuron. *Scientific Reports* **5,** 14945. ISSN: 20452322. http://dx.doi.org/10.1038/srep14945 (2015).

100. Andreoli, L. *et al.* Optical pumping of quantum dot micropillar lasers. *Optics Express* **29,** 9084–9097. ISSN: 1094-4087 (2021).